

8.03

Fundamentals of Interface Mechanics

T. C. WANG

*Institute of Mechanics of the Chinese Academy of Sciences, Beijing,
People's Republic of China*

8.03.1	ELASTIC INTERFACE MECHANICS	90
8.03.1.1	<i>Stress Jump across Interface</i>	90
8.03.1.2	<i>Complex Potential</i>	91
8.03.2	ELASTIC FRACTURE MECHANICS FOR AN INTERFACE CRACK	91
8.03.2.1	<i>Crack Tip Fields</i>	91
8.03.2.2	<i>Interface Toughness with $\beta = 0$</i>	92
8.03.2.3	<i>Interface Toughness with $\beta \neq 0$</i>	93
8.03.2.4	<i>Kinking Out of an Interface</i>	94
8.03.2.5	<i>Mechanics Models of an Interface Crack</i>	94
8.03.3	TYPICAL INTERFACE FRACTURE PROBLEMS	96
8.03.3.1	<i>Film Decohesion</i>	96
8.03.3.1.1	<i>Film decohesion from edges or channels</i>	97
8.03.3.1.2	<i>Decohesion from a hole</i>	97
8.03.3.1.3	<i>Effects of plasticity and segregation</i>	97
8.03.3.2	<i>Cracking in Films</i>	101
8.03.3.2.1	<i>Crack patterns in the film</i>	101
8.03.3.2.2	<i>Surface crack</i>	102
8.03.3.2.3	<i>Crack channeling</i>	104
8.03.3.2.4	<i>Substrate cracking</i>	105
8.03.3.3	<i>Debonding and Sliding in Brittle Matrix Composites</i>	105
8.03.3.4	<i>Cracks in Multilayers</i>	108
8.03.3.4.1	<i>A straight crack within the layer</i>	108
8.03.3.4.2	<i>Crack along the interface</i>	109
8.03.3.4.3	<i>Alternating cracking</i>	110
8.03.3.4.4	<i>Tunneling cracks</i>	110
8.03.3.5	<i>Crack Perpendicular to a Bimaterial Interface</i>	111
8.03.3.5.1	<i>Crack perpendicular to a bimaterial interface</i>	111
8.03.3.5.2	<i>Crack perpendicular to and terminating at a bimaterial interface</i>	114
8.03.4	INTERFACE FRACTURE TEST	115
8.03.4.1	<i>Delamination Specimens and R-curves</i>	116
8.03.4.2	<i>Interface Fracture Specimens</i>	117
8.03.4.3	<i>Brazil-nut Specimen</i>	117
8.03.4.4	<i>Fracture Energy Data</i>	118
8.03.5	INTERFACE CRACKS IN DISSIMILAR ANISOTROPIC MEDIA	119
8.03.5.1	<i>Basic Formulas</i>	120
8.03.5.2	<i>Interface Crack in Anisotropic Bimaterials: Nonoscillatory Fields</i>	120
8.03.5.3	<i>Interface Crack in Anisotropic Bimaterials: Oscillatory Fields</i>	121
8.03.5.4	<i>Crack Kinking out of an Interface</i>	121
8.03.6	ELASTIC-PLASTIC FRACTURE MECHANICS FOR AN INTERFACE CRACK	122
8.03.6.1	<i>Elastic-Plastic Analyses of Interface Crack</i>	122
8.03.6.2	<i>Crack Tip Fields for a Bimaterial Interface</i>	124
8.03.6.3	<i>Elastic-Plastic Solutions with a Contact Zone</i>	124
8.03.6.4	<i>High-order Solutions</i>	129
8.03.6.4.1	<i>High-order solutions with traction free crack surfaces</i>	130

8.03.1 ELASTIC INTERFACE MECHANICS

Advanced materials, such as fiber or particle reinforced composites, structure ceramics, laminated materials, polycrystalline intermetallic alloys, adhesive joints, etc., have many important applications in the combustion engine components, aerospace bearings, cutting tools, hip joints, advanced energy generation systems, components for printing industry, transmission elements, etc. Their fracture, fatigue, corrosion, or wear behavior can be significantly improved by surface coating. Thin films of metals, ceramics, and polymers deposited on tools, machinery, or electronic devices can endow the structures with new thermal, mechanical, chemical, and tribological properties.

Interfaces are intrinsic to these materials. The overall mechanical behavior of such materials and material systems strongly depends on the interfacial features such as discontinuities in elastic and thermal properties, residual stresses around the interfaces, and the cohesive stresses along the interfaces. Interface failures are a common feature in advanced materials and thin films. The design process of these components requires a better understanding of their failure mechanisms. An important task is devoted to detailed investigations of the fracture characteristics of flaws along or perpendicular to the interface.

8.03.1.1 Stress Jump across Interface

Consider two semi-infinite elastic solids joined along the x -axis as shown in Figure 1. A Cartesian coordinate system oxy is attached to the interface. The x -axis is along the interface and the y -axis is normal to the interface. Both materials are isotropic and homogeneous. The material I occupies the upper half plane S_1 and the material II occupies the lower half plane S_2 . The displacements u_x and u_y should be continuous across the interface. Hence the strain ϵ_x should be continuous across the interface. It follows

$$(\epsilon_x)_I = (\epsilon_x)_{II} \quad \text{on interface}$$

For a plane strain problem from above equation, we obtain directly

$$(\sigma_x)_I = \frac{\mu_1(1 - \nu_2)}{\mu_2(1 - \nu_1)}(\sigma_x)_{II} + \frac{\sigma_y}{1 - \nu_1} \left(\nu_1 - \frac{\mu_1 \nu_2}{\mu_2} \right) \quad \text{on interface} \quad (1)$$

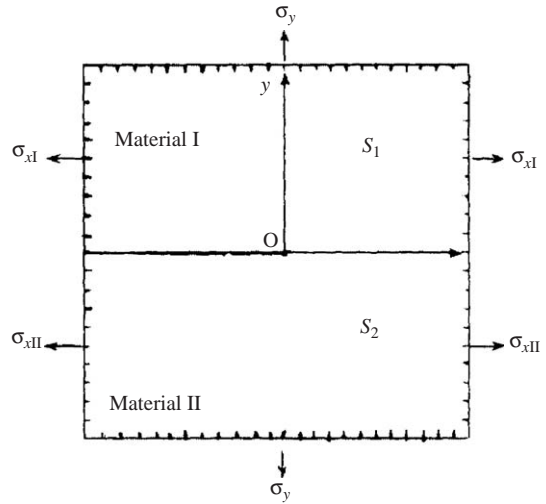


Figure 1 A bimaterial interface.

The above equation can be represented as

$$(\sigma_x)_I = \frac{1 + \alpha}{1 - \alpha}(\sigma_x)_{II} + \frac{2\sigma_y}{1 - \alpha}(2\beta - \alpha) \quad \text{on interface} \quad (2)$$

where α and β are two Dundurs' parameters

$$\alpha = \frac{(\kappa_2 + 1)/\mu_2 - (\kappa_1 + 1)/\mu_1}{(\kappa_2 + 1)/\mu_2 + (\kappa_1 + 1)/\mu_1} \quad (3)$$

$$\beta = \frac{(\kappa_2 - 1)/\mu_2 - (\kappa_1 - 1)/\mu_1}{(\kappa_2 + 1)/\mu_2 + (\kappa_1 + 1)/\mu_1}$$

where $\kappa_i = 3 - 4\nu_i$ for plane strain and $\kappa_i = (3 - \nu_i)/(1 + \nu_i)$ for plane stress, ν_i and μ_i are the Poisson ratio and the shear modulus of the respective materials. Equation (2) is also suitable for a plane stress problem.

In the plane strain case, the physically admissible values of α and β lie within a parallelogram bounded by $\alpha = \pm 1$ and $\alpha - 4\beta = \pm 1$ in the (α, β) plane. The values of α and β for representative material pairs are plotted for plane strain in Figure 2, in which the stiff material is taken as material I so that α is positive. At infinity we have

$$(\sigma_x^\infty)_I = \frac{1 + \alpha}{1 - \alpha}(\sigma_x^\infty)_{II} + \frac{2\sigma_y^\infty}{1 - \alpha}(2\beta - \alpha) \quad \text{on interface} \quad (4)$$

We should emphasize that the stress jumping Equation (4) is important for the understanding of the interface problem.

If the bimaterial system shown in Figure 1 is subjected to far-field uniform stresses, which

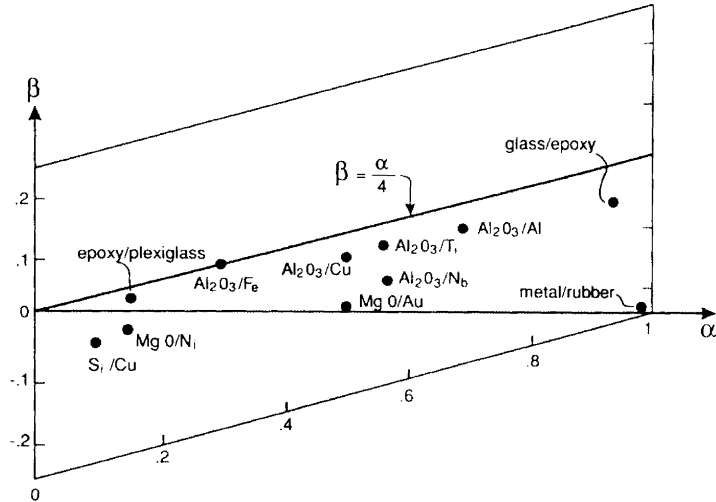


Figure 2 Values of Dundurs' parameters in-plane strain for a selected combination of materials (source Hutchinson and Suo, 1992).

satisfy Equation (4), the stress fields in materials I and II take the following forms, respectively,

$$\sigma_x = (\sigma_x^\infty)_I, \quad \sigma_y = \sigma_y^\infty, \quad \tau_{xy} = \tau_{xy}^\infty, \quad \text{in material I} \quad (5a)$$

$$\sigma_x = (\sigma_x^\infty)_{II}, \quad \sigma_y = \sigma_y^\infty, \quad \tau_{xy} = \tau_{xy}^\infty, \quad \text{in material II} \quad (5b)$$

8.03.1.2 Complex Potential

Stress and displacement in an elastic solid can be represented by two Muskhelishvili's potentials:

$$\begin{aligned} \sigma_x + \sigma_y &= 4\text{Re}\{\Phi(z)\} \\ \sigma_y - i\tau_{xy} &= \Phi(z) + \Omega(\bar{z}) + (z - \bar{z})\overline{\Phi'(z)} \quad (6) \\ 2\mu(u_x + iu_y)_{,x} &= \kappa\Phi(z) - \Omega(\bar{z}) - (z - \bar{z})\overline{\Phi'(z)} \end{aligned}$$

The complex potentials for an edge dislocation at $z = s$ in infinite elastic solid can be expressed as follows:

$$\begin{aligned} \Phi_0(z) &= \frac{B}{z - s} \\ \Omega_0(z) &= \frac{B}{z - \bar{s}} + \bar{B} \frac{s - \bar{s}}{(z - \bar{s})^2} \quad (7) \\ B &= \frac{\mu}{\pi i(\kappa + 1)}(b_x + ib_y) \end{aligned}$$

where symbols b_x and b_y are the x and y components of a dislocation.

The complex potentials for a point force at $z = s$ in infinite elastic solid can be expressed as follows:

$$\Phi_0(z) = \frac{P}{z - s}$$

$$\Omega_0(z) = \kappa \frac{P}{z - \bar{s}} - \bar{P} \frac{s - \bar{s}}{(z - \bar{s})^2} \quad (8)$$

$$P = \frac{1}{2\pi(\kappa + 1)}(P_x + iP_y)$$

where P_x and P_y are the x and y components of the force.

The interaction problem of an edge dislocation with a bimaterial interface was studied by Dundurs (1969) and Suo (1989) among others. If the edge dislocation is embedded in material II, the complex potentials are (Suo, 1989):

$$\begin{aligned} \Phi(z) &= \begin{cases} (1 + \Lambda_1)\Phi_0(z), & z \in S_1 \\ \Phi_0(z) + \Lambda_2\Omega_0(z), & z \in S_2 \end{cases} \\ \Omega(z) &= \begin{cases} \Omega_0(z) + \Lambda_1\Phi_0(z), & z \in S_1 \\ (1 + \Lambda_2)\Omega_0(z), & z \in S_2 \end{cases} \quad (9) \end{aligned}$$

$$\Lambda_1 = \frac{\alpha + \beta}{1 - \beta}, \quad \Lambda_2 = \frac{\alpha - \beta}{1 + \beta}$$

8.03.2 ELASTIC FRACTURE MECHANICS FOR AN INTERFACE CRACK

8.03.2.1 Crack Tip Fields

The singular crack tip fields were first investigated by Williams (1959) (see Chapter 2.03). Many interface crack problems have been solved by Cherepanov (1962, 1979), Erdogan (1965), England (1965), Sih and Rice (1964), and Rice and Sih (1965), among others. Take the origin at the interface crack tip as shown in Figure 3, the crack lies along the

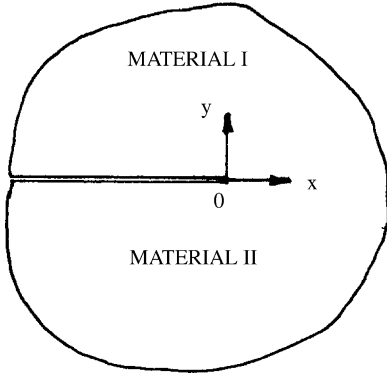


Figure 3 An interface crack.

interface of two dissimilar materials. The singular crack tip fields for plane strain and plane stress problems are

$$\sigma_{\alpha\beta} = \frac{1}{\sqrt{2\pi r}} \left\{ \text{Re}(Kr^{i\varepsilon})\sigma_{\alpha\beta}^{\text{I}}(\theta) + \text{Im}(Kr^{i\varepsilon})\sigma_{\alpha\beta}^{\text{II}}(\theta) \right\} \quad (10)$$

where $i = \sqrt{-1}$, r , and θ are polar coordinates. The complex interface stress intensity factor, $K = K_1 + iK_2$, has a real and an imaginary part, K_1 and K_2 , respectively. The angular distribution functions $\sigma_{\alpha\beta}^{\text{I}}$ and $\sigma_{\alpha\beta}^{\text{II}}$ were given by Rice *et al.* (1990). The traction ahead of the crack tip is given by

$$\sigma_{22} + i\sigma_{12} = \frac{K}{\sqrt{2\pi r}} r^{i\varepsilon} \quad (11)$$

where $r^{i\varepsilon} = \cos(\varepsilon \ln r) + i \sin(\varepsilon \ln r)$ is the oscillatory singularity. From Equation (11), one can find that the stress field ahead of the crack tip has not only the square root singularity $r^{-1/2}$ but also the oscillatory singularity. As r approaches zero, the stress fields undergo an infinite number of sign reversals. The oscillatory index has the expression:

$$\varepsilon = \frac{1}{2\pi} \ln \frac{1 - \beta}{1 + \beta}$$

The relative crack opening displacements a distance r behind the crack tip take the form

$$\delta_2 + i\delta_1 = \frac{8K}{(1 + 2i\varepsilon) \cosh(\pi\varepsilon) E_*} \sqrt{\frac{r}{2\pi}} r^{i\varepsilon}, \quad (12)$$

$$E_* = \frac{2\bar{E}_1 \bar{E}_2}{\bar{E}_1 + \bar{E}_2}$$

where $\bar{E} = E/(1 - \nu^2)$ for plane strain and $\bar{E} = E$ for plane stress.

The above formula predicts wrinkling of crack faces and overlapping of the materials, which would contradict the assumption that the crack faces are traction free (England 1965;

Malyshev and Salganik 1965). Since the crack contact zone is very small for pure tension remote loading, one can argue that the complicated issues arising from oscillatory singularity are not important for fracture process.

The energy release rate G can be expressed as

$$G = \frac{1 - \beta^2}{E_*} (K_1^2 + K_2^2) \quad (13)$$

For a center cracked panel subjected to remote loading, the complex stress intensity factor is

$$K = (\sigma_y^\infty + i\tau_{xy}^\infty) (1 + 2i\varepsilon) \sqrt{\pi a} (2a)^{-i\varepsilon}$$

K_1 and K_2 depend on the elastic mismatch only through the oscillatory index ε and are independent of parameter α . In other words, the stress fields ahead of the crack tip only depend on one Dundurs' parameter β .

8.03.2.2 Interface Toughness with $\beta = 0$

The oscillatory index ε vanishes when $\beta = 0$. Then the stress field ahead of the crack tip only has the conventional square root singularity $r^{-1/2}$. Equation (11) becomes

$$\sigma_{22} = \frac{K_1}{\sqrt{2\pi r}}, \quad \sigma_{12} = \frac{K_2}{\sqrt{2\pi r}} \quad (14)$$

The stress intensity factors K_1 and K_2 play the same role as their counterparts in elastic fracture mechanics of homogeneous media. K_1 characterizes the amplitude of normal stress singularity, while K_2 describes the amplitude of the shear stress singularity. Meanwhile, the elastic mismatch has no direct effect on the singular stress field ahead of the crack tip. The bimaterial system can be treated as a homogeneous solid with effective Young's modulus E_* . The mode mixity can be defined as

$$\psi = \tan^{-1}(K_2/K_1)$$

For the center cracked panel:

$$\psi = \tan^{-1}(\tau_{xy}^\infty/\sigma_y^\infty)$$

An interface is typically a plane of low fracture toughness; the crack tends to propagate along the interface despite the bimaterial system being subject to mixed mode loading. Many experiments have shown that interfacial toughness strongly depends on the mode mixity.

Trantina (1972) presented the first experimental evidence of interface fracture toughness that increases with increasing shear mode. He

carried out the experiments with adhesive bonded scarf joints (aluminum/epoxy system) that failed along the adhesive. Using cone, blister, and peel specimens, Anderson *et al.* (1974) observed similar trends. Liechti and Chai (1991, 1992) measured the interface fracture toughness of a glass/epoxy system over a wide range of mode mixities. They found that by applying displacements along clamped boundaries $x_2 = \pm h$, the interface fracture toughness increases remarkably with increasing positive or negative in-plane shear component.

Using symmetric and asymmetric double cantilever beams, Cao and Evans (1989) studied an epoxy/glass system. Wang and Suo (1990) examined an epoxy layer on metal and plexiglass substrates. All these systems exhibit rapidly increasing interface fracture toughness at large shear mode components. O'Dowd *et al.* (1992) investigated the mixed-mode interface fracture toughness of an alumina/niobium system using four-point shear specimens. They found the fracture toughness of alumina is relatively insensitive to the mode mixity. In contrast, the fracture toughness of the alumina–niobium interface depends strongly on the mode mixity. Various aspects of interface fracture toughness can be found in papers by Charalambides *et al.* (1989), Rice *et al.* (1990), Shih (1991), Hutchinson and Suo (1992), and in a volume edited by Ruhle *et al.* (1990). Extensive reviews of fracture in thin film and interface were given by Evans and Hutchinson (1995) and Hutchinson and Evans (2000).

The criterion to initiate crack propagation along an interface when the interfacial crack is subject to in-plane mixed mode loading, is

$$G = \Gamma(\psi) \quad (15)$$

where the interface fracture toughness $\Gamma(\psi)$ should be measured by specially designed bimaterial specimens. The energy release rate G can be thought of as a force driving the interfacial crack propagation, while $\Gamma(\psi)$ is the resistance to that. Fracture toughness data from Wang and Suo (1990) in a layer of plexiglass/epoxy sandwiched between two halves of a Brazil nut specimen are shown in Figure 4. For the plexiglass/epoxy system $\alpha = -0.15$, $\beta = -0.029$, $\varepsilon = 0.009$. Since the value of ε is very small, one can assume that the bimaterial system has $\varepsilon = 0$. The error in G due to this approximation is less than 0.1%.

8.03.2.3 Interface Toughness with $\beta \neq 0$

When $\beta \neq 0$, the tractions on the interface directly ahead of the crack tip are given by

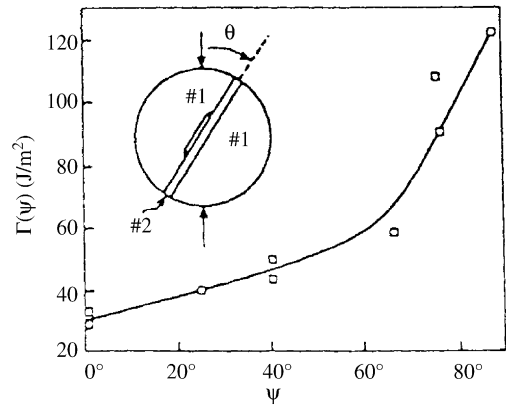


Figure 4 Interfacial fracture toughness of plexiglass/epoxy sandwich (source Wang and Suo, 1990).

Equation (11). The contact zone should be considered. As long as the contact zone size is very small, the complex stress intensity factor K provides a unique characterization of the crack tip fields. As pointed out by Rice (1988), the oscillatory singularity leads to a complicated issue, since the ratio of the shear traction to the normal traction directly ahead of the crack tip slowly varies with r approaching zero. One cannot uniquely define the proportion of “mode II” to “mode I.” A generalized interpretation of the mode mixity is needed. Let us introduce a reference length l for the definition of the phase angle, i.e., $\tan \hat{\psi} = \text{Im}(Kl^{ie})/\text{Re}(Kl^{ie})$. From Equation (11), one obtains $\tan \hat{\psi} = (\tau_{xy}/\sigma_y)_{r=l}$. The choice of the reference length is somewhat arbitrary. Generally speaking there are two choices. The first is based on the length scale L of the specimen geometry, such as the crack length. The second choice is based on the length scale intrinsic to the materials, such as the size of the fracture process zone or the intensive plastic zone. The complex stress intensity factor K for an interface crack has the form $K = FTL^{1/2}L^{-ie}\exp(i\psi)$, where T is a representative amplitude of the applied load, F and ψ are dimensionless real numbers which depend on specimen geometry and the external loading. Now ψ is the phase angle of KL^{ie} .

Fracture toughness data can be reported as a function of $\hat{\psi}$ based on l . Using a simple phase translation formula, one can express the phase angle $\hat{\psi}$ as $\hat{\psi} = \psi + \varepsilon \ln(l/L)$. The criterion for initiation of crack propagation along an interface can be given as

$$G = \Gamma(\hat{\psi}, l) \quad (16)$$

If the value of l is broadly representative of the relevant microstructure length, the term $\Gamma(\hat{\psi})$ can be interpreted as the intrinsic interface

fracture toughness for a given material pair. The phase angle $\hat{\psi}$ provides an intrinsic measure of mode mixity and the interface toughness data from different crack geometries can collapse on to a single toughness curve against mode mixity $\hat{\psi}$.

Figure 5 shows the fracture toughness data for an epoxy/glass interface measured by Liechti and Chai (1992). The interface parameters are $E_1 = 2.07$ GPa, $E_2 = 68.9$ GPa, $\nu_1 = 0.37$, $\nu_2 = 0.20$, $\alpha = -0.935$, $\beta = -0.188$, and $\varepsilon = 0.060$. They took $l = 12.7$ mm. The plastic zone in the epoxy observed by them is approximately on the order of $1 \mu\text{m}$ for $\hat{\psi} \approx 0^\circ$ and $140 \mu\text{m}$ for $\hat{\psi} \approx 90^\circ$. Hutchinson and Suo (1992) found that if instead of $l = 12.7$ mm, l is chosen to be two orders of magnitude smaller ($l = 127 \mu\text{m}$), the shift in the $\hat{\psi}$ -origin is -15.8° . Then the $\hat{\psi}$ origin is placed approximately at the minimum of $\Gamma(\hat{\psi}, l)$ and roughly centers the data.

8.03.2.4 Kinking Out of an Interface

Consider a branch crack segment of a length a , which makes an angle Ω with the main crack in a homogeneous solid. Prior to kinking the main crack is loaded with a complex stress intensity factor $K = K_1 + iK_2$, and a T -stress on the tip when $a = 0$.

The stress intensity factors K_1^{kink} and K_2^{kink} can be expressed as

$$\begin{aligned} K_1^{\text{kink}} &= c_{11}K_1 + c_{12}K_2 + b_1Ta^{1/2} \\ K_2^{\text{kink}} &= c_{21}K_1 + c_{22}K_2 + b_2Ta^{1/2} \end{aligned} \quad (17)$$

The coefficients c_{ij} are given by Hayashi and Nemat-Nasser (1981) (see also Karihaloo,

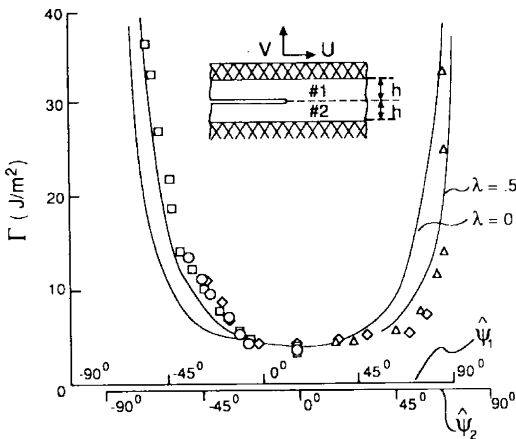


Figure 5 Interface fracture toughness for an epoxy/glass interface measured by Liechti and Chai (1992) (reproduced by permission of Academic Press from “Advances in Applied Mechanics,” vol. 29, pp. 63–191).

1982), and b_i are given by He and Hutchinson (1989). The energy release rate G^{kink} at the tip of the branch crack is $G^{\text{kink}} = [(K_1^{\text{kink}})^2 + (K_2^{\text{kink}})^2]/\bar{E}$. The energy release rate G for the main crack when it advances straight ahead is $G = (K_1^2 + K_2^2)/\bar{E}$.

For a given mode mixity ψ , one can find the maximum value $G_{\text{max}}^{\text{kink}}$ with respect to Ω . The kinking angle $\hat{\Omega}$ at which G^{kink} is maximized, is a function of ψ . The function $\hat{\Omega}(\psi)$ is given by He and Hutchinson (1989) and plotted in Figure 6(a). Figure 6(b) shows the ratio of strain energy release rate for straight-ahead growth to the maximum energy release rate for a branched crack, $G/G_{\text{max}}^{\text{kink}}$, as a function of ψ . As pointed out by He and Hutchinson (1989), the kinking angle that maximizes G^{kink} nearly coincides with the kinking angle for which $K_2^{\text{kink}} = 0$. Since the calculation for maximum energy release rate $G_{\text{max}}^{\text{kink}}$ is more complex than the calculation of the stress intensity factors K_1^{kink} and K_2^{kink} , it is convenient to use a criterion based on propagation in the direction for which $K_2^{\text{kink}} = 0$.

For an interface crack as shown in Figure 7, the conventional stress intensity factors K_1^{kink} and K_2^{kink} at the tip of branched crack take the form

$$K_1^{\text{kink}} + iK_2^{\text{kink}} = cKa^{ie} + d\bar{K}a^{-ie} + bTa^{1/2} \quad (18)$$

The coefficients c , d , and b are the functions of Ω , α , and β which are tabulated in He and Hutchinson (1989) and He *et al.* (1991). The energy release rate $G_{\text{max}}^{\text{kink}}$ is also a function of Ω and (α, β) . The ratio $G/G_{\text{max}}^{\text{kink}}$ is plotted against ψ in Figure 8 for the case of $\beta = 0$ and $\eta = 0$. Let $\Gamma(\psi)$ denote the interface fracture toughness and Γ_c denote the fracture toughness of material II under mixed mode loading, kinking will be favored if $G/G_{\text{max}}^{\text{kink}} < \Gamma(\psi)/\Gamma_c$.

8.03.2.5 Mechanics Models of an Interface Crack

According to Equation (12), interpenetration of two crack faces occurs at sufficiently small r . The normal opening displacement $\delta_y = \delta \cos[\psi - \tan^{-1}(2\varepsilon) - \varepsilon \ln(L/r)]$. The largest r for which the opening displacement δ_y turns to negative is $r_c = L \exp\{-[\pi/2 + \psi - \tan^{-1}(2\varepsilon)]/\varepsilon\}$, for $\varepsilon > 0$, where L is the crack length. If $|\psi| < \pi/4$ and $|\varepsilon| < 0.03$, then $r_c/L < 10^{-8}$, the contact zone size is much smaller than all physically relevant length scales. If $|\psi| \approx \pi/2$, the contact zone size is comparable with the crack length. Therefore, one cannot neglect the effect of the contact zone on stress and displacement fields near a crack tip.

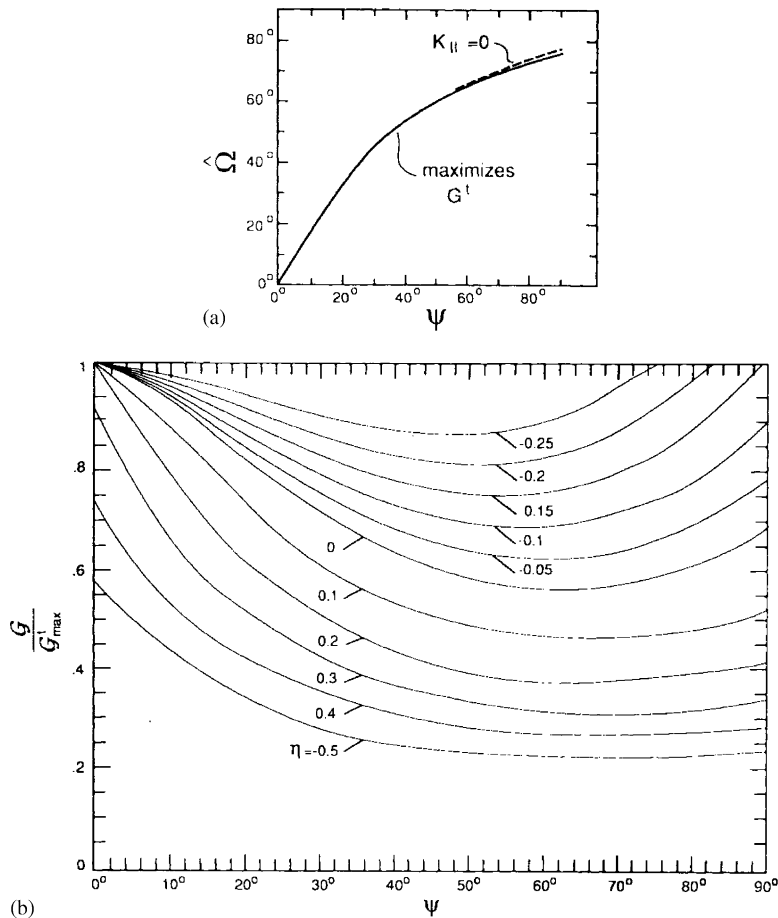


Figure 6 A kinked crack in homogeneous material: (a) kink angle as predicted by two criteria and (b) ratio of energy release rate for straight-ahead advance to maximum energy release rate for a kinked crack as a function of $\psi = \tan^{-1}(K_{II}/K_I)$. Here $G'_{max} = G'_{max}^{kink}$ and $\eta = T\sqrt{a/\bar{E}G}$ (reproduced by permission of the American Ceramics Society from *J. Am. Ceram. Soc.*, 1991, **74**, 767–771).

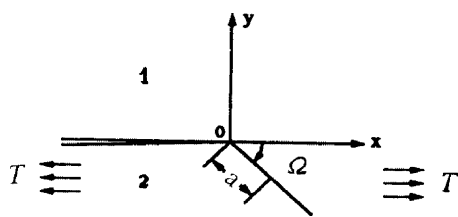


Figure 7 A branched interface crack.

Comninou (1977) and Comninou and Schmueser (1979) proposed the contact zone model to eliminate the oscillatory singularity. As shown in Figure 9, behind the crack tip, there is a contact zone in which the gap δ_y vanishes and the normal stress σ_y becomes negative. The oscillatory singularity and the overlap of the crack faces are eliminated in their solutions. But Comninou’s solution is quite different from the classical K field as described below.

Ahead of the crack tip, the normal stress is finite and the shear stress has the square root singularity $r^{-1/2}$. Behind the crack tip, the compressive normal stress σ_y has the square root singularity $r^{-1/2}$. They found that the contact zone size is extremely small under remote tension loading in comparison with the crack length.

The interfacial layer model proposed by Atkinson (1977) is depicted in Figure 10. The crack could be embedded in the layer or could lie on the interface between the layer and the material I or the material II. In the latter case the material properties of the interfacial layer should be chosen such that the Dundurs’ parameter $\beta = 0$ at the tip of the interface crack.

Delale and Erdogan (1988) improved Atkinson’s model. They argued that the interfacial layer is an inhomogeneous medium. The Young modulus E and the Poisson ratio ν in the interfacial layer vary continuously from the

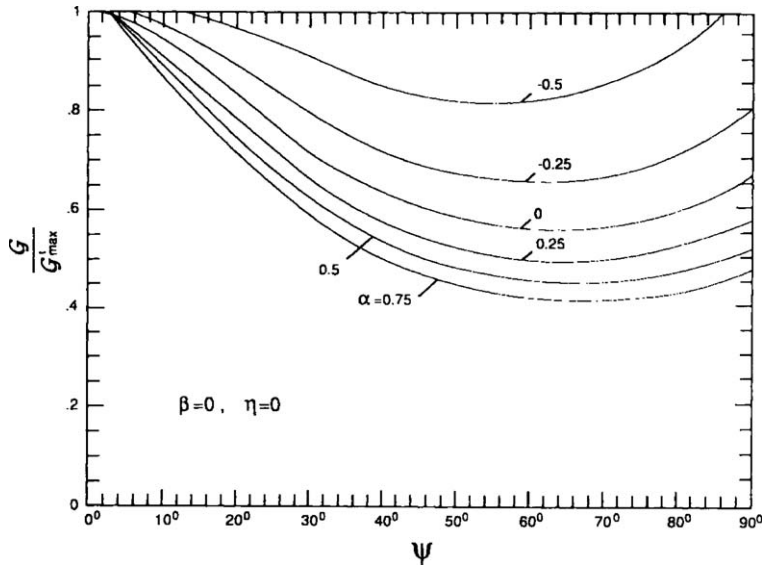


Figure 8 Ratio of energy release rate for advance in the interface to the maximum energy release rate for the kinked crack for various levels of elastic mismatch, all with $\beta = 0$. Here $G_{max}^t = G_{max}^{kink}$ and $\eta = T\sqrt{a}/\sqrt{EG}$ (source He *et al.*, 1991).

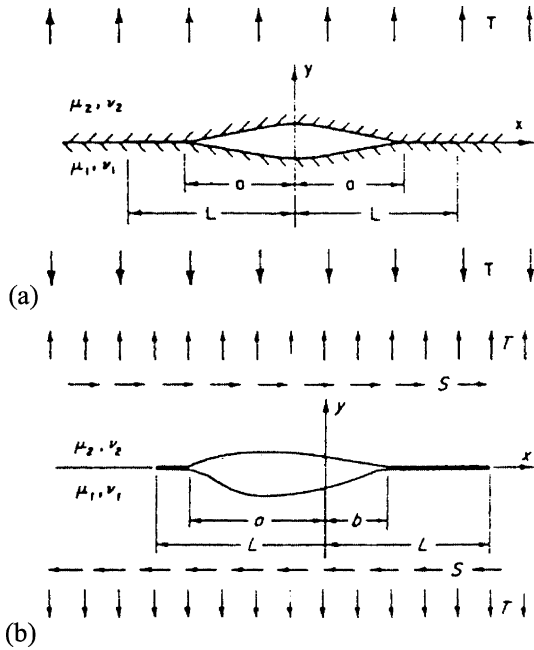


Figure 9 A crack surface contact model: (a) pure tension loading and (b) tension and shear combined loading (after Comninou, 1977).

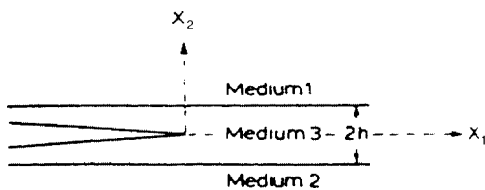


Figure 10 An interfacial layer model for interface crack (after Atkinson, 1977).

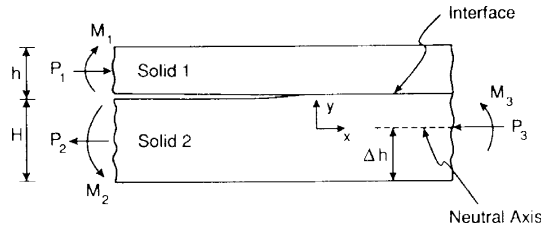


Figure 11 A bilayer with a half-plane interface crack. The neutral axis of the composite layer is indicated (source Hutchinson and Suo, 1992).

upper interface to the lower interface so that the discontinuity in elastic properties vanishes across the upper interface and the lower interface.

8.03.3 TYPICAL INTERFACE FRACTURE PROBLEMS

8.03.3.1 Film Decohesion

A cross-section of the interface of an infinite bilayer with a semi-infinite plane crack along the interface is shown in Figure 11. Both materials are homogeneous isotropic elastic materials. The uncracked interface is assumed to be perfectly bonded with continuous displacements and tractions. The bimaterial system is subjected to forces and moments along three edges. The problem was solved by Suo and Hutchinson (1990). Far ahead of the crack tip, the bimaterial system is treated as a composite beam. The neutral axis lies a distance $h \cdot \Delta$ above the bottom of beam, the quantity Δ was given in their paper.

A close form solution of the energy release rate for the crack advance along an interface was obtained. The complex stress intensity factor K takes the form $K = h^{-i\epsilon} F e^{i\omega}$, where F is the function of P_i and $M_i, i = 1, 2, 3$. An explicit formula for F was given in their paper. The angle ω is a function of the Dundurs' parameters α, β , and relative height $\eta = h/H$, which was tabulated by Suo and Hutchinson (1990). Some typical results are plotted in Figure 12.

8.03.3.1.1 Film decohesion from edges or channels

Figure 13 depicts a pre-tensioned film. The edge load can be identified as $P_1 = P_3 = \sigma h, M_3 = (1/2 + 1/\eta - \Delta)\sigma h^2, P_2 = M_1 = M_2 = 0$. The phase angle ψ is defined as $K = |K|/h^{-i\epsilon} \exp(i\psi)$, which is shown in Figure 13. The energy release rate is shown in Figure 14. Since the film thickness h is much smaller than the thickness of the substrate, the decohesion process is inherently mixed mode. The sliding mode will be stronger than the opening mode.

8.03.3.1.2 Decohesion from a hole

A decohesion crack emanating from the edge of a hole in a pre-tensioned film is shown in Figure 15. The energy release rate is equal to $G = h\sigma^2/2\bar{E}_f k^2$, where k was given by Suo and Hutchinson (1990). When $(b - b_0)/h$ is sufficiently large, the mode mixity is independent of b_0/b . Farris and Bauer (1988) and Jensen *et al.* (1990) used this kind of film decohesion to

measure the interface toughness. The decohesion radius b can be easily measured.

8.03.3.1.3 Effects of plasticity and segregation

As pointed out by Evans *et al.* (1999), the decohesion at an interface between a thin film and a thick substrate is strongly affected by the plasticity and segregation. Two types of measurements are important to film decohesion:

- (i) the energy dissipated per unit area ($J m^{-2}$) which has the same role as the fracture toughness in homogeneous materials (Evans and Dalgliesh, 1992); and
- (ii) the critical stress at which the interface separates (Gupta *et al.*, 1992).

Figure 16 illustrates the schematic of three basic mechanisms of the film decohesion. In mechanism I, the crack remains atomically sharp. Mechanisms II and III occur in company with crack blunting. Mechanism II involves a fracture process zone on the interface. The fracture process zone is comprised by debonds, voids, and their coalescence. Mechanisms I and II exhibit resistance curve behavior with steady-state toughness trends. Mechanism III involves the injection of crack onto the interface from weak patches ahead of a stationary crack.

Interfaces usually can be made by bonding procedures, such as diffusion bonding or brazing. The residual stresses intrinsically exist and play an important role in determining the energy release rate G and mode mixity (Charalambides *et al.*, 1989; Jensen and Thouless, 1993).

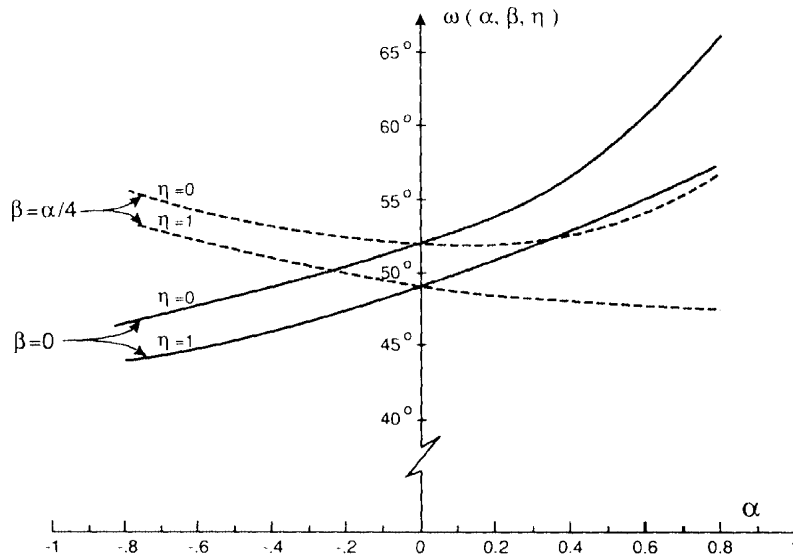


Figure 12 The values of the function $\omega(\alpha, \beta, \eta)$ (source Hutchinson and Suo, 1992).

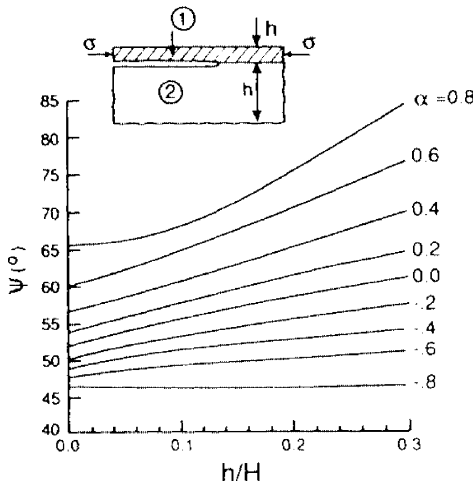


Figure 13 Mode mixity for a debonding crack (source Hutchinson and Suo, 1992).

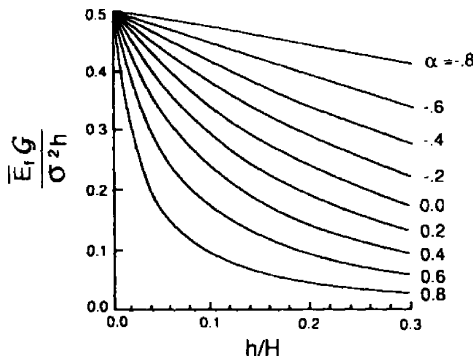


Figure 14 Energy release rate for a debonding crack (source Hutchinson and Suo, 1992).

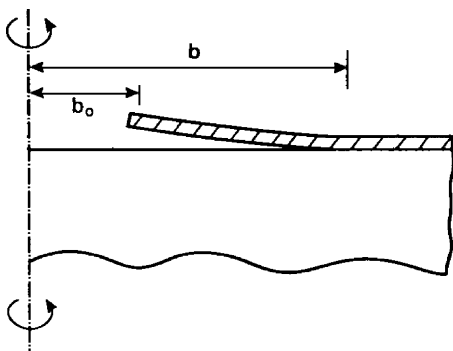


Figure 15 An axial-section of a decohesion annulus originating from an edge of a circular cut (source Hutchinson and Suo, 1992).

Much work about decohesion mechanism has been obtained from metal/oxide interfaces by Evans and Dalgliesh (1992), Turner *et al.* (1995), Gaudette *et al.* (1997), Reimanis *et al.* (1997), Lipkin *et al.* (1998), among others.

The major conclusions are:

(i) Clear interfaces are much benefited on the toughness and ductility of the interfaces. The high adhesion could be realized even though the metal is polycrystalline solid or nonepitaxial layer.

(ii) A systematic infusion of a contaminant on a clean interface can clearly demonstrate the role of contaminants and segregants on the interface toughness of the interfaces.

(iii) The fracture toughness with a clear interface is much higher than that of the oxide. The critical energy release rate G_c can achieve $\sim 200\text{--}400\text{ J m}^{-2}$ for the metal/sapphire system with a clear interface, despite a much smaller critical value for the oxide $\Gamma_{\text{oxide}} \cong 10\text{--}20\text{ J m}^{-2}$, (Elssner *et al.*, 1994; McNaney *et al.*, 1996; Reimanis *et al.*, 1997; Gaudette *et al.*, 1997). Such findings reveal that the metal/oxide interfaces are inherently strong.

The elastic-plastic mechanics for thin film decohesion has been studied by Tvergaard and Hutchinson (1992, 1993), and Wei and Hutchinson (1997a, 1997b). There are three models to describe the influence of plasticity on interface toughness.

(i) *The embedded fracture process zone model*

The embedded fracture process zone (EPZ) model was proposed by Needleman (1987), and by Tvergaard and Hutchinson (1992, 1993). In the EPZ model, a traction-separation law characterizing the interface fracture process is employed as a boundary condition along the interface. The fracture process zone lies between the plastic zone on the metal thin film side of the interface and the elastic substrate on the other side. Once the parameters of the traction-separation law are specified the fracture resistance curve can be obtained using the EPZ model. Following Tvergaard and Hutchinson (1992), a material-based length parameter is introduced as $R_0 = E\Gamma_0/3\pi(1 - \nu^2)/\sigma_Y^2$, where E and σ_Y are the Young modulus and yield stress of the film, respectively. Γ_0 is the work of separation per unit area of the interface which is consumed by the near tip fracture process.

Suppose the films are bonded to, or deposited on, an elastic substrate at an elevated temperature and then cooled. Films are subjected to equi-biaxial tension σ_0 . The critical energy release rate $G_c = F\Gamma_0$, where F is the function of stress hardening exponent N , the phase angle and the peak separation stress $\hat{\sigma}$ for interface under a strict pure mode I opening. The parameters Γ_0 and $\hat{\sigma}$ characterize the separation law of the interface. Based on this model, the crack growth resistance $\Gamma_R(\Delta a)$

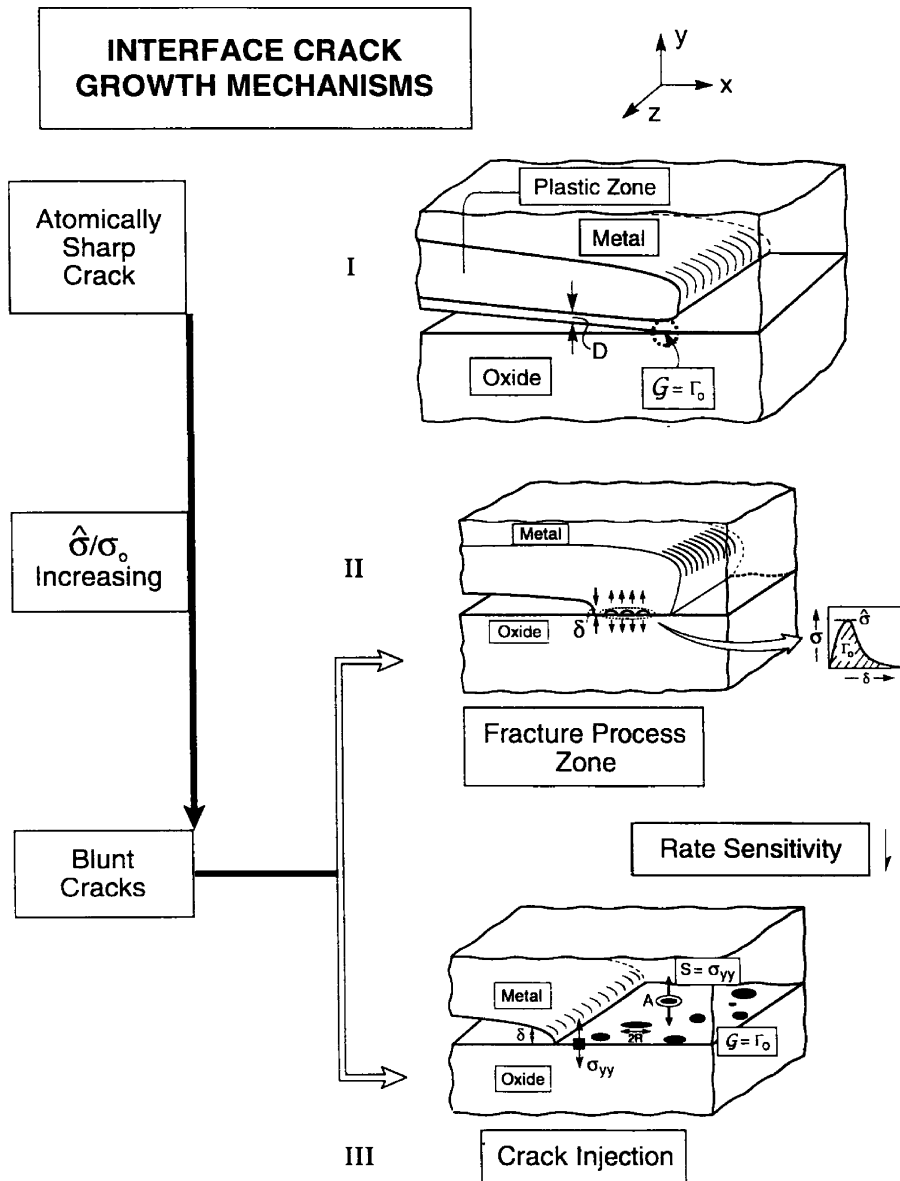


Figure 16 A schematic of three basic mechanisms that control interface crack growth (source Evans *et al.*, 1999).

can be computed in terms of $\Gamma_0, \hat{\sigma}$, and the mechanical properties of the metal film and substrate. In particular, one can get the steady-state toughness Γ_{ss}/Γ_0 .

The critical energy release rate in the steady state, G_c , versus $\hat{\sigma}/\sigma_Y$ is plotted on Figure 17(a) for the EPZ model (Wei and Hutchinson, 1997a). One can find that the critical energy release rate G_c increases rapidly as the $\hat{\sigma}/\sigma_Y$ increases. Meanwhile the strain hardening has a significant effect on the G_c . The effect of σ_Y/E seems to be small in comparison with the effect of $\hat{\sigma}/\sigma_Y$ and N .

(ii) The SSV model

The SSV model is proposed by Suo *et al.* (1993). The model assumes that dislocations are not emitted at the crack tip and imposes an elastic zone of height D above the interface in the metal film. Plastic deformation occurs outside the near tip elastic zone. Since the crack tip is surrounded by an elastic zone, the crack tip remains atomically sharp and the stresses have the square root singularity $r^{-1/2}$. Hence the resistance to crack advance is mainly the separation work of the interface. The critical energy release rate at the crack tip G_c

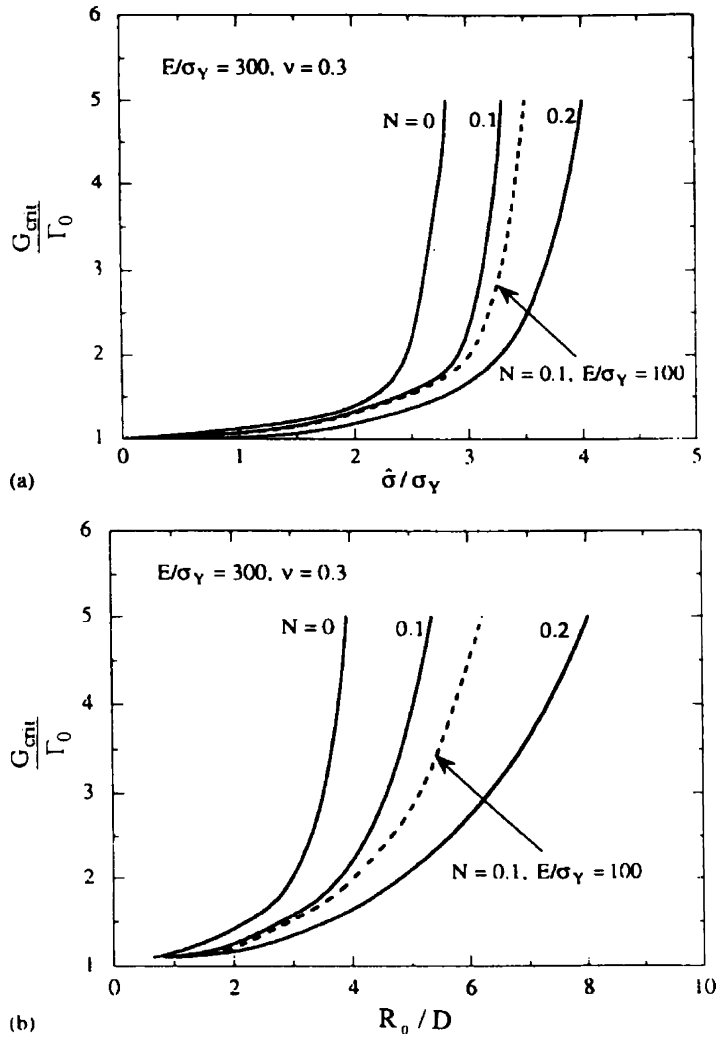


Figure 17 Critical values of G for films that yield plastically: (a) EPZ model and (b) SSV model (source Wei and Hutchinson, 1997a).

should be equal to the adhesion work. This criterion fully characterizes this model. The parameter D is a fitting parameter. The critical energy release rate in the steady state is $G_c = F\Gamma_0$, where F is the function of stress hardening exponent N and the nondimensional parameter D/R_0 . Plots of G_c/Γ_0 as a function of R_0/D are shown in Figure 17(b) (Wei and Hutchinson, 1997a). The parameter R_0/D plays a role similar to $\hat{\sigma}/\sigma_Y$ in the EPZ model. When this parameter is larger than a certain value, depending on N , G_c/Γ_0 increases sharply.

For mode I loading, the steady-state toughness Γ_{ss}/Γ_0 is plotted against $\hat{\sigma}/\sigma_Y$ in Figure 18, where $\hat{\sigma} = \sqrt{E\Gamma_0/D}$. Note that the adhesion index, Γ_{ss}/Γ_0 , refers to steady state for mechanisms I and II, but Γ_c/Γ_0 refers to initiation for mechanism III. The notation DBT refers to a transition condition to fracture

into an adjoining material rather than along the interface. At strength indices above this transition, the interface mechanism no longer operates.

It is worth noting that the Γ_{ss}/Γ_0 ratio becomes unbounded as D approaches zero. The reason is that the criterion of SSV model cannot be employed and the energy release rate at the crack tip always equals zero, if the plastic deformation extends to the crack tip.

(iii) A unified model

As pointed out by Wei and Hutchinson (1999), the EPZ model fails to provide realistic predictions when the peak stress $\hat{\sigma}$ is at high levels. The EPZ model predicts essentially unbounded toughness if the peak stress of the interface exceeds a high level (e.g., $\hat{\sigma}/\sigma_Y \cong 5$ for $N = 0.2$). Alternatively, in the SSV model, the

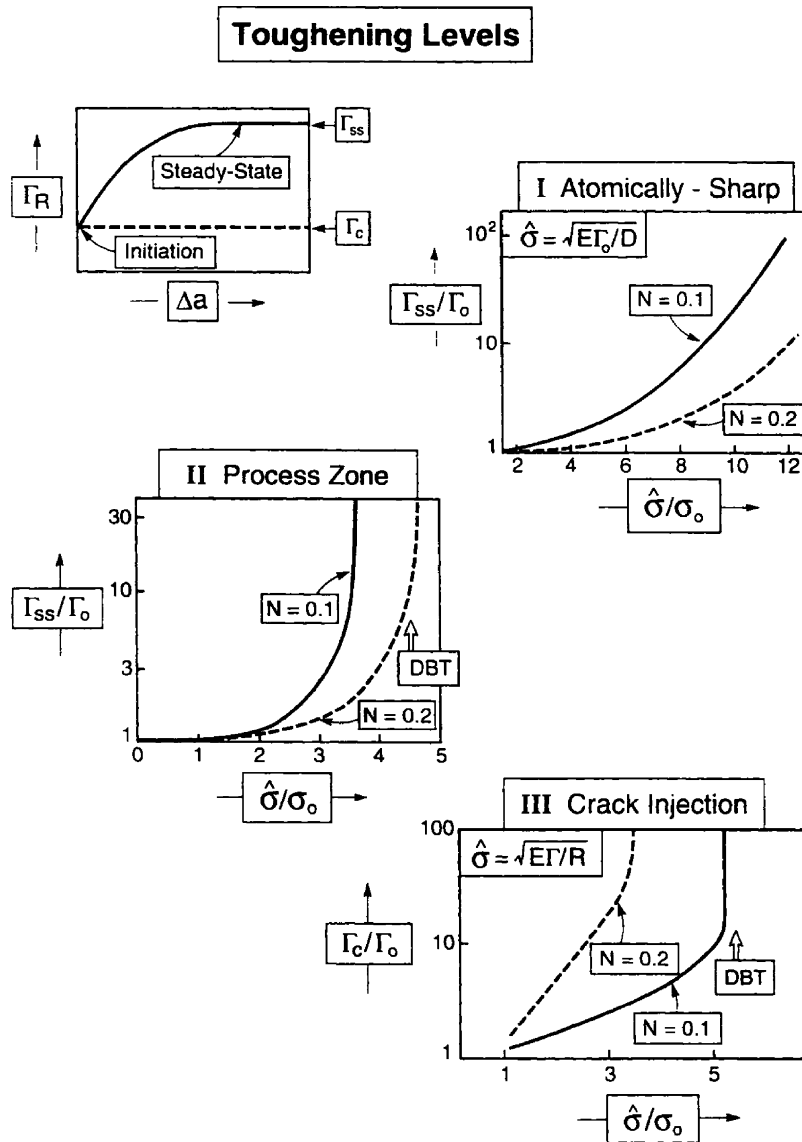


Figure 18 Characteristic toughness features. These are compared and contrasted by using common adhesion indices, where $\sigma_0 = \sigma_Y$ (source Evans *et al.*, 1999).

traction on the interface is unbounded as the tip is approached. The unified model proposed by Wei and Hutchinson (1999) incorporates both the elastic zone of thickness D in the metal film above the interface and the traction-separation law at the interface immediately ahead of the crack tip. They assumed that the length of separation would be sufficiently small compared to D . The stress in the separation zone should not exceed the peak stress $\hat{\sigma}$. The interface is characterized by the adhesion energy Γ_0 , the peak stress $\hat{\sigma}$, and the width D of the dislocation free zone. Figure 19 shows the steady-state toughness Γ_{ss}/Γ_0 against $\hat{\sigma}/\sigma_Y$ for mode I loading based on the unified model. The dashed curves included in each of these

figures are the results for the EPZ model. The limiting value corresponding to the SSV model is also depicted in these figures for each value of R_0/D . The unified model approaches the SSV model for large $\hat{\sigma}/\sigma_Y$. Meanwhile the unified model approaches the EPZ model as D approaches zero.

8.03.3.2 Cracking in Films

8.03.3.2.1 Crack patterns in the film

First we discuss the residual stress due to thermal mismatch. The film-substrate is stress free at high temperature T_0 (processing at high temperature). When the system cools to room

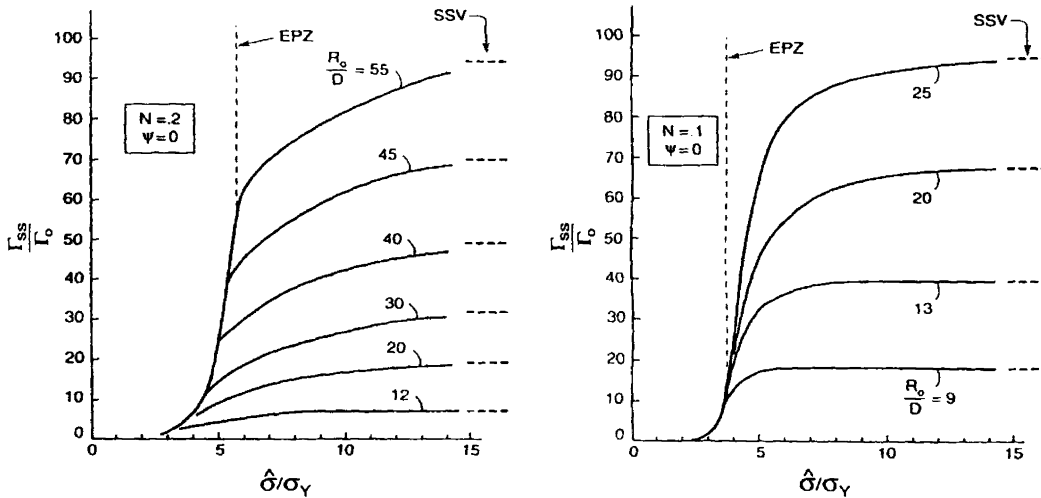


Figure 19 The ratio of the macroscopic work of fracture to work of separation, Γ_{ss}/Γ_0 , for the unified model for mode I ($\psi = 0$) steady-state crack growth along a bimaterial interface joining an elastic-plastic solid to a rigid solid. The parameters used in carrying out the calculations are $\nu = 0.3$, $\lambda_1 = 0.15$, $\lambda_2 = 0.5$, and $\delta_n^C/\delta_f^C = 1$ (source Wei and Hutchinson, 1999).

temperature T_r , the contraction strains in the film and substrate would differ by $(\alpha_f - \alpha_s)(T_0 - T_r)$, where α_f and α_s are the thermal expansion coefficients of the film and substrate, respectively. A biaxial residual stress can be defined as $\sigma = (\alpha_f - \alpha_s)(T_0 - T_r)E_f(1 - \nu_f)$. When $\alpha_f > \alpha_s$, one has $\sigma > 0$. This residual stress is quite large, e.g., if $(T_0 - T_r) = 500$ K, $\sigma \cong 500$ MPa for most materials. This implies that if the same amount of biaxial residual stress is applied to edges of the film, the film and the substrate could be bonded together without a misfit strain. Then the film is under a uniform biaxial stress σ and the substrate is stress free. Now an opposite uniform biaxial stress $-\sigma$ is applied on the edges of the film in order to release the traction on the edges of the film. Since the film thickness is very small compared with the substrate thickness, one can imagine that the perturbed stresses caused by the opposite biaxial stress on the edges of the film are negligibly small in the central part of the film when compared with σ . The perturbed stresses are comparable with σ only at the edges of a film.

The biaxial residual stress σ can cause cracking in the film, then the crack can grow through the film, arrest at the interface, or penetrate into the substrate. Different cracking patterns are formed in the film as sketched in Figure 20. The crack can propagate in the film, substrate, or along the interface. The fracture resistances of the film, substrate and interface are denoted by Γ_f , Γ_s and Γ_i , respectively.

The energy release rate takes the forms $G = Z\sigma^2 h(1 - \nu_f)/E_f$, where the parameter Z is a

dimensionless driving force, which depends on the cracking patterns and the Dundurs' parameters. For the case of $\alpha = \beta = 0$ (the film and substrate are homogeneous elastic media), the parameter Z is also listed in Figure 20 (see Hutchinson and Suo, 1992; Evans *et al.*, 1989).

The crack can be initiated from a surface flaw. If the crack size is much smaller than the film thickness, the crack front runs both toward the interface and laterally in the film. The driving force parameter Z is high for a surface crack ($Z = 3.951$), but the fracture resistance Γ_f is usually much higher than Γ_i or Γ_s . Hence the surface crack could be isolated, stabilized, and not connected. A crack channel could form sometimes. Once the channel process activates, it causes unstable propagation and arrests at another channel or passes through the edge of the film. A connected channel network would form. For most engineering applications, such a channel network is not acceptable. But such crack channels are quite common if the film is brittle. Surface cracks may penetrate into the substrate. Since the residual stress is mainly localized in the film, the penetrated crack will arrest at a certain depth. However, the crack may turn and run parallel to the interface, leading to spalling of the substrate.

8.03.3.2.2 Surface crack

We start by studying the situation of a plane strain crack as shown in Figure 21. The problem was solved by Gecit (1979) and Beuth (1992). The dimensionless stress intensity

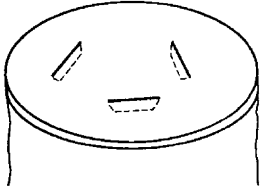
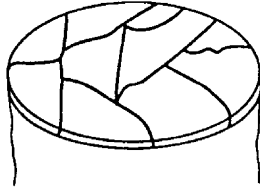
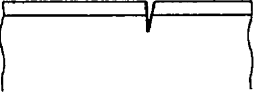
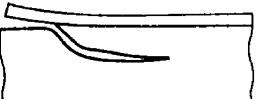

Cracking Patterns	$G = Z \sigma^2 h / \bar{E}_1$
	Surface Crack $Z = 3.951$
	Channeling $Z = 1.976$
	Substrate Damage $Z = 3.951$
	Spalling $Z = 0.343$
	Debond $Z = \begin{cases} 1.028 & \text{(initiation)} \\ 0.5 & \text{(steady - state)} \end{cases}$

Figure 20 Commonly observed cracking patterns. The dimensionless driving force for each pattern is listed, assuming that the film-substrate is elastically homogeneous and the substrate is infinitely thick (source Hutchinson and Suo, 1992).

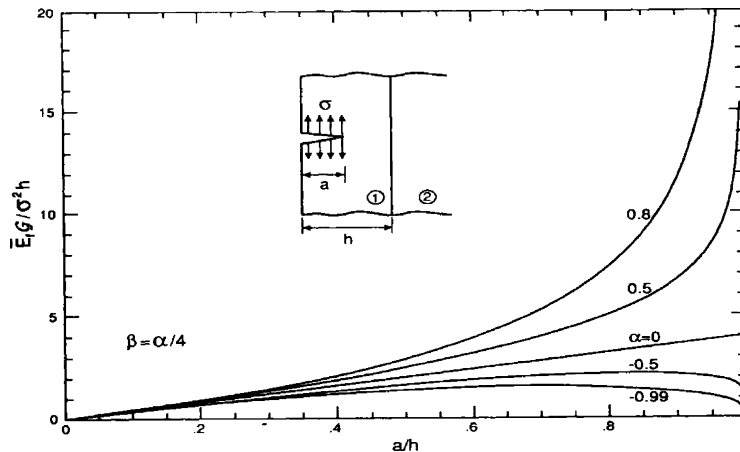


Figure 21 Driving force available for an edge crack at various depths a/h (source Beuth, 1992).

factor $K/\sigma\sqrt{h}$ depends only on the relative crack depth a/h and the Dundurs' parameters α, β . If the value of a/h is small enough, the stress intensity factor will approach to that of

an edge crack in a semi-infinite space, i.e., $K \rightarrow 1.12\sigma\sqrt{\pi a}$. For another limiting case, $a/h = 1$, the crack is perpendicular to and terminates at the interface, the stresses near

such a crack tip behave like $\sigma_{ij} \approx \tilde{K}r^{-s}\tilde{\sigma}_{ij}(\theta)$, where $\tilde{\sigma}_{ij}(\theta)$ is the angular stress distribution function. \tilde{K} is a generalized stress intensity factor, which has the dimension: [stress][length]^s (Zak and Williams, 1963; Cook and Erdogan, 1972; Wang and Ståhle, 1998b). The singular exponent $s(0 < s < 1)$ is the smallest real root of the following eigen equation:

$$\cos(s\pi) - 2\frac{\alpha - \beta}{1 - \beta}(1 - s)^2 + \frac{\alpha - \beta^2}{1 - \beta^2} = 0 \quad (19)$$

The numerical results of s are depicted in Figure 22.

As $a/h \rightarrow 1$, but with the crack tip still within the film, the stress intensity factor can be expressed as $K/\sigma\sqrt{h} = 1.12\sqrt{\pi}(a - h)^{1/2}(1 - a/h)^{1/2-s}(1 + \lambda a/h)$ (see Beuth, 1992). The parameter λ only depends on the Dundurs' parameters and is plotted in Figure 22.

The energy release rate G/G_0 is shown in Figure 21, where $G_0 = \sigma^2 h(1 - \nu_f^2)/E_f$. The critical condition for crack initiation can be expressed as $G \geq \Gamma_f$. From Figure 21, one can see that the crack growth will be unstable for the case of $\alpha \geq 0$. Meanwhile the crack will be blocked by the interface after crack initiation for the case of $\alpha < 0$. This means that if the substrate is stiffer than the film, the interface acts as an obstacle to block crack growth.

8.03.3.2.3 Crack channeling

If the film is brittle, a crack may channel through it as shown in Figure 23. The problem is three-dimensional (3D). An accurate solution is rather complex. After the crack channel length exceeds the film thickness by several times, the channel will approach a steady state

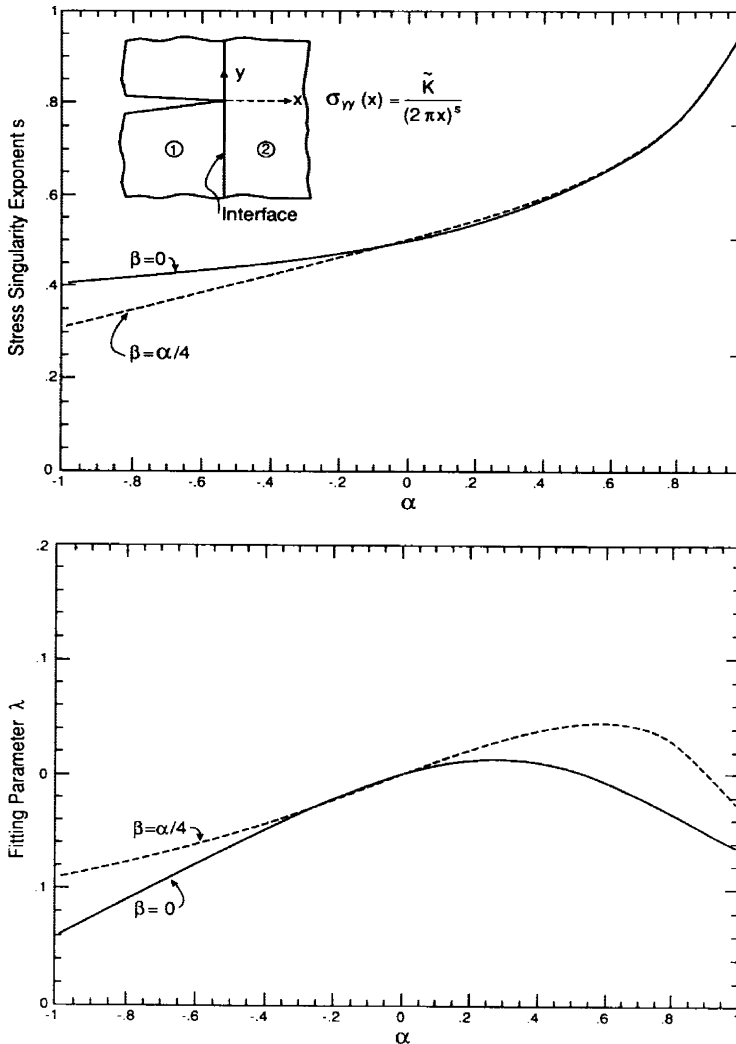


Figure 22 (a) Zak–Williams singularity and (b) a curve fitting parameter (reproduced by permission of Academic Press from “Advances in Applied Mechanics,” vol. 29, pp. 63–191).

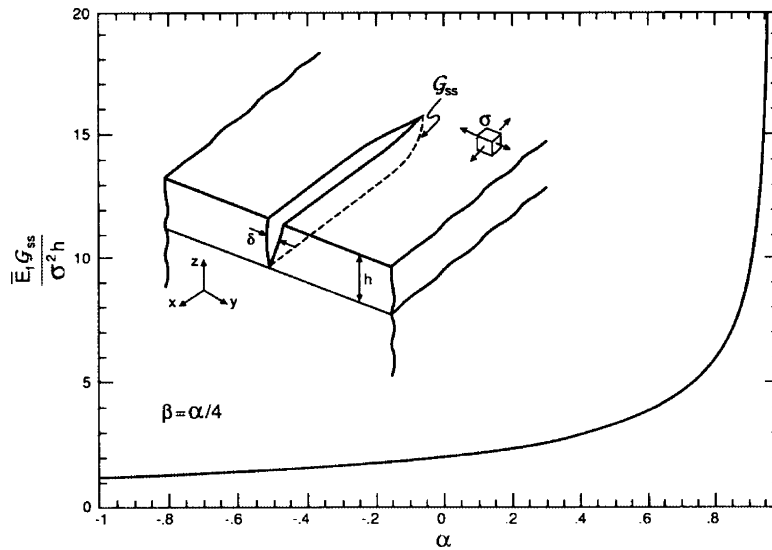


Figure 23 The insert shows a crack channeling across the film, driven by the tensile stress in the film. The available energy at the channel front is plotted for various elastic mismatch (after Ye *et al.*, 1992; reproduced by permission of Academic Press from “Advances in Applied Mechanics,” vol. 29, pp. 63–191).

and the cross-section profile in the wake attains the shape of a plane strain through crack. In the steady state, the energy release rate at the channel crack front can be evaluated by subtracting the strain energy stored in a unit length slice far behind of the front from that far ahead of the front. The calculation is quite simple and does not require the knowledge of the real front shape. Motivated by this consideration, Hutchinson and Suo (1992) proposed an alternative formula

$$G_{ss} = \frac{\sigma}{2h} \int_0^h \delta(z) dz$$

where $\delta(z)$ is the displacement profile for a plane strain crack. The second formula proposed by them is

$$G_{ss} = \frac{1}{h} \int_0^h G(a) da$$

where $G(a)$ is the energy release rate of a plane strain crack of depth a in Figure 21. This means that the energy release rate G_{ss} is the average of the energy release rates for plane strain cracks at various depths. The energy release rate G_{ss} with dissimilar elastic modulus was given by Beuth (1992). A typical result with $\beta = \alpha/4$ is shown in Figure 23. If G_{ss} is larger than Γ_f , a channel network is expected. For the case of $\alpha = \beta = 0$ (the film and substrate are homogeneous elastic media), the nondimensional driving force is $Z = 1.976$, as listed in Figure 20.

8.03.3.2.4 Substrate cracking

The driving force for a plane strain crack penetrating into a substrate was analyzed by Ye *et al.* (1992) and the results are plotted in Figure 24. Obviously the driving force decreases as the crack depth increases for the case of $\alpha > -0.5$. It implies that the crack will arrest at a certain depth.

8.03.3.3 Debonding and Sliding in Brittle Matrix Composites

Ceramic matrix reinforced by continuous fiber could create a composite that is significantly stronger and tougher than the ceramic matrix. The property of the fiber-matrix plays an important role. Much observation has shown that a relatively weak interface can prevent matrix cracks from breaking the fibers in their propagation paths due to interface debonding and sliding. These fibers bridge the crack and impede matrix crack from further propagation.

The effect of bridging fibers on matrix propagation has been investigated by several authors. Aveston *et al.* (1971) proposed a model to estimate the applied tensile stress at which the matrix crack could be nucleated with the fiber remaining completely intact. The effect of the interface sliding on the applied fracture stress was also studied by them. The ACK model of Aveston *et al.* (1971) was extended by Budiansky *et al.* (1986). Their BHE model utilizes a shear lag analysis of a single cylindrical fiber surrounded by an annular crack. A critical review on the

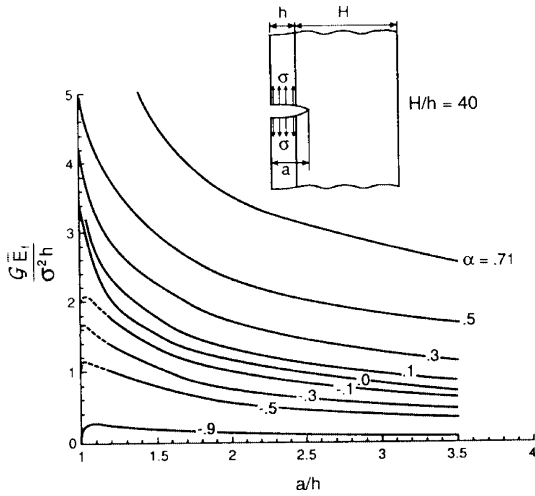


Figure 24 Energy release rate for a plane strain with the tip in the substrate (source Ye *et al.*, 1992).

mechanical behavior of ceramic composites reinforced by continuous fiber was given by Evans and Marshall (1989). Figure 25 shows a schematic of a long fiber unidirectionally reinforced composite that contains a bridged crack and is subjected to remote tension parallel to the fiber axis. The basic features are depicted in Figure 26. Debonding and sliding at the fiber/matrix interface must occur to allow crack bridging by the fibers. The initial debonding of the interface at the crack front results in sliding along the interface. When this situation appears, the sliding resistance τ of the debonding interface has an important role for governing the rate of load transition from the fiber to the matrix. A small sliding resistance along the debonding interface promotes high “toughness.” If the residual stress in the interface is compressive, the debonding length of the interface is small. But the debonding can be extensive when the residual stress is tensile. A more important fact is that the debonding could be further developed in the crack wake. The extent of debonding in crack wake is still governed mainly by the residual field.

He and Evans (1991) pointed out that the fiber debonding is preferred to occur if the fracture resistance of the interface, Γ_i , is sufficiently small compared with that of the fiber, Γ_f , e.g., $\Gamma_i \leq 0.25\Gamma_f$. The experimental observations of crack interaction with fibers and whiskers seem to support this judgment (Bischoff *et al.*, 1989; Thouless *et al.*, 1989a). The mechanical properties of the interfaces, the strength of the fibers, and the residual stresses in the composite are three key factors to control the axial tensile properties of the composite. Qualitatively, the “tough” response is favored in composites with “weak” inter-

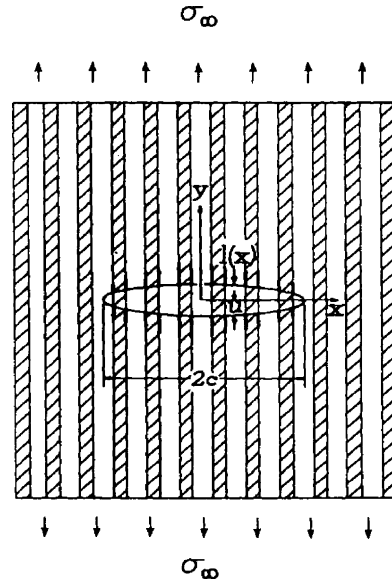


Figure 25 Schematic of a crack bridged by fibers and subjected to far-field loading (source Danchai-vijit and Shetty, 1993).

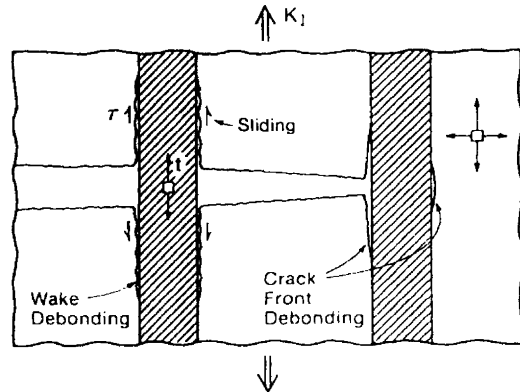


Figure 26 A schematic illustrating the initial debonding of fibers at the crack front and fiber debonding in the crack wake (source Evans and Marshall, 1989).

faces, high-strength fibers, and tensile residual stresses normal to the fiber/matrix interface. Otherwise a catastrophic failure response could occur. Different typical responses are sketched in Figure 27.

For a “tough” ceramic composite, the first crack in the matrix could nucleate from a pre-existing flaw, breaking only a small fraction of fibers. Further loading increases the nonlinear behavior of the stress–strain curve of the composite due to interface debonding and frictional interactions between the fibers and the matrix. This phenomenon is called the fiber bridging. The tail of the stress–strain curve corresponds to pullout of broken fibers. The

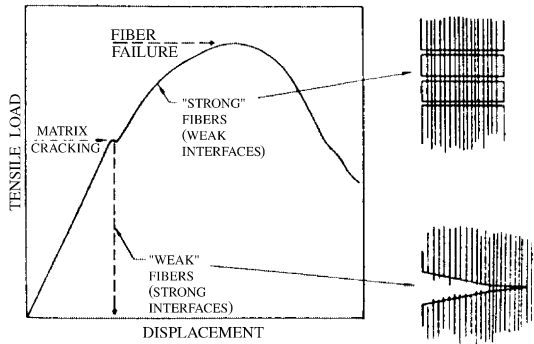


Figure 27 A tensile stress-strain curve for a “tough” ceramic composite (source Evans and Marshall, 1989).

ultimate strength of the composite is largely determined by the strength of the fiber bundle. This type of “tough” response is quite common in many composites.

The stretching of bridging fibers between two crack surfaces can be characterized by a relation of the average bridging stress, p , versus a local opening displacement, u , as shown in Figure 28. This formula depends strongly on the bridging mechanism and mechanical properties such as interface debonding, frictional sliding, and elastic properties of the fibers. The maximum value σ_{fc} represents the “strength” of the fiber.

If the interface between fiber/matrix is perfectly bonded, no debonding occurs when a matrix crack terminates at the interface, the $p(u)$ curve is linear up to failure. In the other extreme case, the fibers are completely debonded from the matrix, but frictional forces resist pullout, and the bridging stress increases monotonically until the fibers break, then the bridging stress decreases and the broken fibers are pulled out of the matrix. The bridging stresses in the fibers within the crack wake are taken as crack closure tractions, which reduce the stress intensity factor at the crack tip. Using a standard Green’s function one can calculate shielding stress intensity factors. An alternative approach is to use the J -integral to estimate the effect of the bridging traction on the energy release rate. A bridging zone develops behind the advancing crack front and results in the increase of the applied stress intensity factor. The crack growth is depicted by a resistance curve.

Budiansky *et al.* (1986) and Rose (1987) proposed a simple analytical solution of the steady state toughness increment $\Delta G = 2 \int_0^{u_0} p(u) du$, where u_0 is the crack opening displacement at the end of the bridging zone.

The critical stress for the growth of matrix cracks bridged by continuous fibers have been

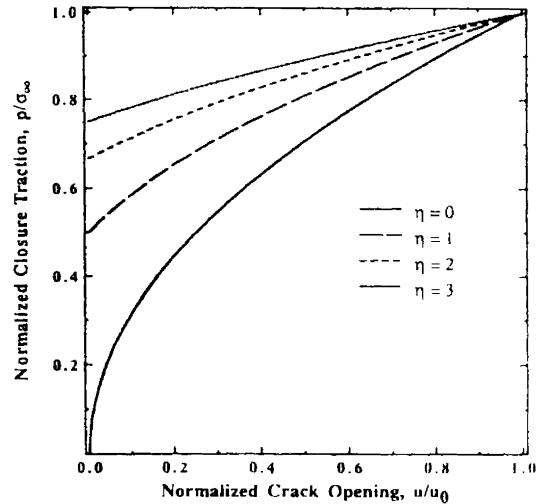


Figure 28 Normalized crack closure traction, p/σ_∞ , as a function of normalized crack opening displacement, u/u_0 (source Danchaivijit and Shetty, 1993).

investigated by Marshall *et al.* (1985), Wells and Beaumont (1985), Stang and Shah (1986), MacCartney (1987), Gao *et al.* (1988), Majumdar *et al.* (1989), Thouless *et al.* (1989b), Danchaivijit and Shetty (1993), Curtin (1993), Xia *et al.* (1994), and Meda and Steif (1994), among others. Marshall and Cox (1987) considered the effect of the fiber strength, fiber strength statistical distribution, and residual stress.

The calculations of critical stress essentially include three steps:

- (i) Establishing a formula between the closure traction applied by the bridging fiber and the local crack opening displacement.
- (ii) Developing an integral equation to determine the crack opening displacement by the entire distribution of crack surface tractions and solving this integral equation in a self-consistent scheme to ensure the formula of the bridging traction versus crack opening displacement is satisfied.
- (iii) Using the self-consistent fiber tractions to calculate the effective stress intensity factor and the critical stress.

Danchaivijit and Shetty (1993) obtained a simple analytical formula of the bridging traction versus crack opening displacement. According to this formula, the normalized bridging stress as a function of the normalized crack opening displacement is plotted in Figure 28, where the parameters $\eta = E_f V_f / E_m V_m$ and $u_0 = \sigma_\infty^2 R / 4(1 + \eta) E_f V_f^2 \tau$, E_f , E_m are the Young moduli of the fiber and matrix, respectively; V_f , V_m are the volume fractions of the fiber and matrix, respectively; R is the radius of the fiber; and τ is the sliding friction

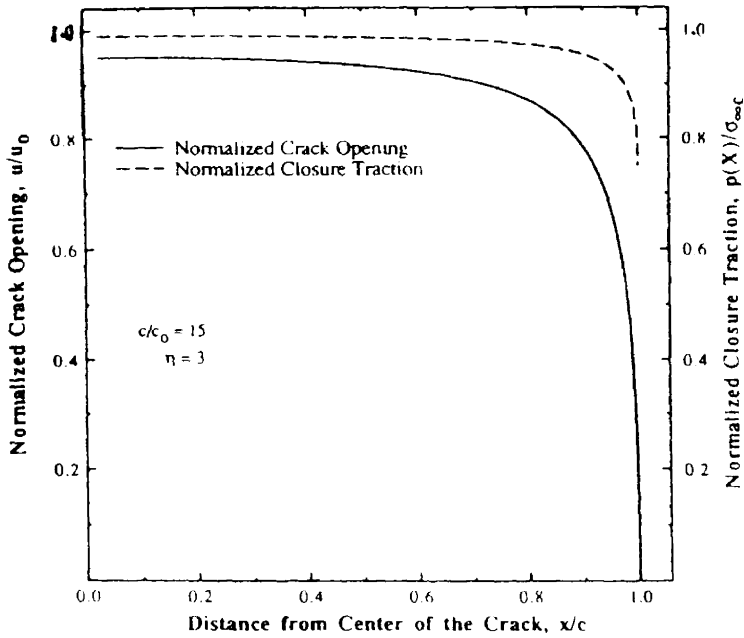


Figure 29 Crack surface traction and crack opening displacement for a fiber-bridged crack in the steady-state regime (source Danchaivijit and Shetty, 1993).

stress over the debonding region which is assumed to be constant. The crack surface traction and the crack opening displacement in the steady state are shown in Figure 29.

The normalized critical stress for the growth of a matrix crack as a function of normalized crack length is depicted in Figure 30 for a silicon/carbide/lithium aluminosilicate composite. The properties of the fiber, matrix, composite, and interface were taken from the data compiled by Marshall *et al.* (1985). The solid line represents the numerical results for $\eta = 2.35$, the value applicable to this composite, the long dashed line is the result using the approximation, $E' = E_{11} = E_c$, where E_c is the Young modulus of the composite, $c_0 = \pi(K_{cm}/\alpha)^{2/3} V_m^2 (1 + \eta)$, V_m is the volume fraction of the matrix, K_{cm} is the fracture toughness of the matrix, and c is the crack length. The definition of E' can be found in the paper by Danchaivijit and Shetty (1993). The experimental results given by Marshall *et al.* (1985) and the prediction by the ACK theory are also plotted in Figure 30.

8.03.3.4 Cracks in Multilayers

Attention here is focused on the cracking of a thin brittle adhesive layer joining two identical thick bulk solids. The cracking morphologies are sketched in Figure 31. The adhesive layer thickness is assumed to be very small compared with the in-plane dimension of the system. The applied load is characterized

by stress intensity factors K_I^∞ and K_{II}^∞ , which are determined from macroscopic analysis without considering the existence of the thin layer. The macroscopic energy release rate is

$$G^\infty = \frac{1 - \nu^2}{E} (K_I^{\infty 2} + K_{II}^{\infty 2})$$

where E and ν are the Young modulus and the Poisson ratio of the two bulk materials, respectively. The macroscopic toughness $\bar{\Gamma}(\psi^\infty)$ of the system is determined by test, where $\psi^\infty = \tan^{-1}(K_{II}^\infty / K_I^\infty)$. A test series carried out using such sandwich specimen provides the macroscopic interface toughness $\bar{\Gamma}(\psi^\infty)$. In engineering applications, one can disregard the local crack morphology. The critical condition for interface crack growth can be expressed as $G_c^\infty = \bar{\Gamma}(\psi^\infty)$, where G_c^∞ is the critical macroscopic energy release rate.

8.03.3.4.1 A straight crack within the layer

According to the J -integral principle, the local energy release rate G is identical to G^∞ . The local energy release rate G is closely related to the local stress intensity factors,

$$G = \frac{1 - \nu_2^2}{E_2} (K_I^2 + K_{II}^2)$$

where E_2, ν_2 are the Young modulus and the Poisson ratio of the layer, respectively. The relation between the local stress intensity factors and the applied stress intensity factors

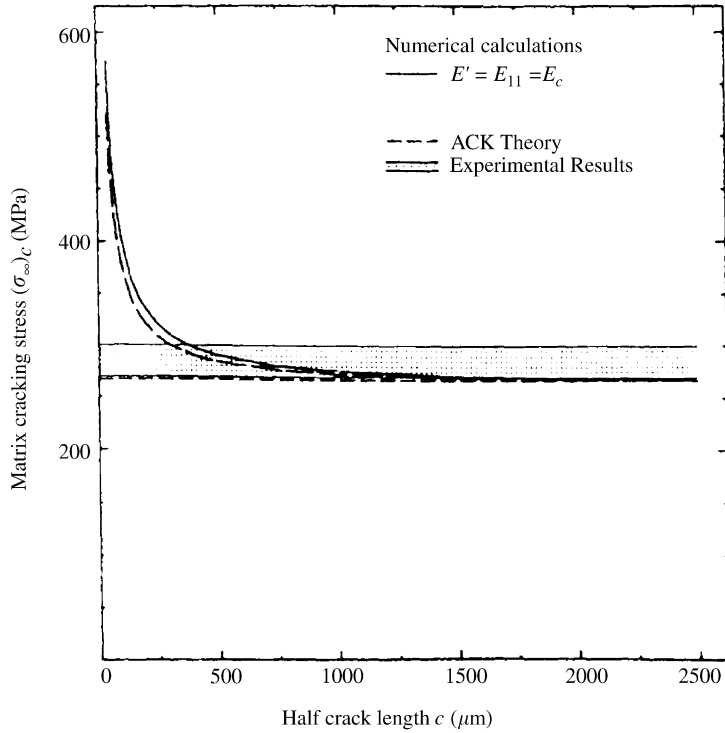


Figure 30 Comparison of the predictions of the numerical study with the matrix-cracking stress measurements on silicon carbide–lithium aluminosilicate composites (source Danchaivijit and Shetty, 1993).

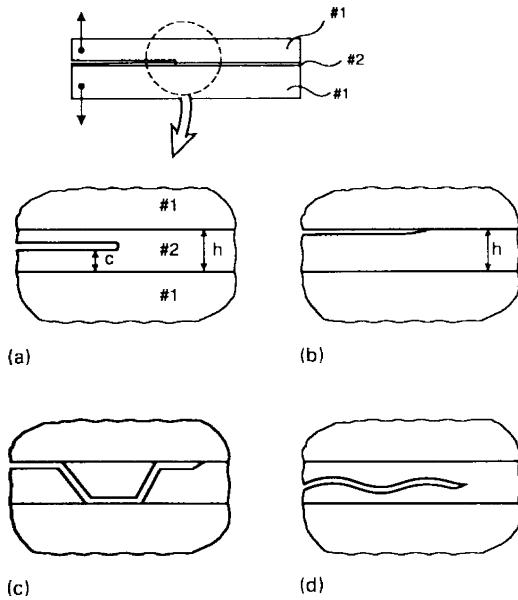


Figure 31 Modes of cracking in a thin brittle adhesive layer: (a) straight crack within layer (b) interface crack, (c) alternating crack, and (d) wavy crack (source Hutchinson and Suo, 1992).

takes the form

$$K = \left(\frac{1 - \alpha}{1 + \alpha}\right)^{1/2} (K_I^\infty + iK_{II}^\infty)e^{i\phi}$$

where ϕ is the shift in the phase angle between the local stress intensity factors and the applied stress intensity factors. The numerical results for ϕ were given by Fleck *et al.* (1991). If the applied stress intensity factor is pure mode I and the crack propagates along the centerline of the layer, Wang *et al.* (1978) showed that the local stress intensity factor K_I could be expressed as

$$K_I = \left(\frac{1 - \alpha}{1 + \alpha}\right)^{1/2} K_I^\infty$$

This result implies that a crack within a compliant layer is shielded. The shielding factor can be large when two stiff materials are jointed by a compliant adhesive. For example, when two ceramic bulk materials are jointed by a polymer adhesive.

8.03.3.4.2 Crack along the interface

The local energy release rate G still equals the global energy release rate G^∞ in this case. The local stress intensity factors are related to the global stress intensity factors according to the formula

$$K = h^{-ic} \left(\frac{1 - \alpha}{1 - \beta^2}\right)^{1/2} (K_I^\infty + iK_{II}^\infty)e^{i\omega}$$

where the shift angle $\omega(\omega = \psi - \psi^\infty)$ ranges between 5° and -15° and is plotted in Figure 32 (Suo and Hutchinson, 1989a).

8.03.3.4.3 Alternating cracking

A crack path switching back and forth between the upper and lower interfaces with a fairly regular interval is called the alternating-cracking mode. Chai (1987) has reported this mode in an aluminum/epoxy/aluminum sandwich specimen. The relatively high residual tensile stress σ_R in the layer was ~ 60 MPa, which was induced by a thermosetting epoxy. The system has a strong positive T -stress. A quantitative analysis of the alternating cracking mode was given by Akisanya and Fleck (1992). The key feature is the variation in the mode mixity. The trends of the variation in the mode mixity ψ are plotted in Figure 33, where ψ is defined by

$$\psi = \tan^{-1} \left[\frac{\text{Im}(Kl^{ie})}{\text{Re}(Kl^{ie})} \right]$$

with $l = h$. When $\sigma_R \sqrt{h}/K_I^\infty$ is of the order of unity, the interface starts with a large negative value of ψ , then decreases to the value $\psi = \omega$ as the crack length increases. The large negative value K_{II} forces the crack to propagate along the interface since the crack cannot penetrate the aluminum due to relatively high tensile residual stress in the layer. When the magnitude of ψ is sufficiently low, the crack kinking down into the layer becomes possible for the aluminum/epoxy sandwich system. Akisanya and Fleck (1992) found that the kinking condition was met when $c/h \rightarrow 2$, which is consistent with the experimental observation of Chai (1987).

8.03.3.4.4 Tunneling cracks

Bi-axial residual stresses could be developed in the adhesive layer during the bonding process. For example, two parts of ceramics coated with glass are put together and heated above the melting temperature of the glass, and then cooled down to the room temperature. A residual stress is produced due to a thermal expansion mismatch. The residual stress is tensile in the glass, since the thermal expansion coefficient of the glass is larger than that of the ceramic part. The tensile residual stress causes cracks to tunnel through the adhesive glass. Figure 34 shows a crack nucleated from a flaw, tunneling through the adhesive layer. The crack tunneling is a complicated 3D problem. When the crack length is much longer than the adhesive layer thickness, a steady state is

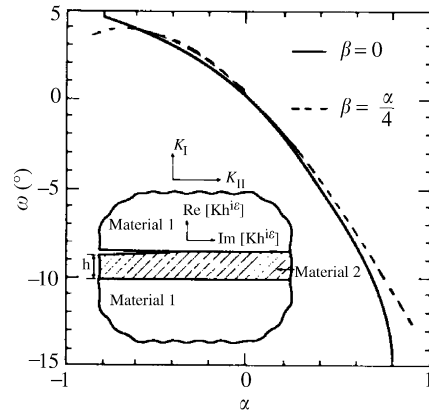


Figure 32 An interface crack in a sandwich. The phase shift ω is plotted as a function of elastic mismatch parameter (source Hutchinson and Suo, 1992).

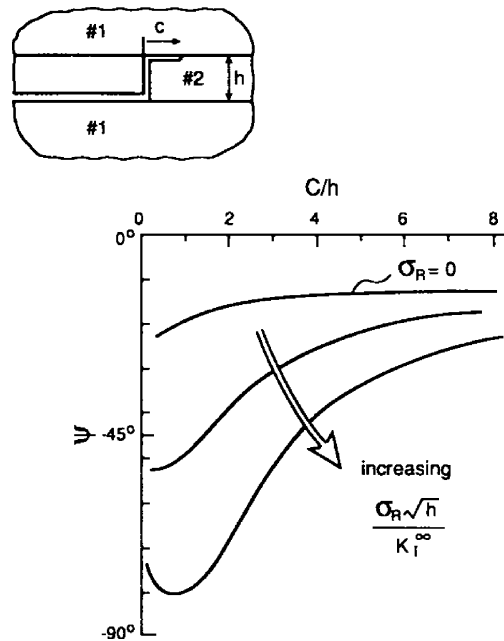


Figure 33 Sketch of trends of phase of loading at interface crack tip for various levels of residual tension σ_R in the layer. The remote loading is mode I (after Akisanya and Fleck, 1992; reproduced by permission of Academic Press from "Advances in Applied Mechanics," vol. 29, pp. 63–191).

reached. The tunneling crack front maintains its shape. The energy release rate per unit advance can be calculated by using a 2D elastic solution. The energy release rate hG_{ss} , per unit length of a tunneling crack is identical to the energy released by a plane strain crack growing across the layer. The energy release rate G_{ss} for a single tunneling crack in a finite thickness sandwich was given by Ho and Suo (1992). The nondimensional G_{ss} is a function of the elastic

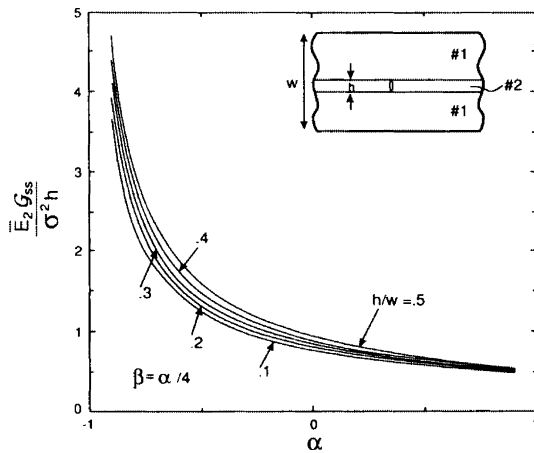


Figure 34 Steady-state energy release rate for isolated tunneling crack. The crack extends from interface to interface, and is propagating in the direction perpendicular to the cross-section shown (after Ho and Suo, 1992; reproduced by permission of Academic Press from “Advances in Applied Mechanics,” vol. 29, pp. 63–191).

mismatch parameters α and β , and the relative thickness h/w . Figure 34 shows typical results for different values of α (with $\beta = \alpha/4$) and various values of h/w . The nondimensional energy release rate seems to be very sensitive to the mismatch parameter α , on the other hand, it seems not to be sensitive to the relative thickness of h/w when $\alpha > 0.5$.

8.03.3.5 Crack Perpendicular to a Bimaterial Interface

A crack perpendicular to a bimaterial interface has attracted many investigators. Zak and Williams (1963) used the eigenfunction expansion method to analyze the stress singularity ahead of a crack tip, which is perpendicular to and terminated at the interface (see also Wang and Karihaloo, 1994, 1996). Their analysis revealed that the stress singularity is of the order r^{-s} , where s is the smallest real eigenvalue and dependent on the elastic moduli of the bimaterial. Cook and Erdogan (1972) used the Mellin transform method to derive the governing equation of a finite crack perpendicular to the interface and obtained the stress intensity factors. Erdogan and Biricikoglu (1973) solved the problem of two bounded half planes with a crack going through the interface. Bogy (1971) investigated the stress singularity of an infinite crack terminated at the interface with an arbitrary angle. Wang and Chen (1993) used photoelasticity to determine the stress distribution and the stress intensity factors of a crack perpendicular to the interface. They found that

the far field has significant effects on the stress distribution and stress intensity factors.

Lin and Mar (1976) presented a finite element analysis of the stress intensity factors for cracks perpendicular to a bimaterial interface. Ahmad (1991) used the finite element method to analyze a crack normal to the fiber-matrix interface in unidirectional fiber composites.

Meguid *et al.* (1995) proposed a novel finite element to analyze cracks perpendicular to bimaterial in finite elastic body. Chen (1994) used the body force method to determine the stress intensity factors for a crack normal to and terminated at a bimaterial interface. Stähle *et al.* (1995) investigated a crack growing towards a bimaterial interface. They carried out an experiment and a finite element simulation. Their results showed that the crack could deflect and follow a smooth curved path.

8.03.3.5.1 Crack perpendicular to a bimaterial interface

Consider the in-plane elasticity problem as shown in Figure 35. A finite crack is perpendicular to a bimaterial interface, which does not intersect with the interface. The elastic body is bonded by two materials and subjected to the prescribed traction p_i on the surface S_σ and to the prescribed displacements u_i on the surface S_u . The crack surfaces are assumed to be traction free. Both materials are isotropic and homogeneous. The material I occupies the upper half-plane S_1 and the material II occupies the lower half-plane S_2 . A Cartesian coordinate system oxy is attached to the interface. The x -axis is along the interface and the y -axis is normal to the interface and coincident with the crack elongation direction. The crack is within material II. Stress and displacement can be expressed by Equation (6). The complex potential for an edge dislocation at $z = s$ in an infinite homogeneous elastic solid can be expressed by Equation (7).

The crack can be considered as a continuous distribution of dislocations. A novel expansion method was proposed by Wang and Stähle (1998a) for solving the problem. The dislocation density was expressed as a series of Chebyshev polynomials of the first kind. The complex potential and the stress fields can be expanded as a power series of a new complex variable, which is a simple rational function of the complex variable z . Using the traction free condition on the crack surface, one can establish the governing equations for the unknown dislocation density functions b_x and

b_y . Based on the boundary collocation method, the governing equation was solved and the unknown coefficients were obtained. The complete solutions to the problem, including the T -stress ahead of the crack tip and the stress intensity factors were presented. The stress field characteristics were analyzed in detail in their paper. Without loss of generality, they studied the problem of $\sigma_y^\infty = 0$ and $\tau_{xy}^\infty = 0$. The nonvanishing remote stresses are $(\sigma_x^\infty)_II = \sigma$ and $(\sigma_x^\infty)_I$, which satisfies Equation (4).

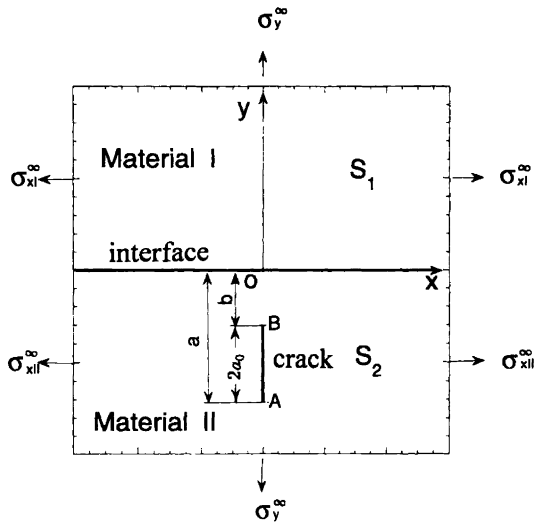


Figure 35 A finite crack perpendicular to a bimaterial interface.

(i) Stress intensity factors

The calculated stress intensity factors for a half plane are given in Table 1. The results by Cook and Erdogan (1972) are also listed in this table for comparison. The two results agree with each other. The calculated stress intensity factors for the material pairs aluminum–epoxy in the plane strain are shown in Table 2. The elastic constants are $\mu_1/\mu_2 = 23.08$, $\nu_1 = 0.3$, and $\nu_2 = 0.35$. For comparison, the results by Cook and Erdogan (1972) are also listed in this table. The two results are in complete agreement.

The stress intensity factor at the crack tip B versus the geometry parameter $\rho = b/a_0$ is plotted in Figure 36 for the material pair of aluminum–epoxy. The nondimensional stress intensity factor is $\bar{K}_I(B) = K_I(B)/\sigma\sqrt{\pi a_0}$. When the crack in the weak epoxy approaches the interface, the stress intensity factor at crack tip B will approach zero due to the strong blocking effect from the stiff material aluminum. It is worth noting that the nondimensional stress intensity factor $\bar{K}_I(B)$ at the crack tip B varies approximately according to a power law relation. A simple fit was proposed by Wang and Stähle (1998a) as $\bar{K}_I(B) = q\rho^\gamma$, where q and γ are given in their paper. The curves given by this equation (Equation (33) in their paper) are also listed in Figure 36. It is clear that this equation gives very good prediction when the parameter $\rho < 0.1$.

Figure 37 depicts the stress intensity factor at the crack tip B versus the geometry parameter

Table 1 Stress intensity factors for a half plane.

b/a_0	$K_I(A)/\sigma\sqrt{\pi a_0}$ Source ^a	$K_I(A)/\sigma\sqrt{\pi a_0}$ Source ^b	$K_I(A)/\sigma\sqrt{\pi a_0}$ Source ^a	$K_I(B)/\sigma\sqrt{\pi a_0}$ Source ^b
0.10	1.211	1.211	1.759	1.759
0.15	1.183	1.183	1.575	1.575
0.20	1.163	1.163	1.464	1.464
0.50	1.097	1.097	1.204	1.204
1.00	1.054	1.054	1.091	1.091
4.00	1.009	1.009	1.011	1.011
9.00	1.002	1.002	1.003	1.003

Source: ^a Wang and Stähle (1998a). ^b Cook and Erdogan (1972).

Table 2 Stress intensity factors for an aluminum–epoxy bimaterial.

b/a_0	$K_I(A)/\sigma\sqrt{\pi a_0}$ Source ^a	$K_I(A)/\sigma\sqrt{\pi a_0}$ Source ^b	$K_I(A)/\sigma\sqrt{\pi a_0}$ Source ^b	$K_I(B)/\sigma\sqrt{\pi a_0}$ Source ^a
0.10	0.8985	0.8985	0.6674	0.6674
0.15	0.9051	0.9051	0.7179	0.7179
0.25	0.9165	0.9165	0.7838	0.7838
1.00	0.9616	0.9616	0.9249	0.9249
4.00	0.9929	0.9929	0.9912	0.9912
9.00	0.9981	0.9981	0.9979	0.9979

Source: ^a Wang and Stähle (1998a). ^b Cook and Erdogan (1972).

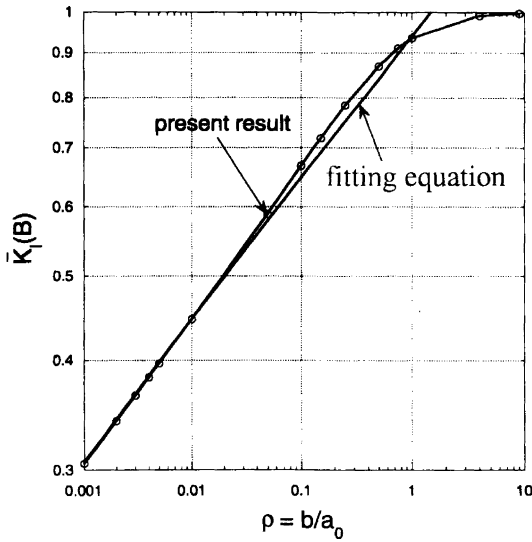


Figure 36 Nondimensional stress intensity factor $\bar{K}_I(B) = K_I(B)/\sigma\sqrt{\pi a_0}$ versus the geometry parameter ρ for material pair aluminum-epoxy.

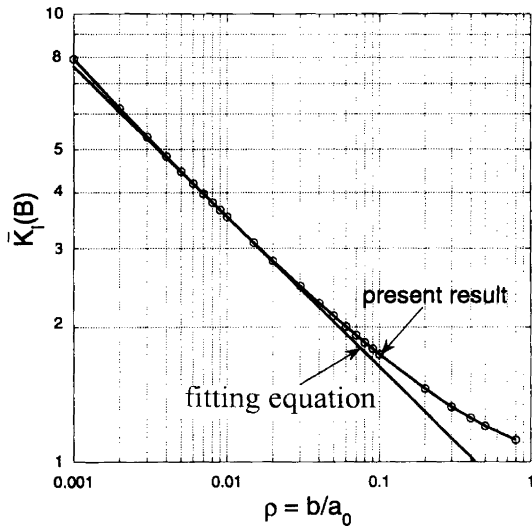


Figure 37 The relationship between the nondimensional stress intensity factor $\bar{K}_I(B) = K_I(B)/\sigma\sqrt{\pi a_0}$ and the geometry parameter ρ for material pair epoxy-boron.

$\rho = b/a_0$ for material pairs epoxy-boron. The elastic constants are $\mu_1/\mu_2 = 0.007223$, $\nu_1 = 0.35$, and $\nu_2 = 0.3$. The crack is now within the stiff material of boron. The stress intensity at crack tip B increases rapidly when the geometry parameter ρ approaches zero. The empirical equation gives very good prediction when the parameter $\rho < 0.1$.

(ii) Stress distribution ahead of the crack tip B

Figures 38 and 39 show the stress distribution ahead of the crack tip B for the material pairs of aluminum-epoxy in the case $b/a_0 =$

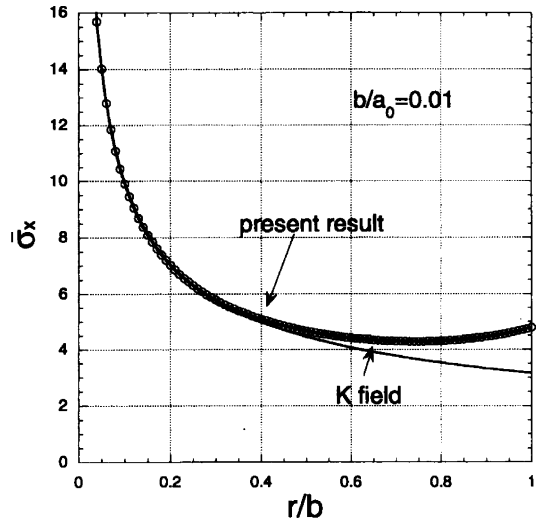


Figure 38 Normal stress σ_x distribution ahead of the crack tip B for material pair aluminum-epoxy in the case of $b/a_0 = 0.01$. Here r is the distance from the crack tip B and $\bar{\sigma}_x = \sigma_x/\sigma$.

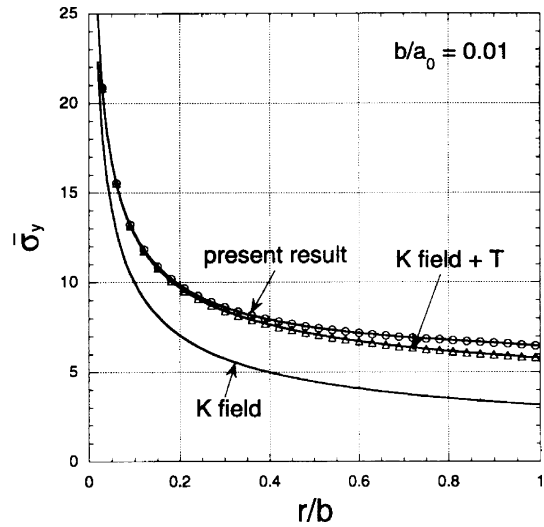


Figure 39 Comparison of the normal stress σ_y ahead of the crack tip B with the K -field and the K -field plus T stress for material pair aluminum-epoxy in the case of $b/a_0 = 0.01$. Here r is the distance from the crack tip B and $\bar{\sigma}_y = \sigma_y/\sigma$.

0.01. The crack is within the weaker material. In these figures, the ordinates are the non-dimensional stresses $\bar{\sigma}_x = \sigma_x/\sigma$ and $\bar{\sigma}_y = \sigma_y/\sigma$, respectively. It is clear that the normal stress σ_x is dominated by the K -field in the region of $0 < r/b < 0.5$, whereas the normal stress σ_y is characterized by the K -field plus T -stress in the region of $0 < r/b < 0.4$.

Figure 40 shows the normal stress σ_y ahead of the crack tip B for the material pair epoxy-boron in the case $b/a_0 = 0.1$. Now the crack is within the stiffer material. The K -field is remarkably different from the accurate result

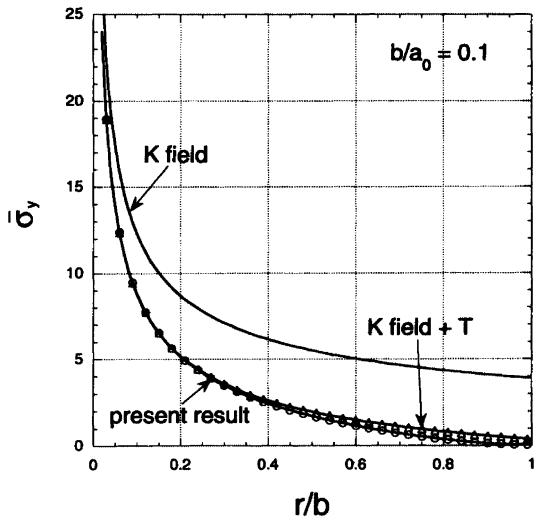


Figure 40 Comparisons of the normal stress σ_y ahead of the crack tip B with the K -field and the K -field plus T -stress for material pair epoxy–boron in the case of $b/a_0 = 0.1$.

for the normal stress σ_y . The normal stress σ_y is essentially characterized by the K -field plus T -stress in the region of $0 < r/b < 0.4$. It means that the T -stress effect is very important for the material pair aluminum–epoxy.

8.03.3.5.2 Crack perpendicular to and terminating at a bimaterial interface

Consider the plane elastic problem as shown in Figure 41. A finite crack is perpendicular to and terminating at a bimaterial interface. A basic equation for a finite crack perpendicular to and terminating at a bimaterial interface was formulated by Wang and Ståhle (1998b). The dislocation density was expressed as a series of Chebyshev polynomials of the first kind plus a special term, which had a desired stress singularity at the crack tip. Using a boundary collocation method, the governing equation was solved and the unknown coefficients were obtained. The complete solution to the problem was obtained.

(i) Calculation results

The calculation was carried out for different material pairs. The convergence of the series was rather rapid. The infinite series of the Chebyshev polynomials of the first kind can be approximated with a sufficient degree of accuracy by a corresponding truncated series, in which the maximum value of m is the number M . A typical example for the material pair of aluminum–epoxy was tested in the case

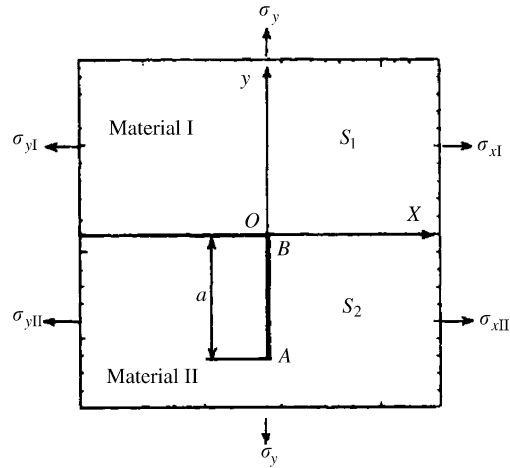


Figure 41 A finite crack perpendicular to and terminating at a bimaterial interface.

of plane strain. Values for M of 150, 180, and 210 gave the same results of stress intensity factors at the crack tips A and B with four digits of accuracy and the coefficients α_m of the series of the Chebyshev polynomials approaches zero rapidly as m increases. For example, $\alpha_1 = 0.2487$, $\alpha_{10} = -0.1421 \times 10^{-3}$, $\alpha_{100} = 0.4015 \times 10^{-6}$, $\alpha_{180} = -0.2342 \times 10^{-8}$. All results given in their paper were calculated with $M = 180$.

(ii) Stress intensity factors

The calculated stress intensity factors for different material pairs in the case of plane stress are shown in Tables 3 and 4.

Here the parameter λ_0 is the smallest eigenvalue of Equation (19). The results by Wang and Ståhle (1998b) agree well with the results by Meguid *et al.* (1995) and Chen (1994).

(iii) Stress distribution ahead of the crack tip B

The stress fields ahead of the crack tip can be expressed as

$$\sigma_{ij} = \frac{Q_1}{(2\pi r)^{\lambda_0}} f_{ij}(\theta) + T_{ij} \quad (20)$$

where Q_1 is the generalized mode I stress intensity factor at the crack tip B, T_{ij} are the T -stresses, which are characterized by the second term of the eigenfunction and play an important role in the analysis of fracture process. The first term of the right side of Equation (20) is known as the Q -field.

Figures 42 and 43 show the stress distributions ahead of the crack tip B for the material pair of epoxy–boron in the case of plane stress.

Table 3 Stress intensity factors $\bar{Q}_I(B) = \sqrt{2}Q_I(B)/\sigma(2\pi a_0)^{1/2}$.

μ_1/μ_2	ν_1	ν_2	Source ^a	Source ^b	Source ^c	Source ^d	Source ^e
0.00722	0.35	0.30	0.0192	0.018	0.0192	0.0196	0.079
0.0433	0.35	0.30	0.0955	0.094	0.095	0.095	0.074
23.08	0.35	0.30	4.232	4.240	4.231	4.241	4.176
138.46	0.35	0.30	5.002	5.004	5.001	4.978	4.922

Source: ^a Wang and Stähle (1998b). ^b Meguid *et al.* (1995). ^c Chen (1994). ^d Lin and Mar (1976). ^e Cook and Erdogan (1972).

Table 4 Stress intensity factors $\bar{K}_I(A) = K_I(A)/\sigma(2\pi a_0)^{1/2}$.

μ_1/μ_2	ν_1	ν_2	Source ^a	Source ^b	Source ^c	Source ^d
0.00722	0.35	0.30	1.474	1.474	1.529	1.509
0.0433	0.35	0.30	1.340	1.340	1.371	1.353
23.08	0.35	0.30	0.879	0.879	0.855	0.879
138.46	0.35	0.30	0.870	0.870	0.833	0.871

Source: ^a Wang and Stähle (1998b). ^b Chen (1994). ^c Lin and Mar (1976). ^d Cook and Erdogan (1972).

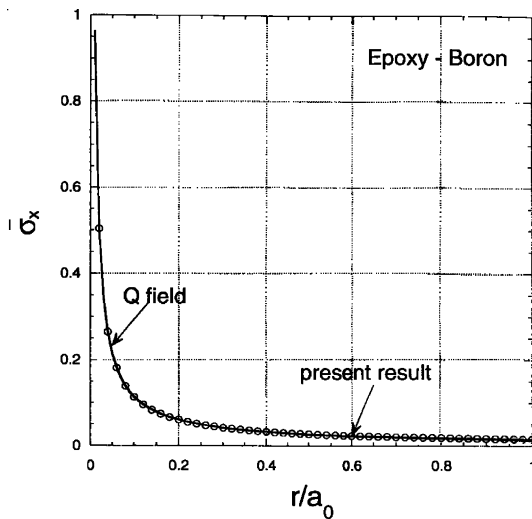


Figure 42 Normal stress σ_x distribution ahead of the crack tip B for material pair epoxy–boron in the case of plane stress. Here r is the distance from the crack tip B and $\bar{\sigma}_x = \sigma_x/\sigma$.

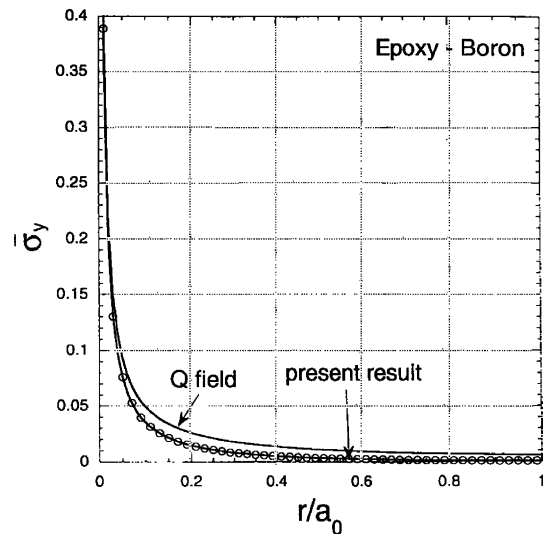


Figure 43 Normal stress σ_y distribution ahead of the crack tip B for material pair epoxy–boron in the case of plane stress and $\bar{\sigma}_y = \sigma_y/\sigma$.

The material constants are $\mu_1/\mu_2 = 0.00722$, $\nu_1 = 0.35$, and $\nu_2 = 0.3$. It is clear that the normal stress σ_x is dominated by the Q -field in the region of $0 < r/a_0 < 1$, whereas the normal stress σ_y is characterized by the Q -field in the region of $0 < r/a_0 < 0.05$.

The trend is different when the crack is within the weaker material, as shown in Figure 44 for the case of plane stress. Figure 44 shows the comparison between the normal stress σ_x , the Q -field, and the Q -field plus T_x stress for the material pair of boron–epoxy. The material constants are $\mu_1/\mu_2 = 138.46$, $\nu_1 = 0.3$, and $\nu_2 = 0.35$. The Q -field plus T_x stress gives very good prediction for the normal stress σ_x in the region of $0 < r/a_0 < 1$. But the Q -field is

remarkably different from the normal stress σ_x . It clearly shows that the T_x stress has a tremendous contribution to the normal stress. The Q -field plus the T_y stress also agrees very well with the normal stress σ_y in the region $0 < r/a_0 < 0.4$.

The situation for material pairs with slight elastic constant mismatch is similar. The normal stresses are dominated by Q -field plus T -stress. But the size of the dominated zone becomes small.

8.03.4 INTERFACE FRACTURE TEST

Experiments show that interfacial fracture toughness depends strongly on the mode

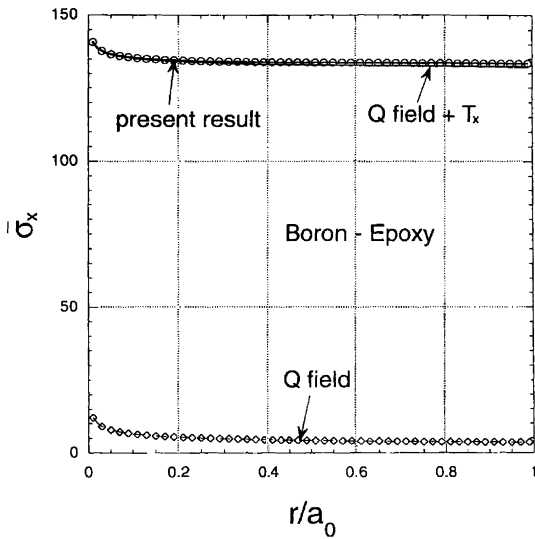


Figure 44 Normal stress σ_x distribution ahead of the crack tip B for material pair boron–epoxy in the case of plane stress.

mixity. Cao and Evans (1989), and Liechti and Chai (1991, 1992) studied the interfacial toughness of epoxy/glass system. Wang and Suo (1990) carried out interfacial fracture tests on an epoxy layer on metal and plexiglass substrates. O’Dowd *et al.* (1992) investigated the fracture toughness of alumina–niobium interfaces. All of these tests reveal a common feature: the interfacial fracture toughness increases rapidly as the phase angle becomes large. A variety of test methods have been proposed by Charalambides *et al.* (1989), Evans *et al.* (1990), Ruhle *et al.* (1990), and O’Dowd *et al.* (1992) among others. Delamination resistance of laminated composites can be enhanced by a variety of bridging mechanisms. The delamination resistance is nonunique, which indicates that the delamination resistance curve should be measured over the phase angle range of practical significance.

8.03.4.1 Delamination Specimens and R-curves

Beam-type fracture specimens are most extensively used for unidirectional composites, adhesive joints, and other laminated materials. Typical delamination beams were analyzed by Suo (1990b) and Bao *et al.* (1992). Liechti and Chai (1991, 1992) developed a bimaterial interfacial fracture specimen, which is capable of providing the interfacial fracture toughness over essentially the full range of mode mixity. The specimen used by them was the edge-cracked bimaterial strip made of glass and epoxy. The initial crack was introduced by

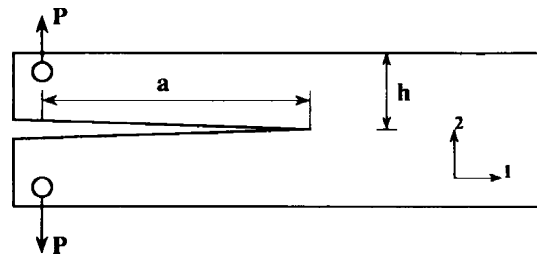


Figure 45 A double cantilever beam (DCB).

inserting a razor at the interface and wedging it open to a length $a_0 \approx 6h$. The specimen was loaded using a special biaxial loading device. The prescribed in-plane displacements were imposed along the clamped boundaries, $x_1 = \pm h$. The in-plane length is long compared with the thickness h of each layer. The solution to the problem of an infinite long strip with a semi-infinite interfacial crack was used by Liechti and Chai to obtain the energy release rate and the stress intensity factors.

For the plane strain case, the explicit solution for stress intensity factors can be found in the paper by Suo and Hutchinson (1990).

A double cantilever beam made of a unidirectional composite with fiber along the beam axis is plotted in Figure 45. The composite is treated as a homogeneous orthotropic material. Mesoscale features such as interface and fiber/matrix inhomogeneity are not explicitly taken into account. The specimen is pure mode I, the energy release rate is given by

$$G = f\left(\frac{a}{h}\right) \frac{(Pa)^2}{h^3 \bar{E}_L}$$

where P is the force per unit width, $2h$ the beam thickness, a the crack length, and \bar{E}_L the effective Young’s modulus in the fiber direction. The function $f(a/h)$ is related to the orthotropic parameters. A simple calibration formula for $f(a/h)$ was proposed by Bao *et al.* (1992). The formula was obtained using finite elements together with several analytic considerations.

Figure 46 depicts several edge-loaded specimens, which have a fixed mode mixity as the crack grows. In the unidirectional composites, the delamination cracks normally grow along the fiber direction. Figure 46(a) is a pure mode I specimen, while Figure 46(b) is a pure mode II specimen. Figures 46(c) and (d) are mixed mode specimens. As the crack length exceeds about two times the specimen thickness $2h$, both the energy release rate and the mode mixity become essentially independent of the crack length.

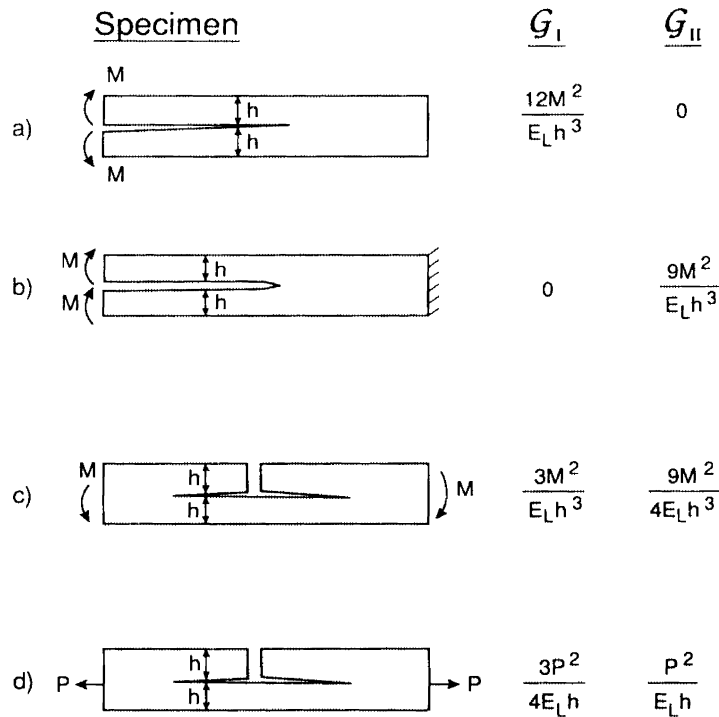


Figure 46 Several exact solutions: (a) a pure mode I specimen (double cantilever beam), (b) a pure mode II specimen (end-loaded split), (c) a mixed mode specimen (four-point bend), and (d) a mixed mode specimen (crack-lap shear) (reproduced by permission of Academic Press from "Advances in Applied Mechanics," vol. 29, pp. 63–191).

The calibrations for the energy release rates of different modes are also listed in Figure 46 (Hutchinson and Suo, 1992).

defined by

$$\psi = \tan^{-1} \left[\frac{\text{Im}(KI^{ic})}{\text{Re}(KI^{ic})} \right]$$

8.03.4.2 Interface Fracture Specimens

Gao *et al.* (1979), Suresh *et al.* (1990), and He *et al.* (1990) developed asymmetric three-point bend specimens and asymmetric four-point bend specimens for measuring the mixed-mode fracture toughness of homogeneous metallic materials. The corresponding calibration was given by Wang *et al.* (1977) and Suresh *et al.* (1990). Figure 47 shows the schematic diagrams of the asymmetric four-point bend specimen and the loading arrangement.

O'Dowd *et al.* (1992) adopted the asymmetric four-point bend specimen together with the symmetric four-point bend specimen. These geometries have been used by them to measure the interfacial fracture toughness of an alumina–niobium material system over the full range of mode mixity. Figure 48 provides a schematic diagram of the symmetric four-point bend specimen and the asymmetric four-point bend specimen. They carried out the specimen calibration. The stress intensity factors take the form $K = YT\sqrt{aa^{-ic}}e^{i\psi}$, where ψ is again

with $l = a$, and $T = (A - B)P/(A + B)W$ for asymmetric four-point bend specimen. The dimensionless functions Y and ψ are plotted in Figure 49.

For the symmetric four-point bend specimen, T is given by $T = P(3B/2W^2)$. The dimensionless functions Y and ψ are plotted in Figure 50. For the alumina–niobium pair with alumina designated as material I, the plane strain Dundurs' parameters are $\alpha = 0.527$ and $\beta = 0.063$ and consequently the oscillatory index is given by $\varepsilon = -0.02$.

8.03.4.3 Brazil-nut Specimen

A homogeneous Brazil nut is a disk of radius a , with a center crack of length $2l$, which was used by Atkinson *et al.* (1982) as well as Singh and Shetty (1989) for mixed mode fracture testing of brittle solids. The mode mixity is controlled by the compression angle, θ . It is pure mode I when $\theta = 0^\circ$, and pure mode II when $\theta \approx 25^\circ$. The stress intensity factors are given by $K_I = f_I Pa^{-1/2}$, $K_{II} = \pm f_{II} Pa^{-1/2}$, where the plus sign is for point A , and the

minus sign for point *B*. Atkinson *et al.* (1982) calibrated the nondimensional factors f_I, f_{II} . The energy release rate and phase angle $\psi = \tan^{-1}(K_{II}/K_I)$ at tips *A* and *B* are plotted in Figure 51 for homogeneous material. An interfacial fracture specimen can be made by sandwiching a thin interlayer of thickness h and a center crack of length $2l$ along one interface of the substrate/interlayer as shown in Figure 52. When the interlayer thickness h is

much smaller than the radius a and the crack length $2l$, the energy release rate can be evaluated by the Irwin relation in accordance with the J -integral principle. Since the perturbation in the far field due to the thin interlayer is negligible, the local stress intensity factors can still be calculated by the nondimensional factors f_I, f_{II} . The interfacial phase angle $\hat{\psi}$ is shifted from that for the homogeneous specimen, according to $\hat{\psi} = \tan^{-1}(K_{II}/K_I) + \omega + \varepsilon \ln(l/h)$, where ω is the shift due to substrate/interlayer mismatch of elastic constants, and the last term is the shift due to the oscillation index.

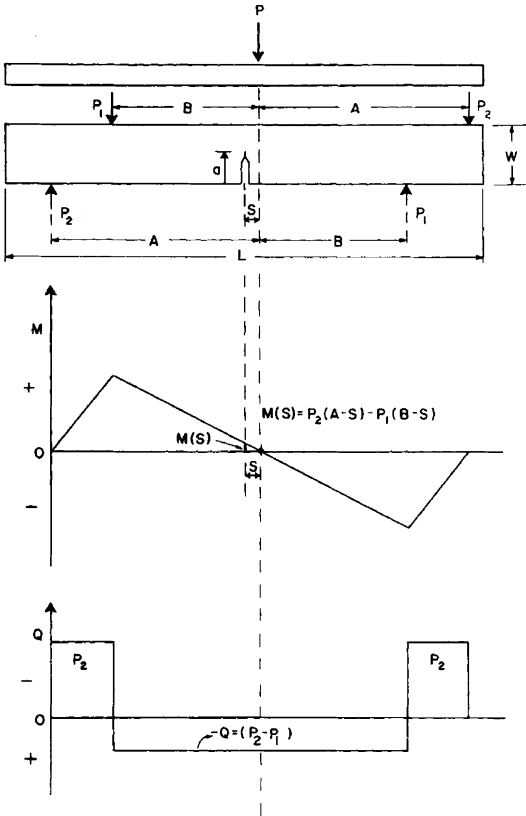


Figure 47 Schematic diagram of the asymmetric four-point bend specimen geometry and the loading arrangement, as well as the variation of the shear force, Q , and the bending moment, M , along the length of the specimen (source Suresh *et al.*, 1990).

8.03.4.4 Fracture Energy Data

The most complete sets of fracture energy data for an epoxy–glass interface were measured by Liechti and Chai (1991, 1992) and are shown in Figure 5. These data demonstrate the strong influence of mode mixity on Γ_i , which indicates the extensive plastic dissipation in the epoxy. The specially designed loading device of Liechti and Chai does not seem to be suitable for metal–ceramic bimaterial systems due to significant high elastic moduli.

The interfacial fracture toughness data for an alumina–niobium system with $\hat{l} = 100 \mu\text{m}$ was measured by O’Dowd *et al.* (1992) and is shown in Figure 53 where $K_c(\hat{\psi})$ is the amplitude of the critical local stress intensity factor. The solid line is the toughness curve predicted by the formula $K_c(\hat{\psi}) = K_{Ic}/\cos \hat{\psi}$.

Wang and Suo (1990) developed a Brazilnut-sandwich specimen to measure the interfacial fracture toughness. Experiments were conducted with 1090 aluminum, 420 stainless steel, 27000 brass, and plexiglass as substrates and epoxy as the interlayer. The measured fracture data are shown in Figure 4. It is worth noting that the apparent toughness values in the range $\hat{\psi} > 60^\circ$ are quite high compared with those of $\hat{\psi} \approx 0^\circ$.

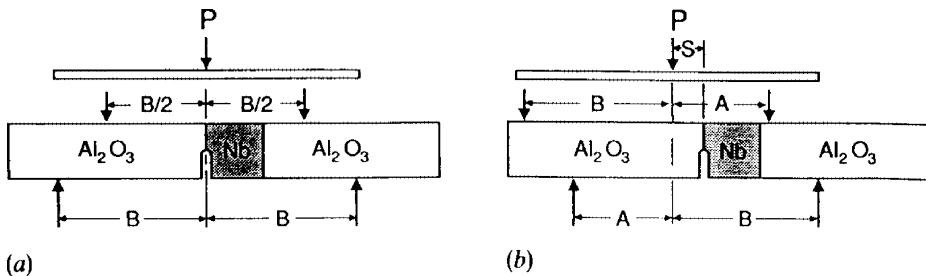


Figure 48 (a) Schematic representation of the symmetric bend specimen and (b) asymmetric bend specimen (source O’Dowd *et al.*, 1992).

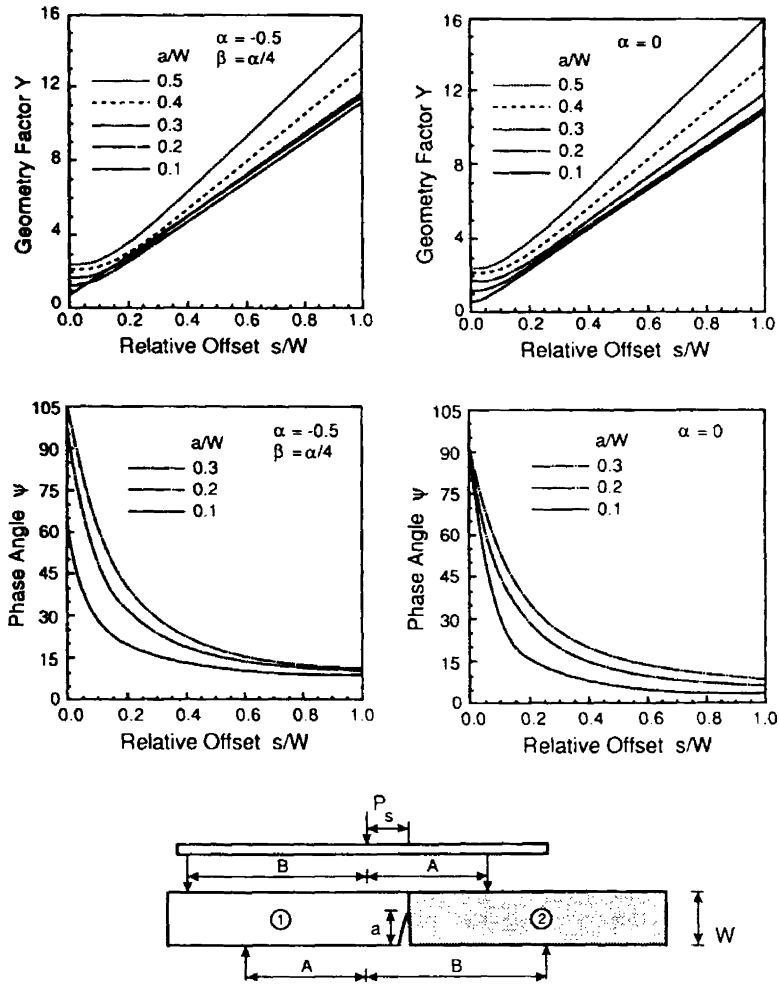


Figure 49 Calibration of the edge-notched shear of a bimaterial bar (reproduced by permission of Academic Press from “Advances in Applied Mechanics,” vol. 29, pp. 63–191).

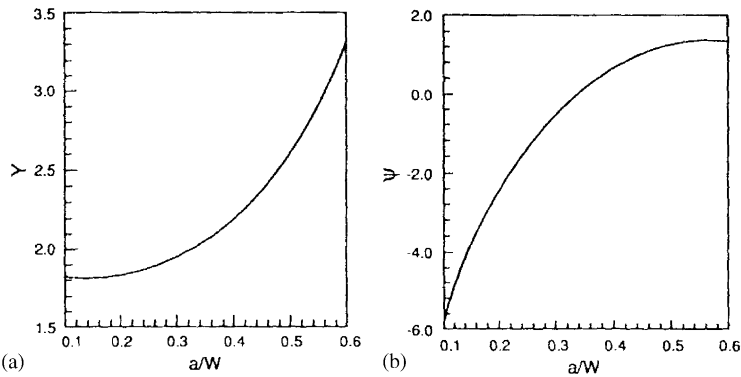


Figure 50 Calibration functions Y and ψ for symmetric four-point bend specimens, (a) dependence of Y on relative crack depth a/W and (b) dependence of ψ on a/W (source O’Dowd *et al.*, 1992).

8.03.5 INTERFACE CRACKS IN DISSIMILAR ANISOTROPIC MEDIA

Interface cracks in anisotropic solids were first analyzed by Gotoh (1967), Clements

and Sneddon (1971), and Willis (1971). Many interface crack problems were solved by Wang and Choi (1983), Ting (1986), Suo (1990a), Wu (1990), Wang *et al.* (1992), and Wang (1994). The mathematical structure of the interface crack tip fields has

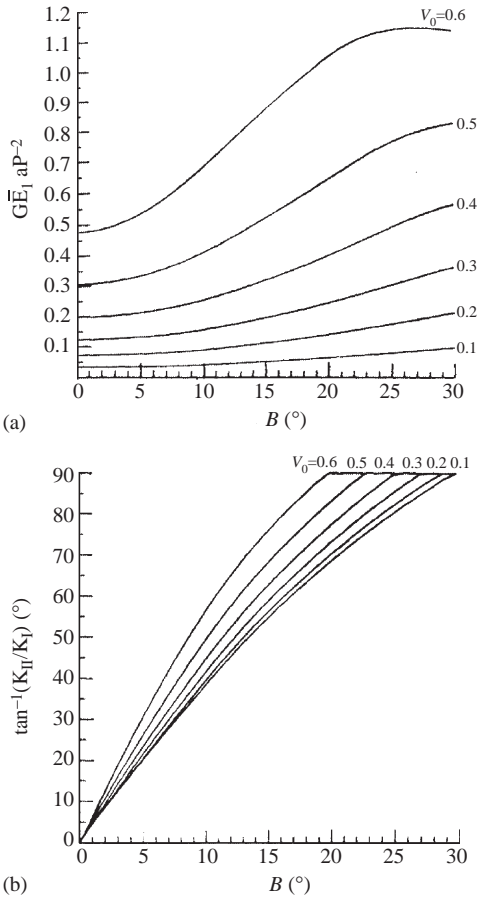


Figure 51 Homogeneous Brazil-nut calibration: (a) the normalized energy release rate and (b) the loading phase (source Atkinson *et al.*, 1982).

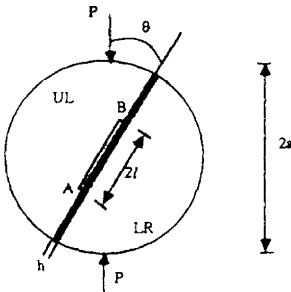


Figure 52 A Brazil-nut-sandwich in diametral compression.

been identified by Ting (1986) and Suo (1990a).

8.03.5.1 Basic Formulas

According to Lekhnitskii (1981) and Stroh (1958), the displacement and stress solution of the plane problem for anisotropic media can be expressed by three analytical functions $f_i(z_i)$, ($i = 1, 2, 3$) as

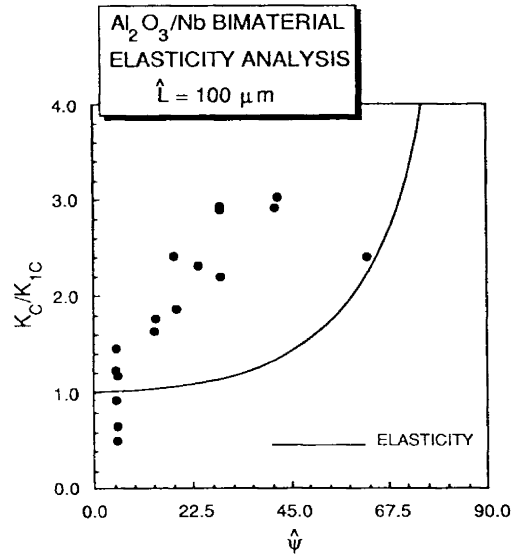


Figure 53 Comparison of $K_c(\hat{\psi})/K_{Ic}$ with experimental data for the alumina/niobium system (source O’Dowd *et al.*, 1992).

$$\begin{aligned}
 u_i &= 2\text{Re} \left[\sum_{j=1}^3 A_{ij} f_j(z_j) \right] \\
 T_i &= -2\text{Re} \left[\sum_{j=1}^3 L_{ij} f_j(z_j) \right] \\
 \sigma_{2i} &= 2\text{Re} \left[\sum_{j=1}^3 L_{ij} f'_j(z_j) \right] \\
 \sigma_{1i} &= -2\text{Re} \left[\sum_{j=1}^3 L_{ij} \mu_j f'_j(z_j) \right]
 \end{aligned}
 \tag{21}$$

where $z_j = x + \mu_j y$, μ_j are three distinct complex numbers with a positive imaginary part, which can be obtained as roots of a sixth-order characteristic equation.

Suo (1990a) introduced a positive definite Hermitian matrix $H = B_1 + \bar{B}_2$, where B_1 and B_2 are “ B matrices” for materials I and II, respectively. The definitions of “ A, B, L matrices” can be found in books by Lekhnitskii (1981) and Ting (1996).

8.03.5.2 Interface Crack in Anisotropic Bimaterials: Nonoscillatory Fields

Ting (1986), Qu and Bassini (1989), and Suo (1990a) have shown that if H is a real matrix, the oscillatory index is $\varepsilon = 0$, and the crack tip fields are nonoscillatory singularity fields, which can be expressed as

$$\sigma_{ij} = \frac{1}{\sqrt{2\pi r}} \left\{ K_1 \sigma_{ij}^I(\theta) + K_2 \sigma_{ij}^{II}(\theta) + K_3 \sigma_{ij}^{III}(\theta) \right\} \tag{22}$$

The stress intensity factors K_1, K_2 , and K_3 play the same role as those in homogeneous

materials. Equation (22) clearly shows that the crack tip stress field is independent of the elastic properties in materials I and II. The angular functions in Equation (22) are identical to those for a crack in homogeneous materials. Specially, the functions for material I are the same as those for a crack in a homogeneous material of the same elastic constants. The same holds true for material II. Consequently, these functions can be found in the article by Sih *et al.* (1965) on cracks in homogeneous anisotropic solids.

The energy release rate G and the opening displacement field δ take the form

$$G = \frac{1}{4} k^T H k \quad (23a)$$

$$\{\delta_x, \delta_y, \delta_z\} = \sqrt{\frac{2r}{\pi}} H k \quad (23b)$$

where $k = \{K_2, K_1, K_3\}$.

8.03.5.3 Interface Crack in Anisotropic Bimaterials: Oscillatory Fields

Suo (1990a) showed that the crack tip fields consist of two types of singularities, namely an oscillatory field and a nonoscillatory field,

$$\sigma_{ij} = \frac{1}{\sqrt{2\pi r}} \left\{ \text{Re}(K r^{i\epsilon}) \sigma_{ij}^{(1)}(\theta) + \text{Im}(K r^{i\epsilon}) \sigma_{ij}^{(2)}(\theta) + K_3 \sigma_{ij}^{(3)}(\theta) \right\} \quad (24)$$

where $K = K_1 + iK_2$.

The energy release rate G is given by

$$G = \frac{\bar{W}^T (H + \bar{H}) W}{4 \cosh^2 \pi \epsilon} K \bar{K} + \frac{1}{8} W_3^T (H + \bar{H}) W K_3^2 \quad (25)$$

where ϵ is the eigenvalue and W , W_3 are eigenvectors, which were identified by Suo (1990a).

8.03.5.4 Crack Kinking out of an Interface

A solution was obtained by Miller and Stock (1989) for the problem of a crack branching off the interface between two dissimilar anisotropic materials. Numerical results for the stress intensity factors at the tip of branched crack were obtained for some special cases in their paper.

A complete analysis of kinking of an interface crack between two dissimilar anisotropic elastic materials was presented by Wang *et al.* (1992) and Wang (1994). The branched crack was treated as distributed dislocations. In their papers, a set of singular integral equations for the distribution function of the dislocation density were developed. Explicit formulas of

stress intensity factors and energy release rate for the branched crack were obtained for orthotropic and misoriented orthotropic bicroystals. The role of the stress parallel to the interface, T , is taken into account in these formulas. According to the work of Wang *et al.* (1992) and Wang (1994), the stress intensity factors at the kink tip can be expressed as

$$\begin{aligned} K_I^{\text{kink}} &= C_{11} \text{Re}(K a^{i\epsilon}) + C_{12} \text{Im}(K a^{i\epsilon}) + d_1 T a^{1/2} \\ K_{II}^{\text{kink}} &= C_{21} \text{Re}(K a^{i\epsilon}) + C_{22} \text{Im}(K a^{i\epsilon}) + d_2 T a^{1/2} \end{aligned} \quad (26)$$

where coefficients C_{ij} were given by Wang *et al.* (1992) and d_i were obtained by Wang (1994). They are functions of the kinking angle ω and elastic constants of materials I and II.

For in-plane problem, the energy release rate for the branched crack takes the form

$$G^{\text{kink}} = k_*^T (B_2 + \bar{B}_2) k_* / 4 \quad (27)$$

where $k_* = \{K_{II}^{\text{kink}}, K_I^{\text{kink}}\}$ is a column vector and B_2 is the matrix for material II, into which the main crack is branched.

Consider two cubic orthotropic crystals with elastic constants $\lambda = 1$, and $\rho = -0.19$ which forms a symmetric tilt grain boundary with $\theta_1 = \theta_2 = 38.9^\circ$ as shown in Figure 54. The (x, y) plane is a plane of mirror symmetry. The interface crack is running in the x -direction. The matrix H is real for such a symmetric tilt grain boundary. The coefficients C_{ij} as the functions of the kinking angle ω are shown in Figure 55. The ratio of the energy release rate G^{kink} of a kinked crack to the interface energy release rate G_i as a function of the kinking angle and the loading mixity is shown in Figure 56.

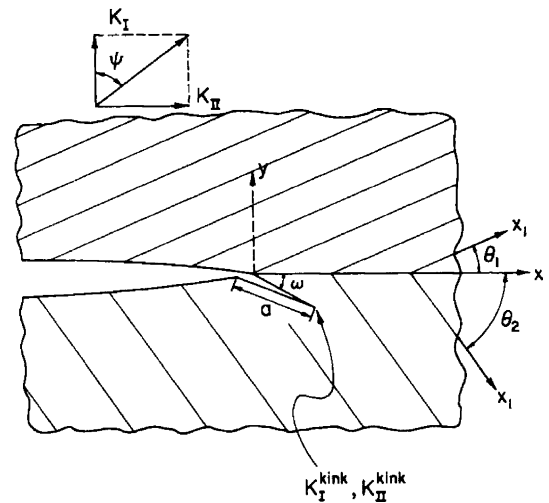


Figure 54 A schematic of a small-scale kink problem. The principal direction x_1 is tilted from the x -axis by θ_1 and θ_2 , respectively. The parent crack is under mixed-mode load.

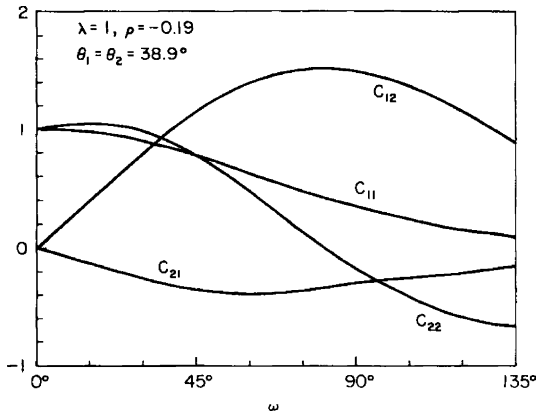


Figure 55 Coefficient C_{ij} for a symmetric tilt cubic bicrystal.

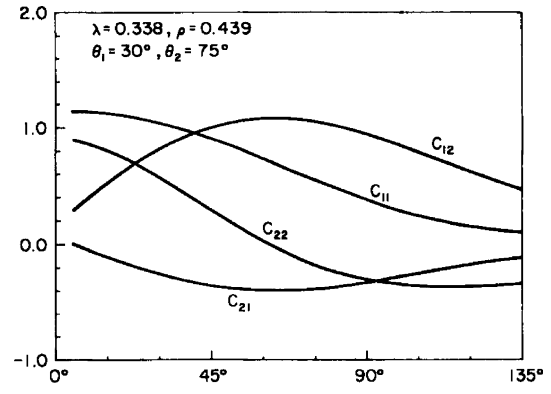


Figure 57 Coefficient C_{ij} for an orthotropic bicrystals.

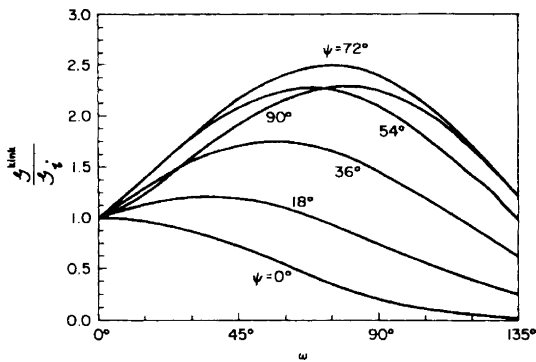


Figure 56 Crack driving force ratios $G_{\max}^{\text{kink}}/G_i$ as a function of the kink angle ω under several remote loading mixities $\psi = \tan^{-1}(K_{II}/K_I)$.

Figures 57 and 58 depict the calculation results for the case of $\theta_1 = 30^\circ, \theta_2 = 75^\circ$. The interface is a typical asymmetric tilt grain boundary. The generalized Dundurs' parameters are $\alpha = 0.0583, \beta = 0$. The coefficients C_{ij} as functions of the kinking angle ω are shown in Figure 57. Figure 58 shows the ratio of the maximum energy release rate G_{\max}^{kink} of the kinked crack to the interface energy release rate G_i as a function of the loading phase. The influence of T-stress on the ratio of $G_{\max}^{\text{kink}}/G_i$ is clearly illustrated in this figure with parameter $\eta = T\sqrt{a}/|K|$.

Now consider two dissimilar orthotropic materials bonded with their principal axes aligned. The interface is on the x -axis and the crack is on the negative x -axis. For an orthotropic material, the anisotropy is characterized by two parameters λ and ρ (Suo, 1990b). For single crystal Cu, the typical values are $\lambda_1 = 1, \rho_1 = -0.19$, while $\lambda_2 = 0.12, \rho_2 = 6.24$ for boron/epoxy composite.

Figures 59 and 60 indicate the effect of parameter α on the ratio of the maximum energy release rate G_{\max}^{kink} of the kinked crack to the

interface energy release rate G_i . It is clear that the ratio $G_{\max}^{\text{kink}}/G_i$ will increase when α increases.

8.03.6 ELASTIC-PLASTIC FRACTURE MECHANICS FOR AN INTERFACE CRACK

8.03.6.1 Elastic-Plastic Analyses of Interface Crack

Using the finite element method Shih and Asaro (1988, 1989, 1990) and Zywickz (1988) investigated elastic-plastic cracks on bimaterial interfaces. Instead of complex stress intensity factor K , Shih and Asaro (1988) introduced a complex stress intensity factor $Q = KL^{ic}$, where L is the crack length. The traction directly ahead of the crack tip for an elastic interface crack can be expressed as

$$\sigma_{22} + i\sigma_{12} = \frac{Q}{\sqrt{2\pi r}} \left(\frac{r}{L}\right)^{ic} \quad (28)$$

It is worth noting that Q has the unit of stress $\times (\text{length})^{1/2}$ in analogy with the definition of stress intensity factor in homogeneous media and the phase angle for Q is independent of length scale. For a center cracked panel, Q is given by $Q = (\sigma_y^\infty + i\tau_{xy}^\infty)(1 + 2i\varepsilon)\sqrt{\pi L}/2$ for the right hand crack tip.

Consider an interface crack between an elastic-plastic material and a rigid substrate. The elastic-plastic material obeys the Ramberg-Osgood stress-strain relation. The near tip stress fields for "opening" dominated external loading take the form

$$\sigma_{ij} = \sigma_0 \left(\frac{J}{\alpha\sigma_0\varepsilon_0 r}\right)^{1/(n+1)} h_{ij}(\theta, \hat{r}, \xi) \quad (29)$$

Here J denotes the J -integral and h_{ij} is a nonsingular function, which slowly varies with $\hat{r} = \sigma_0 r/J$. The function h_{ij} also depends on the phase angle $\xi = \psi + \varepsilon \ln(Q\hat{Q}/\sigma_0^2 L)$. Figure 61

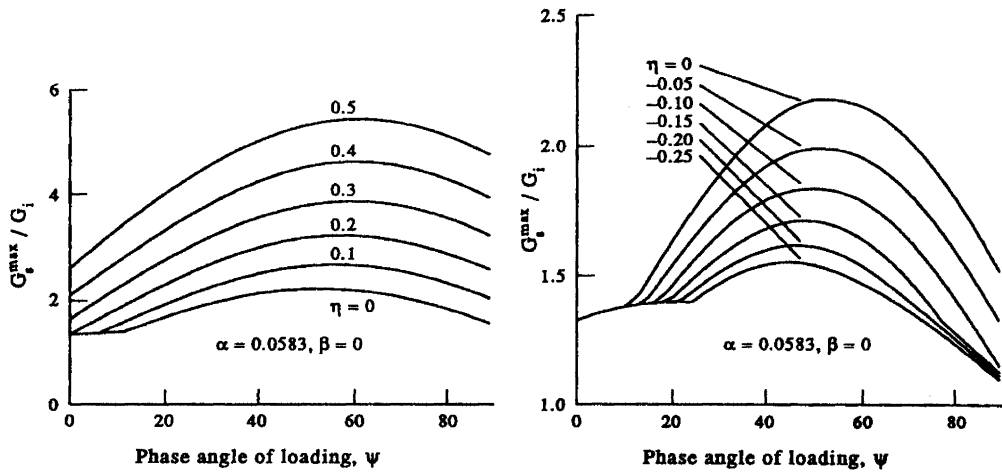


Figure 58 Ratio of the maximum energy release rate of kinked crack to interface energy release rate as a function of the loading phase. Here $G_s^{\max} = G_{\max}^{\text{kink}}$.

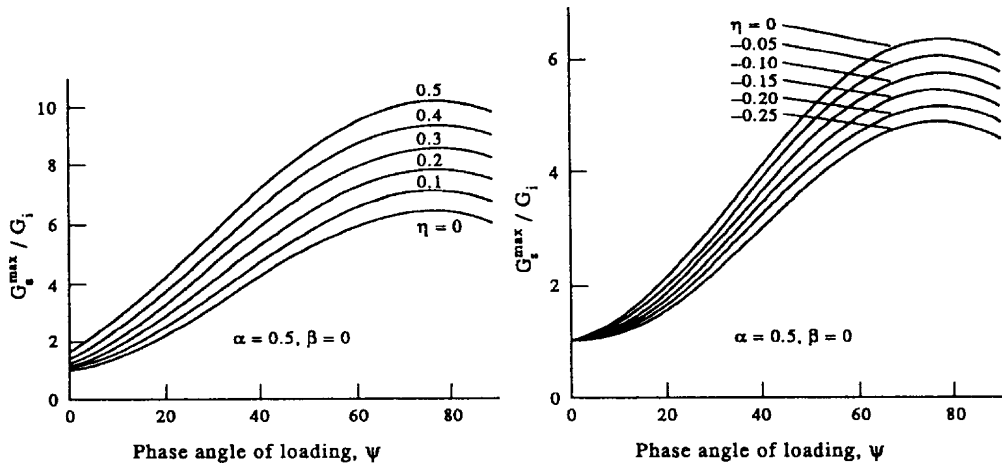


Figure 59 Ratio of the maximum energy release rate of kinked crack to interface energy release rate as a function of the loading phase. Here $G_s^{\max} = G_{\max}^{\text{kink}}$.

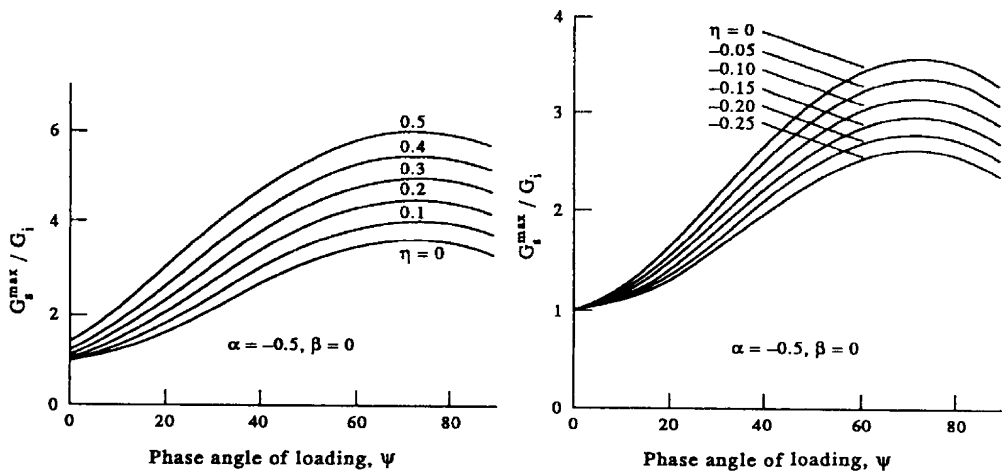


Figure 60 Ratio of the maximum energy release rate of kinked crack to interface energy release rate as a function of the loading phase. Here $G_s^{\max} = G_{\max}^{\text{kink}}$.

shows the normal stresses ahead of the crack tip for the cases of $n = 3$ and $n = 10$, respectively. The dashed line curve denotes the finite element calculation results for a purely elastic material. The break in the dashed line near $r/a = 10^{-9}$ corresponds to the stress changing from tension to compression. Figure 61(a) gives the results for strongly hardening material ($n = 3$). When the load level is very low, $\sigma^\infty/\sigma_0 = 2.0 \times 10^{-5}$, the plastic zone is confined to a distance of about $r_p/a = 10^{-11}$, the near tip stress also has the oscillatory tendency. The stress is negative within the plastic zone. At the next load level $\sigma^\infty/\sigma_0 = 2.0 \times 10^{-4}$, the stress is positive over the entire plastic zone. At the high load level $\sigma^\infty/\sigma_0 = 6.0 \times 10^{-3}$, the normal stress increases monotonically as the crack tip is approached and the oscillatory tendency disappears. Figure 61(b) shows the results for low hardening material. In a low level of remote loading $\sigma^\infty/\sigma_0 = 2.0 \times 10^{-5}$, the hoop stress in the outer plastic zone is compressive; in the next remote stress level, $\sigma^\infty/\sigma_0 = 2.0 \times 10^{-4}$, the hoop stress is essentially not affected by the elastic stress fields; and in the final load level, $\sigma^\infty/\sigma_0 = 6.0 \times 10^{-3}$, the hoop stress is positive over the entire range studied.

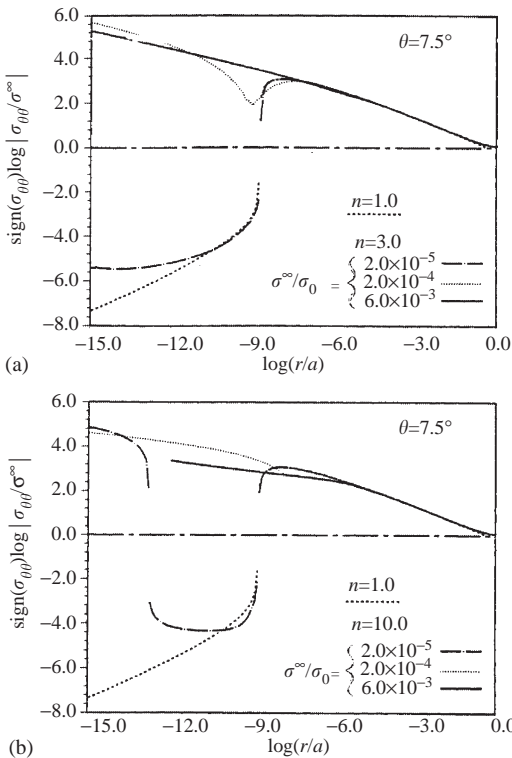


Figure 61 Plots of log of normalized hoop stress ($\theta = 7.5^\circ$) against log of normalized distance for the interface crack: (a) $n = 3$ material and (b) $n = 10$ material (source Shih and Asaro, 1988).

The angular variation of the normalized stresses $\hat{\sigma}_{ij}$ at two fixed distances from crack tip is plotted in Figures 62(a), (c), and (e) for three remote load levels corresponding to $\xi = -1.36, -0.727$, and -0.071 , respectively. The stress distributions deep inside the plastic zone are shown in Figures 62(b), (d), and (f).

8.03.6.2 Crack Tip Fields for a Bimaterial Interface

The exact asymptotic solutions of the HRR type for a plane strain crack lying along an interface between an elastic-plastic power law hardening material (as material I) and a rigid substrate (as material II) were presented by Wang (1990) and Champion and Atkinson (1991). They found that a separable asymptotic solution satisfying the traction free condition on the crack faces only exists at a single mode mixity $M^P = (2/\pi) \tan^{-1}(\hat{\sigma}_\theta(0)/\hat{\tau}_{r\theta}(0))$, the value of which depends on the hardening exponent n . Sharma and Aravas (1993) confirmed Wang's solution. The asymptotic stress fields have a similar structure to that of the classic HRR fields of a homogeneous material. The singularity exponent is $s = -1/(n + 1)$.

The angular variations of normalized stresses are plotted on Figures 63–65 for the cases of $n = 3, 5$, and 10 , respectively. The corresponding values of M^P are 0.96056, 0.93728, and 0.91516, respectively. The stress component σ_r has a jump across the interface, which arises from the mismatch of elastic-plastic properties across the interface.

Exact mathematical analyses for an interface crack between two dissimilar elastic-plastic materials were performed by Xia and Wang (1992). The angular variations of normalized stresses for the asymptotic solution at a crack tip, which satisfy the traction free conditions on the crack faces, are given in Figure 66.

As pointed out by Shih (1991), Wang's solutions for $n = 3, 5$, and 10 are similar to the solutions reported by Shih and Asaro (1989) in their Figure 9 for $\xi = -0.551$ and $\xi = -0.027$, which display features consistent with a separable mode I like fields. The comparison of Wang's solution with Shih and Asaro's solution is also shown in Figure 66 (Xia and Wang, 1992). Note that Wang's solution agrees very well with the finite element solution given by Shih and Asaro (1989).

8.03.6.3 Elastic-Plastic Solutions with a Contact Zone

Zywick and Parks (1990) developed slip line solutions for the near tip region of a plane strain crack with a contact zone lying along an

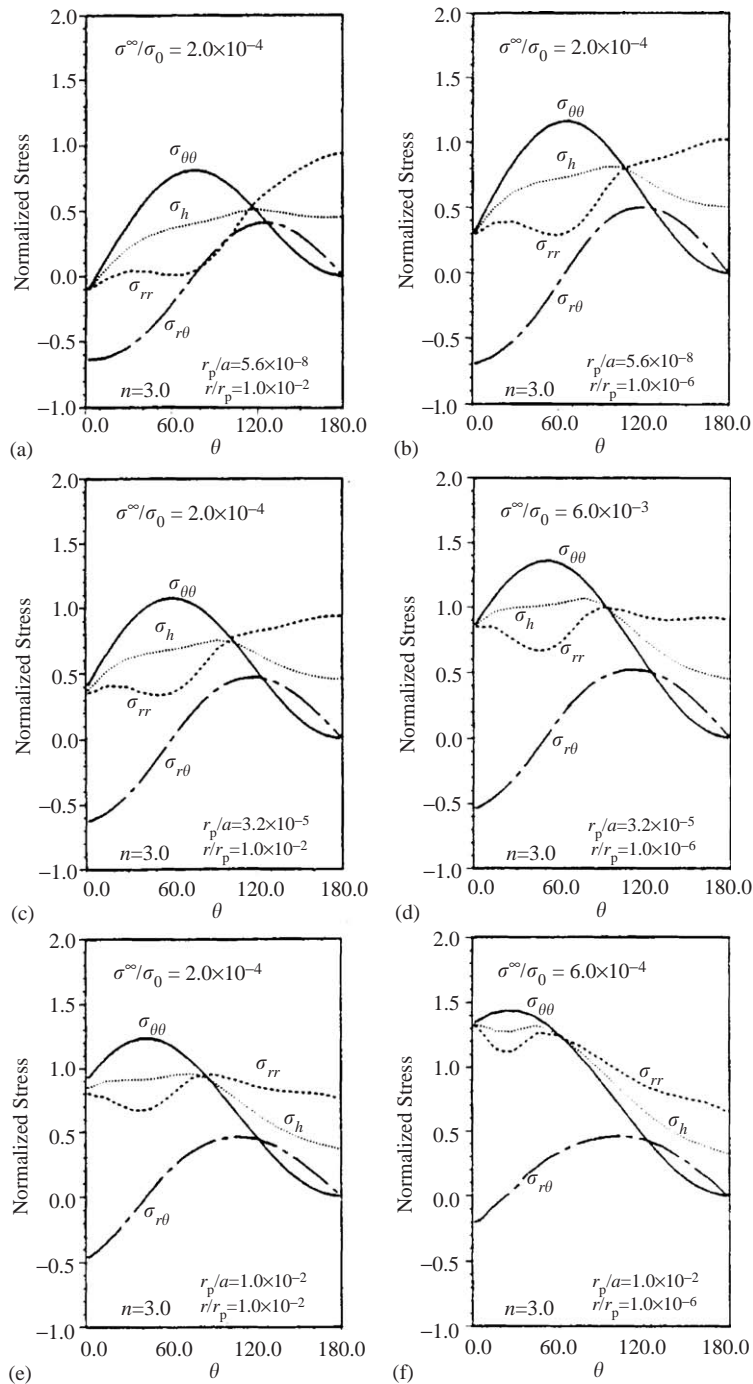


Figure 62 Plots of angular variations of normalized stresses for the interface crack with $n = 3$ at two distances within the plastic zone and for three remote stress levels (source Shih and Asaro, 1988).

interface between an elastic-perfectly-plastic solid and a rigid substrate. Aravas and Sharma (1991) and Xia and Wang (1992) considered a plane strain crack with a contact zone along the interface between an elastic-plastic power law hardening material and a rigid substrate. The solution given by them shows that the asymptotic solution is separable in r and θ , where (r, θ) are polar coordinates centered at

the crack tip. The mathematical structure of the crack tip fields is similar to that of the classic HRR fields in a homogeneous material. But the angular variations of stress components near a crack tip are different from the HRR singularity fields in a homogeneous material. Figure 67 shows the angular variation of stress components at the crack tip for $n = 3$ and $n = 10$. All stress components have the

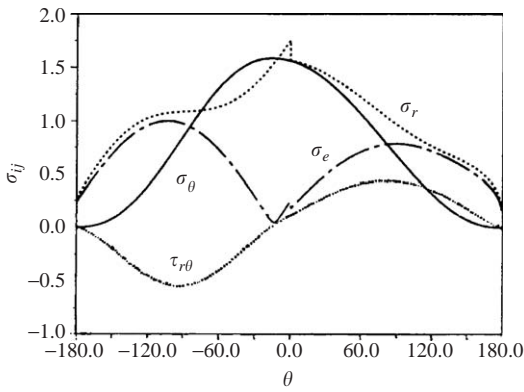


Figure 63 Angular variation of normalized stresses near the tip of a crack, which lies on the interface between an elastic–plastic material with hardening exponent $n = 3$ and a perfect elastic material.

$r^{-1/(n+1)}$ singularity, which is in contrast with the Comninou’s singularity field for the elastic solution of an interface crack with contact zone. Directly ahead of the crack tip, the normal stress is negative and the shear stress is positive. Behind the crack tip the normal stress is also negative and the shear stress is zero due to the frictionless contact of two crack faces. In other words, a necessary condition for the crack surfaces to remain closed near the crack tip is that the singular shear stress $\tau_{r\theta}(r, 0) > 0$. Alternatively, the Comninou’s elastic singular shear stress requires that the singular shear stress $\tau_{r\theta}(r, 0) < 0$.

In order to verify the elastic–plastic asymptotic solutions, Aravas and Sharma (1991) carried out finite element calculations under a small-scale yielding condition. The

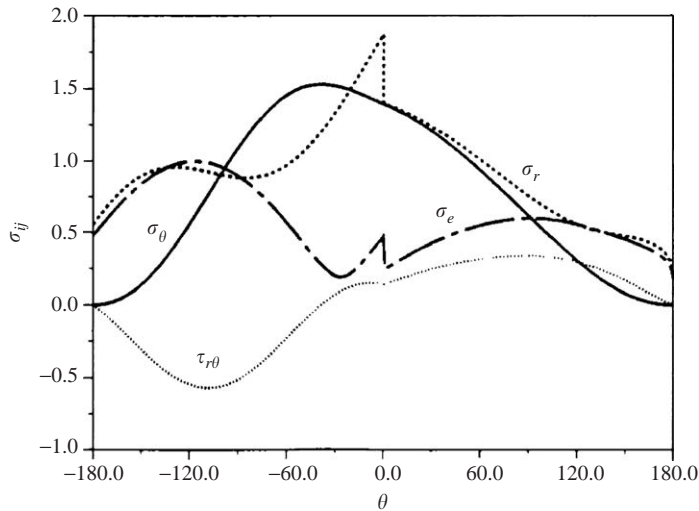


Figure 64 Angular variation of normalized stresses near the tip of a crack, which lies on the interface between an elastic–plastic material with hardening exponent $n = 5$ and a perfect elastic material.

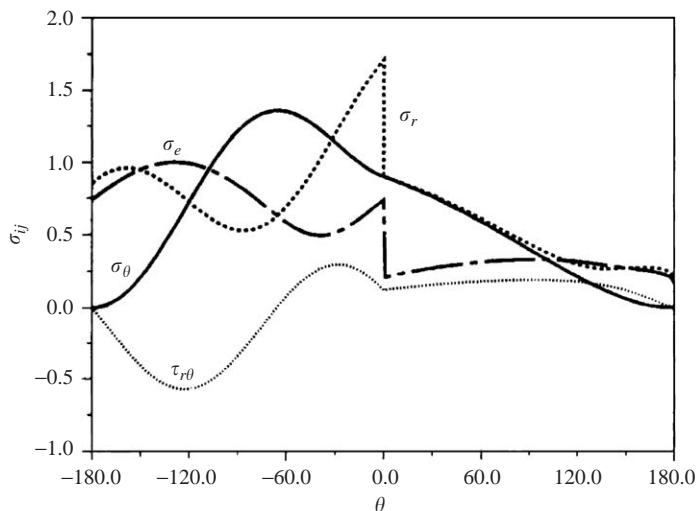


Figure 65 Angular variation of normalized stresses near the tip of a crack, which lies on the interface of an elastic–plastic material with hardening exponent $n = 10$ and a perfect elastic material.

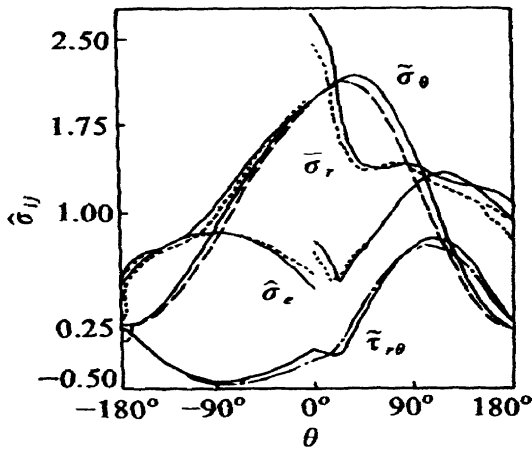


Figure 66 Angular variation of stress for the case $n_1 = 3$ and $n_2 = 5$. Solid lines after Xia and Wang (1992); dashed lines after Shih and Asaro (1990).

Comninou's asymptotic elastic displacement field with $K_2 < 0$ is applied on a remote semicircular boundary. The radial variation of the equivalent stress along $\theta = 86.3^\circ$ for $n = 10$ is shown in Figure 68. Figure 69 depicts the angular variation of the equivalent stress at a crack tip. The hollow circles indicate the results of finite element solution. It is clear that the asymptotic solutions by Aravas and Sharma agree well with the finite element solutions.

Xia and Wang (1992) performed exact mathematical analyses for interface cracks between two dissimilar elastic-plastic materials. The angular variation of normalized stresses for the asymptotic solution at the crack tip with a contact zone along the interface between a power law hardening material and a pure elastic material is shown

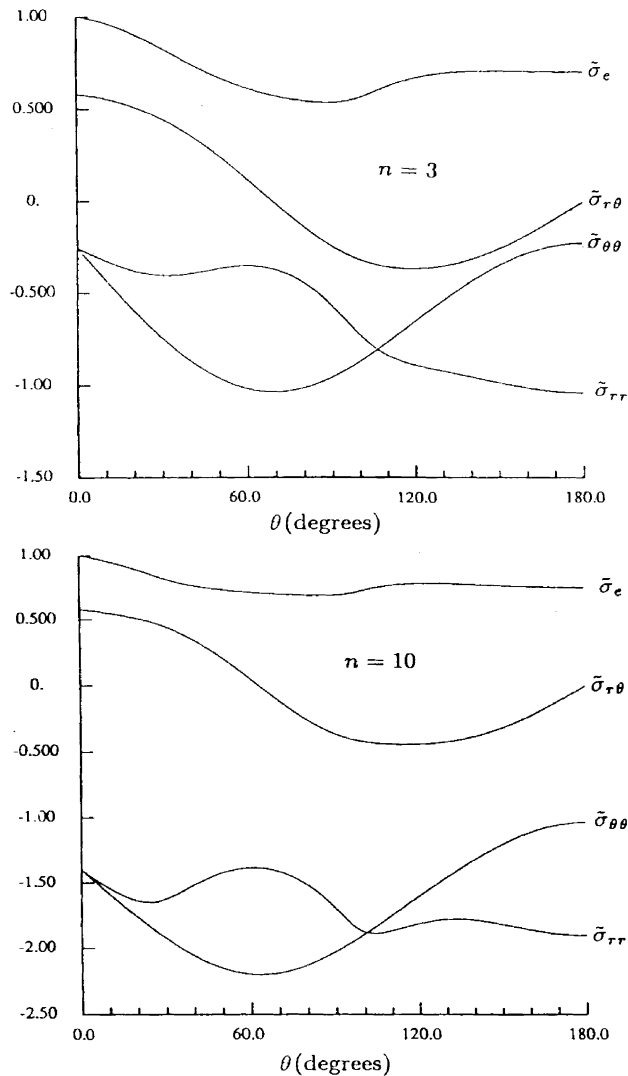


Figure 67 Angular variation of stress components at the tip of an interfacial crack with contact zone between an elastic-plastic power law hardening material and a rigid substrate (source Aravas and Sharma, 1991).

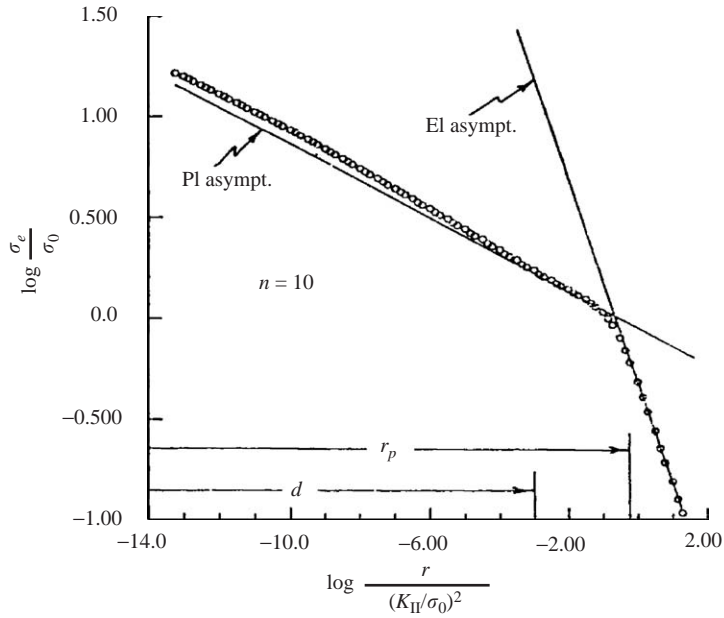


Figure 68 Radial variation of normalized Mises equivalent stress σ_e along $\theta = 86.3^\circ$ for $n = 10$. The open circles indicate the results of the finite element solution (source Aravas and Sharma, 1991).

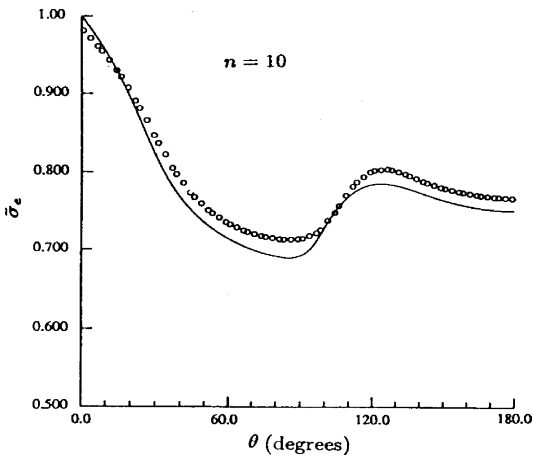


Figure 69 Angular variation of normalized Mises equivalent stress $\bar{\sigma}_e$ at the crack tip for $n = 10$. The circles indicate the results of the finite element (source Aravas and Sharma, 1991).

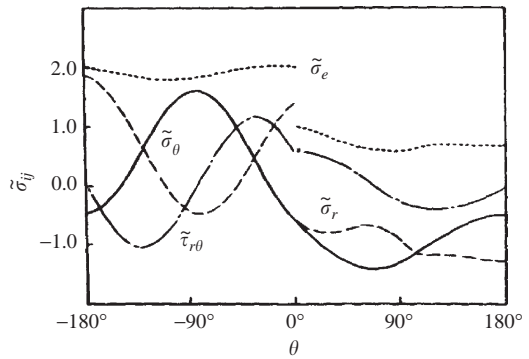


Figure 70 Angular variation of normalized stress ($M^P = -0.51541$). Material I is a power law hardening elastic-plastic material ($n_1 = 5$) and material II is a perfectly elastic material.

in Figure 70 for $n_1 = 5$. The solution is separable in r and θ , which exists only for $M^P = (2/\pi)\tan^{-1}(\bar{\sigma}_\theta(0)/\bar{\tau}_{r\theta}(0)) = -0.51541$.

The solutions provided by Wang (1990), Aravas and Sharma (1991), and Xia and Wang (1992) are fully continuous. It means that the stress components, displacements, and the stress function F and its derivatives up to the third order within materials I and II are all continuous and the tractions and displacements are also continuous across the interface.

For any assigned M^P , the separable solution of HRR type which contains a weak discontinuous line was presented by Xia and Wang (1992). The weak discontinuous line exists in the material with lower hardening (larger n). The third-order derivative of the stress function has a jump across the line. This is the only difference as compared with the fully continuous solution. In order to verify the existence of the solution with a weak discontinuous line, let us consider the following functional equation introduced by K. R. Wang and T. C. Wang (1987):

$$\Pi_1 \sin \theta + \Pi_2 \cos \theta + (1 + ns)\bar{u}_\theta \Pi_3 = 0 \quad (30)$$

The functions Π_x can be found in the paper by Xia and Wang (1992) and $\Pi_3 = \bar{\sigma}_\theta \cos \theta +$

$\tilde{\tau}_{r\theta} \sin \theta$. Symbols $\tilde{u}_\theta(\theta)$, $\tilde{\sigma}_\theta(\theta)$, and $\tilde{\tau}_{r\theta}(\theta)$ stand for angular distributions of the displacement component and the stress components of the first-order asymptotic solution respectively. Equation (30) is equivalent to the original governing equation for the angular distribution function $F(\theta)$ of the stress function. Wang (1986) proved that if $\Pi_3(\theta_A)$ vanishes at a certain polar angle $\theta = \theta_A$, then Equation (30) is always satisfied for any $F'''(\theta)$ value on both sides of the radius line $\theta = \theta_A$. This means that the weak discontinuity is allowable at $\theta = \theta_A$ where the third derivative $F'''(\theta)$ is discontinuous.

The angular variation of singular stresses for the crack along an interface between an elastic-plastic material with $n = 5$ (as material I) and a perfectly elastic material (as material II) is shown in Figure 71. The discontinuous line lies at about $\theta_A \approx 160^\circ$. The parameter $M^p = 0.832$, which nearly corresponds to the result by Shih and Asaro (1989) in their Figure 9. The comparison between the two results is also shown in Figure 71. The results for the normal stress σ_θ and the shear stress $\tau_{r\theta}$ agree well in the entire region $0 < \theta < \pi$. The results for the normal stress σ_r and the effective stress σ_e agree well in the interval $0 < \theta < \theta_A$. But after θ_A , there are considerable differences between the two results. The solutions with a weak discontinuous line for $M^p = 0.3$ and 0.6 are plotted in Figure 72.

Across the weak discontinuous line, the displacement angular function \tilde{u}_θ has a jump. In order to guarantee the displacement continuity, one can assume that there is a complex zone around the weak discontinuous line $\theta = \theta_A$ as shown in Figure 73. In this complex zone, the crack tip fields cannot be expressed in terms of separable variables. Since the displacements

near the crack tip can be expressed as $u_i = r^{1/(n_1+1)}\tilde{u}_i(\theta)$ outside the complex zone, the displacement u_θ is continuous across the weak discontinuous line at the crack tip.

8.03.6.4 High-order Solutions

High-order solutions for a crack along an interface between two dissimilar bimaterial have been studied by Aravas and Sharma (1991), Sharma and Aravas (1993), and Xia and Wang (1994a, 1994b). The constitutive equation of materials I and II is described by the J_2 deformation theory for a Ramberg-Osgood uniaxial stress-strain behavior. Let n_1 and n_2 be the strain hardening exponents of materials I and II respectively. Without loss of generality, one can assume $n_1 > n_2$. It

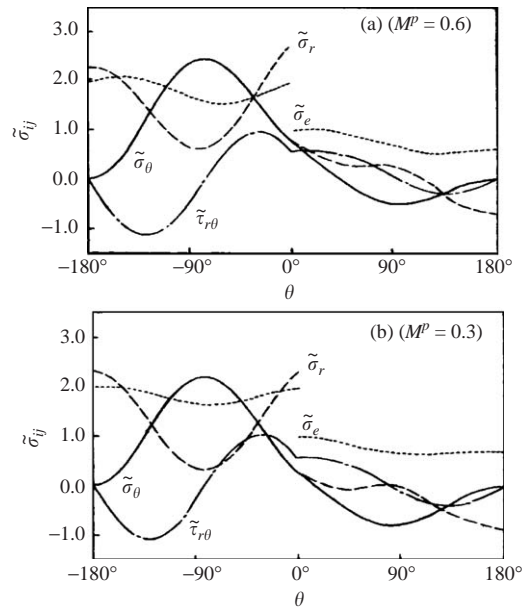


Figure 72 Angular variation of normalized stresses. Material I is an elastic-plastic material ($n_1 = 5$) and material II is a perfectly elastic material.

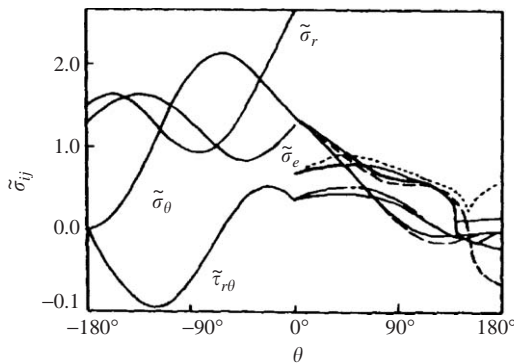


Figure 71 Angular variation of stresses ($M^p = 0.832$). Material I is elastic-plastic ($n_1 = 5$) and material II is perfectly elastic. Solid lines after Xia and Wang (1992); dashed lines after Shih and Asaro (1989).

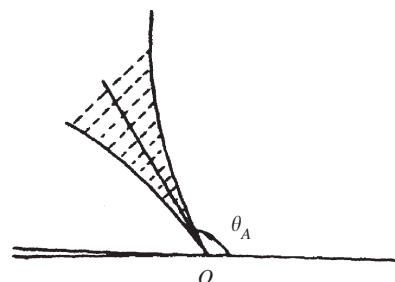


Figure 73 The complex stress zone.

means that material I is more compliant than material II.

As pointed out by Shih and Asaro (1988) and Wang (1990), the singularity exponents of the stress fields in materials I and II are the same due to traction continuity along the interface. But the singularity exponent of the strain fields in material I is larger than that of material II. If E_{I1} and E_{I2} designate the tangent moduli of materials I and II, respectively, then $E_{I1}/E_{I2} \rightarrow 0$, as $r \rightarrow 0$. This suggests that, as $r \rightarrow 0$, the material system would behave increasingly like a plastically deforming material bonded to a rigid substrate. Therefore in the asymptotic sense, we have $u_r(r, 0^+) = u_\theta(r, 0^+) = 0$.

8.03.6.4.1 High-order solutions with traction free crack surfaces

The first-order asymptotic solution has been discussed in Sections 8.03.6.1 and 8.03.6.2. The stresses of first order solution have the singularity $r^{-1/(m_1+1)}$ and the displacements of the first-order solution satisfy the following condition on the interface: $u_r^{(1)}(r, 0^+) = u_\theta^{(1)}(r, 0^+) = 0$. The displacements of the first-order solution in material I can be expressed as $u_i^{(1)}(r, \theta) = r^{1/(m_1+1)} \tilde{u}_i^{(1)}(\theta)$. Since the tractions are continuous across the interface, the stress fields of the first-order solution in material II take the form $\sigma_{ij}^{(1)} = r^{-1/(m_1+1)} \tilde{\sigma}_{ij}^{(1)}(\theta)$, the

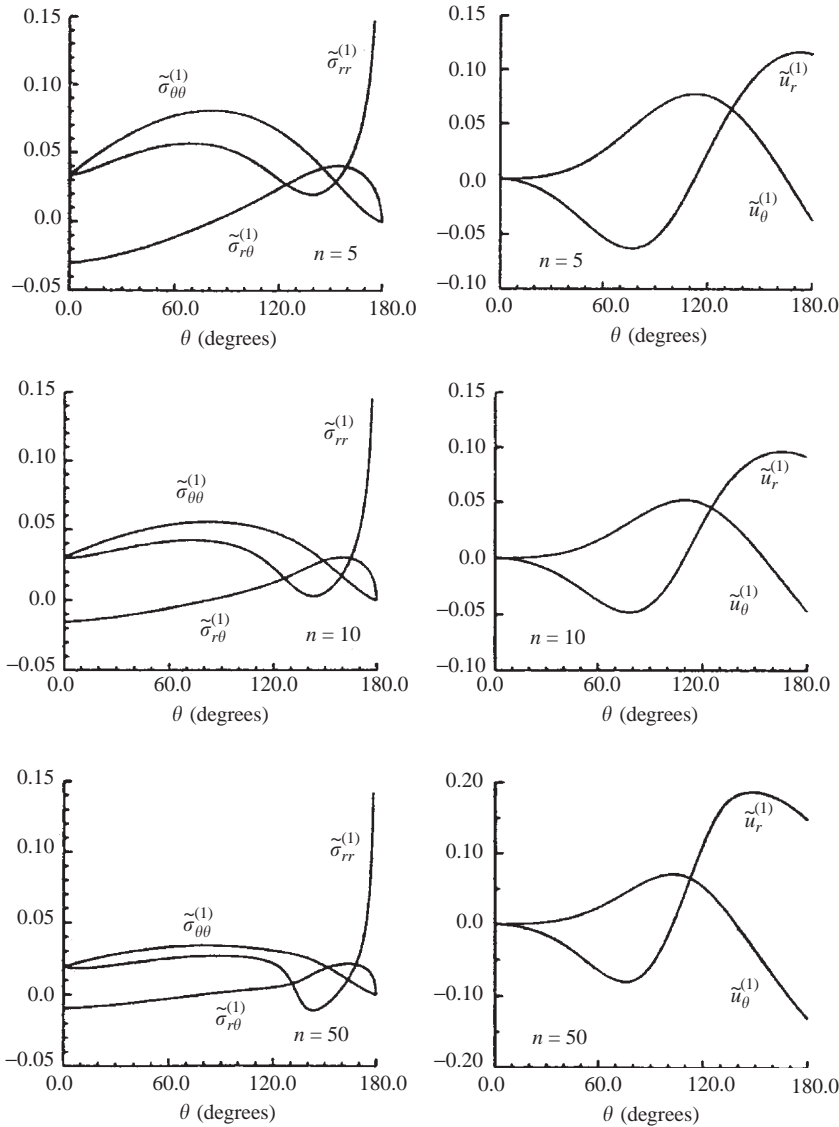


Figure 74 Angular variations of the second-order stress and displacement components for $n = 5, 10,$ and 50 (source Sharma and Aravas, 1993).

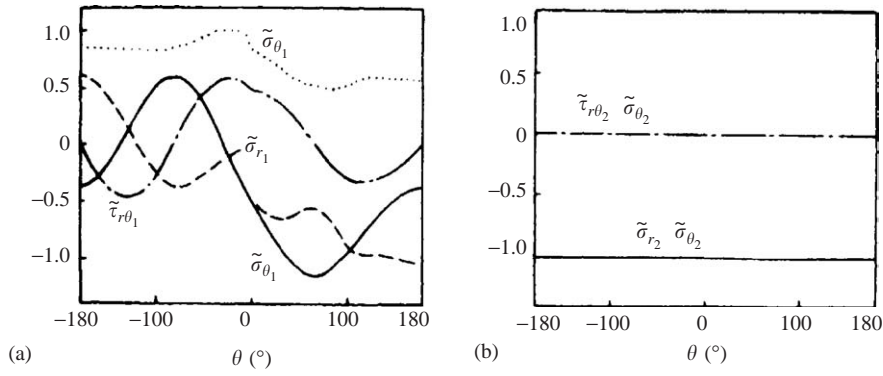


Figure 75 Angular distributions of stresses near the interface crack tip for $n_1 = 5, n_2 = 3$.

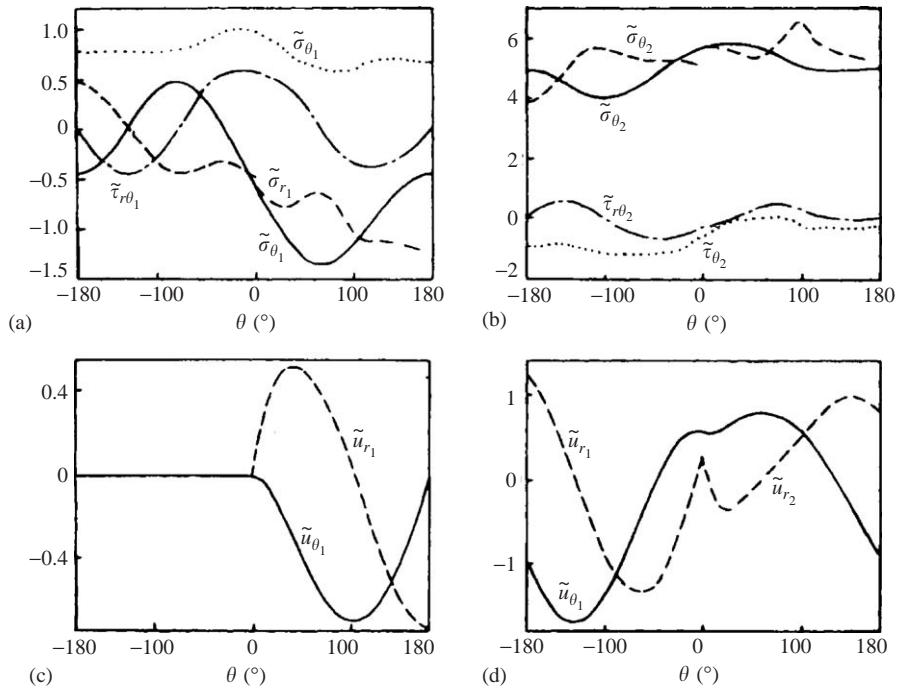


Figure 76 Interface crack tip fields for $n_1 = 5, n_2 = 4.5$.

corresponding strains and displacements in material II can be expressed as $\varepsilon_{ij}^{(1)} = r^{-n_2}/(n_1 + 1)\tilde{\varepsilon}_{ij}^{(1)}(\theta)$ and $u_i^{(1)}(r, \theta) = r^{(n_1+1-n_2)/(n_1+1)}\tilde{u}_i^{(1)}(\theta)$.

Now we search the second-order solution in material I. Besides the traction free condition on the crack surface, the second-order solution should satisfy the following condition along the interface: $u_r^{(2)}(r, 0^+) = u_\theta^{(2)}(r, 0^+) = 0$. Using a method similar to that proposed by Li and Wang (1986), one can get the second-order solution.

The second-order solutions take the form $\sigma_{ij}^{(2)} = r^{s_2}\tilde{\sigma}_{ij}^{(2)}(\theta)$ and $\varepsilon_{ij}^{(2)} = r^{\Delta s_2 - n_1/(n_1+1)}\tilde{\varepsilon}_{ij}^{(2)}(\theta)$, $u_i^{(2)}(r, \theta) = r^{1+\Delta s_2 - n_1/(n_1+1)}\tilde{u}_i^{(2)}(\theta)$, where s_2 is the

smallest eigenvalue of the governing equation of the high-order field, $\Delta s_2 = s_2 - s_1$.

Sharma and Aravas (1993) obtained the second-order solution. Figure 74 shows the angular distribution of the stress fields for the second-order solution.

Comparing the power exponents of the second-order displacement fields in material I and first-order displacement fields in material II, one concludes that if $\Delta s_2 < (n_1 - n_2)/(n_1 + 1)$, the second-order solution by Sharma and Aravas (1993) holds true, otherwise the second-order solution should match the displacement fields of the first-order solution in material II. It means that the second-order solution in material I should satisfy the following condition along the interface: $u_r^{(2)}(r, 0^+) =$

$u_r^{(1)}(r, 0^-)$, $u_\theta^{(2)}(r, 0^+) = u_\theta^{(1)}(r, 0^-)$ with $\Delta s_2 = (n_1 - n_2)/(n_1 + 1)$. Such solutions have been discussed by Xia and Wang (1994b).

8.03.6.4.2 High-order solution with a frictionless contact zone

The second-order solution for an interface crack between a power law hardening material and a rigid substrate was obtained by Aravas and Sharma (1991). They pointed out that the second-order solution with frictionless contact zone corresponds to a constant stress field. An accurate second-order solution for an interface between two dissimilar elastic-power law hardening plastic materials with a frictionless contact zone was presented by Xia and Wang (1994a). They concluded that if $\Delta s_2 < (n_1 - n_2)/(n_1 + 1)$ and $\Delta s_2 < (n_1 - 1)/(n_1 + 1)$, the second-order solution with frictionless contact zone corresponds to a constant stress field. Otherwise the second-order solution with a frictionless contact zone will be different from a constant stress field. Figure 75 shows the angular distribution of the first and second-order stress fields in the case of $n_1 = 5$ and $n_2 = 3$. It is clear that the second-order stress fields correspond to a constant stress. Figure 76 depicts the angular distributions of the first and second-order stress and displacement fields in the case of $n_1 = 5$ and $n_2 = 4.5$. It is worth noting that the stress components of the second-order solution are not uniform.

8.03.7 REFERENCES

- J. Ahmad, 1991, Micromechanics analysis of cracks in unidirectional fiber composites. *J. Appl. Mech.*, **58**, 964–972.
- A. R. Akisanya and N. A. Fleck, 1992, Analysis of a wavy crack in sandwich specimens. *Int. J. Fract.*, **55**, 29–45.
- G. P. Anderson, K. L. DeVries and M. L. Williams, 1974, Mixed-mode stress field effect in adhesive fracture. *Int. J. Fract.*, **10**, 565–583.
- N. Aravas and S. M. Sharma, 1991, An elastoplastic analysis of the interface crack with contact zones. *J. Mech. Phys. Solids*, **39**, 311–344.
- C. Atkinson, 1977, On quasistatic problems of cracks in a non-homogeneous elastic layer. *Acta Mech.*, **26**, 103–113.
- C. Atkinson, R. E. Smelser and J. Sanchez, 1982, Combined mode fracture via the cracked Brazilian disk test. *Int. J. Fract.*, **18**, 279–291.
- J. Aveston, G. A. Cooper, and A. Kelly, 1971, Single and multiple fracture. In: "The properties of fiber composites," ed. National Physics Laboratory, IPC Science and Technology Press, Teddington, UK, pp. 15–26.
- G. Bao, S. Ho, B. Fan and Z. Suo, 1992, The role of material orthotropy in fracture specimen for composites. *Int. J. Solids Struct.*, **29**, 1105–1116.
- J. L. Beuth, 1992, Cracking of thin bonded films in residual tension. *Int. J. Solids Struct.*, **29**, 1657–1675.
- E. Bischoff, M. Rühle, O. Sbaizero and A. G. Evans, 1989, Microstructural studies of the interfacial zone of a SiC-fiber reinforced lithium aluminum silicate glass-ceramic. *J. Am. Ceram. Soc.*, **72**, 741–745.
- D. B. Bogy, 1971, On the plane elastostatic problem of a loaded crack terminating at a material interface. *J. Appl. Mech.*, **38**, 911–918.
- B. Budiansky, J. W. Hutchinson and A. G. Evans, 1986, Matrix fracture in fiber reinforced ceramics. *J. Mech. Phys. Solids*, **34**, 167–189.
- H. C. Cao and A. G. Evans, 1989, An experimental study of the fracture resistance of bimaterial interface. *Mech. Mater.*, **7**, 295–304.
- H. Chai, 1987, A note on crack trajectory in an elastic strip bounded by rigid substrates. *Int. J. Fract.*, **32**, 211–213.
- C. R. Champion and C. Atkinson, 1991, A crack at the interface between two power law materials under plane strain loading. *Proc. Roy. Soc. London A*, **432**, 547–553.
- P. G. Charalambides, J. Lund, A. G. Evans and R. M. McMeeking, 1989, A test specimen for determining the fracture resistance of bimaterial interfaces. *J. Appl. Mech.*, **56**, 77–82.
- D. H. Chen, 1994, A crack normal to and terminating at a bimaterial interface. *Eng. Fract. Mech.*, **49**, 517–532.
- G. P. Cherepanov, 1962, The stress state in a heterogeneous plate with slits. *Izvestia AN SSSR, OTN, Mekhan. i Mashin.*, **1**, 131–137 (in Russian).
- G. P. Cherepanov, 1979, "Mechanics of Brittle Fracture," McGraw-Hill, New York.
- D. L. Clements and I. N. Sneddon, 1971, A crack between dissimilar anisotropic media. *Int. J. Eng. Sci.*, **9**, 257–265.
- M. Comninou, 1977, The interface crack. *J. Appl. Mech.*, **44**, 631–636.
- M. Comninou and D. Schmueser, 1979, The interface crack in a combined tension-compression and shear field. *J. Appl. Mech.*, **46**, 345–348.
- T. S. Cook and F. Erdogan, 1972, Stresses in bonded material with a crack perpendicular to the interface. *Int. J. Eng. Sci.*, **10**, 677–697.
- W. A. Curtin, 1993, Multiple matrix cracking in brittle matrix composites. *Acta Metall. Mater.*, **41**, 1369–1377.
- S. Danchavijit and D. K. Shetty, 1993, Matrix cracking in ceramic-matrix composites. *J. Am. Ceram. Soc.*, **76**, 2497–2504.
- F. Delale and F. Erdogan, 1988, On the mechanical modeling of the interfacial region in bonded half-planes. *J. Appl. Mech.*, **55**, 317–324.
- J. Dundurs, 1969, Edge-bonded dissimilar orthogonal elastic wedges. *J. Appl. Mech.*, **36**, 650–652.
- G. Ellsner, D. Korn and M. Rühle, 1994, Influence of interface impurities on fracture energy of UHV diffusion bonded metal-ceramic bicrystals. *Scr. Metal. Mater.*, **31**, 1037–1042.
- A. H. England, 1965, A crack between dissimilar media. *J. Appl. Mech.*, **32**, 400–402.
- A. G. Erdogan and V. Biricikoglu, 1973, Two bonded half planes with a crack going through the interface. *Int. J. Eng. Sci.*, **11**, 745–766.
- F. Erdogan, 1965, Stress distribution in bonded dissimilar materials with cracks. *J. Appl. Mech.*, **32**, 403–410.
- A. G. Evans and B. J. Dalgleish, 1992, The fracture resistance of metal-ceramic interfaces. *Acta Metall. Mater.*, **40**, S295–S306.
- A. G. Evans, B. J. Dalgleish, M. Y. He and J. W. Hutchinson, 1989, On crack path selection and the interface fracture energy in bimaterial system. *Acta Metall.*, **37**, 3249–3254.
- A. G. Evans and J. W. Hutchinson, 1995, The thermo-mechanical integrity of thin films and multilayers. *Acta Metall. Mater.*, **43**, 2507–2530.
- A. G. Evans, J. W. Hutchinson and Y. G. Wei, 1999, Interface adhesion: effects of plasticity and segregation. *Acta Mater.*, **47**, 4093–4113.

- A. G. Evans and D. B. Marshall, 1989, The mechanical behavior of ceramic-matrix composites. *Acta Metall.*, **37**, 2567–2583.
- A. G. Evans, M. Ruhle, B. J. Dalgleish and P. G. Charalambides, 1990, The fracture energy of bimaterial interfaces. *Mater. Sci. Eng. A*, **126**, 53–64.
- R. J. Farris and C. L. Bauer, 1988, A self-determination method of measuring the surface energy of adhesion of coatings. *J. Adhesion*, **26**, 293–300.
- N. A. Fleck, J. W. Hutchinson and Z. Suo, 1991, Crack path selection in a brittle adhesive layer. *Int. J. Solids Struct.*, **27**, 1683–1703.
- H. Gao, C. S. Yang, T. C. Wang and A. H. Zhou, 1979, Brittle fracture on combined mode I and mode II cracks. *Acta Metall. Sinica*, **15**, 380–391 (in Chinese).
- Y. C. Gao, Y. W. Mai and B. Cotterell, 1988, Fracture of fiber-reinforced materials. *J. Appl. Math. Phys.*, **39**, 550–572.
- F. Gaudette, S. Suresh, A. G. Evans, G. Dehm and M. Ruhle, 1997, The influence of chromium addition on the toughness of γ -Ni/ α -Al₂O₃ interface. *Acta Mater.*, **45**, 3503–3513.
- M. R. Gecit, 1979, Fracture of a surface layer bonded to a half space. *Int. J. Eng. Sci.*, **17**, 287–295.
- M. Gotoh, 1967, Some problems of bonded anisotropic plates with cracks along the bonds. *Int. J. Fract. Mech.*, **3**, 253–260.
- V. Gupta, A. S. Argon, D. M. Parks and J. A. Cornie, 1992, Measurement of interface strength by a laser spallation technique. *J. Mech. Phys. Solids*, **40**, 141–180.
- K. Hayashi and S. Nemat-Nasser, 1981, Energy-release rate and crack kinking under combined loading. *J. Appl. Mech.*, **48**, 520–524.
- M. Y. He, A. Bartlert, A. G. Evans and J. W. Hutchinson, 1991, Kinking of a crack out of an interface: role of in-plane stress. *J. Am. Ceram. Soc.*, **74**, 767–771.
- M. Y. He, H. C. Cao and A. G. Evans, 1990, Mixed mode fracture: the four-point shear specimen. *Acta Metall. Mater.*, **38**, 839–846.
- M. Y. He and A. G. Evans, 1991, Strength and fracture of metal/ceramic bonds. *Acta Metall. Mater.*, **39**, 1587–1593.
- M. Y. He and J. W. Hutchinson, 1989, “Kinking of Crack out of an Interface: Tabulated Solution Coefficients,” Division of Applied Sciences, Harvard University, Cambridge, MA.
- S. Ho and Z. Suo, 1992, Microcracks tunneling in brittle matrix composites driven by thermal expansion mismatch. *Acta Metall. Mater.*, **40**, 1685–1690.
- J. W. Hutchinson and A. G. Evans, 2000, Mechanics of materials: top-down approaches to fracture. *Acta Mater.*, **48**, 125–135.
- J. W. Hutchinson and Z. Suo, 1992, Mixed-mode cracking in layered materials. In: “Advances in Applied Mechanics,” eds. J. W. Hutchinson and T. Y. Wu, Academic Press, New York, vol. 29, pp. 63–191.
- H. M. Jensen, J. W. Hutchinson and K. S. Kim, 1990, Decohesion of a cut prestressed film on a substrate. *Int. J. Solids Struct.*, **26**, 1099–1114.
- H. M. Jensen and M. D. Thouless, 1993, Effects of residual stresses in the blister test. *Int. J. Solids Struct.*, **30**, 779–795.
- B. L. Karihaloo, 1982, Crack kinking and curving. *Mech. Mater.*, **1**, 189–201.
- S. G. Lekhnitskii, 1981, “Theory of Elasticity of an Anisotropic Elastic Body,” MIR, Moscow.
- Y. C. Li and T. C. Wang, 1986, High order asymptotic field of tensile plane strain nonlinear crack problem. *Sci. Sinica A*, **29**, 941–955.
- K. M. Liechti and Y. S. Chai, 1991, Biaxial loading experiments for determining interfacial fracture toughness. *J. Appl. Mech.*, **58**, 680–687.
- K. M. Liechti and Y. S. Chai, 1992, Asymmetric shielding in interfacial fracture under in-plane shear. *J. Appl. Mech.*, **59**, 295–304.
- K. Y. Lin and J. W. Mar, 1976, Finite element analysis of stress intensity factor for crack at a bimaterial interface. *Int. J. Fract.*, **12**, 521–531.
- D. M. Lipkin, D. R. Clarke and A. G. Evans, 1998, Effect of interfacial carbon on adhesion and toughness of gold-sapphire interfaces. *Acta Mater.*, **46**, 4835–4850.
- L. N. McCartney, 1987, Mechanics of matrix cracking in brittle-matrix fiber-reinforced composites. *Proc. Roy. Soc. London A*, **409**, 329–350.
- B. S. Majumdar, G. M. Newaz and A. R. Rosenfield, 1989, Yielding behavior of ceramic matrix composites. In: “Advances in Fracture Research, Proceeding of 7th International Conference on Fracture (ICF7),” eds. K. Salama, K. R. Chandar, D. M. R. Taplin and P. R. Rao, Pergamon, Oxford, UK, pp. 2805–2814.
- B. M. Malyshev and R. L. Salganik, 1965, The strength of adhesive joints using the theory of cracks. *Int. J. Fract. Mech.*, **1**, 114–128.
- D. B. Marshall and B. N. Cox, 1987, Tensile fracture of brittle matrix composites: influence of fiber strength. *Acta Metall.*, **35**, 2607–2619.
- D. B. Marshall, B. N. Cox and A. G. Evans, 1985, The mechanics of matrix cracking in brittle-matrix fiber composites. *Acta Metall.*, **33**, 2013–2021.
- J. M. McNaney, R. M. Cannon and R. O. Ritchie, 1996, Fracture and fatigue crack growth along aluminum-alumina interfaces. *Acta Mater.*, **44**, 4713–4728.
- G. Meda and P. S. Steif, 1994, Detailed analysis of cracks bridged by fibers: I. Limiting cases of short and long cracks. *J. Mech. Phys. Solids*, **42**, 1293–1321.
- S. A. Meguid, M. Tan and Z. H. Zhu, 1995, Analysis of crack perpendicular to bimaterial interface using a novel finite element. *Int. J. Fract.*, **73**, 1–23.
- G. R. Miller and W. L. Stock, 1989, Analysis of branched interface cracks between dissimilar anisotropic media. *J. Appl. Mech.*, **56**, 844–849.
- A. Needleman, 1987, A continuum model for void nucleation by inclusion debonding. *J. Appl. Mech.*, **54**, 525–531.
- N. P. O’Dowd, M. G. Stout and C. F. Shih, 1992, Fracture toughness of alumina-niobium interface experiments and analyses. *Phil. Mag. A*, **66**, 1037–1064.
- J. M. Qu and J. L. Bassani, 1989, Crack on bimaterial and bicrystal interfaces. *J. Mech. Phys. Solids*, **37**, 417–433.
- I. E. Reimanis, K. P. Trumble, K. A. Rogers and B. J. Dalgleish, 1997, Influence of Cu₂O and CuAlO₂ interphases on crack propagation at Cu/ α -Al₂O₃ interfaces. *J. Am. Ceram. Soc.*, **80**, 424–432.
- J. R. Rice, 1988, Elastic fracture mechanics concepts for interfacial cracks. *J. Appl. Mech.*, **55**, 98–103.
- J. R. Rice and G. C. Sih, 1965, Plane problems of cracks in dissimilar media. *J. Appl. Mech.*, **32**, 418–423.
- J. R. Rice, Z. Suo and J. S. Wang, 1990, Mechanics and thermodynamics of brittle interfacial failure in bimaterial systems. In: “Metal-Ceramics Interfaces,” eds. M. Ruhle, *et al.*, Pergamon, New York, pp. 269–294.
- L. R. F. Rose, 1987, Crack reinforcement by distributed springs. *J. Mech. Phys. Solids*, **35**, 383–405.
- M. Ruhle, A. G. Evans, M. F. Ashby and J. P. Hirth (eds.), 1990, “Metal-Ceramics Interfaces—Acta Scripta Metallogica Proc. Series 4,” Pergamon, New York.
- S. M. Sharma and N. Aravas, 1993, On the development of variable-separable asymptotic elastoplastic solutions for interfacial cracks. *Int. J. Solids Struct.*, **30**, 695–723.
- C. F. Shih, 1991, Cracks on bimaterial interfaces: elasticity and plasticity aspects. *Mater. Sci. Eng. A*, **143**, 77–90.
- C. F. Shih and R. J. Asaro, 1988, Elastic-plastic analysis of cracks on bimaterial interfaces: Part I. Small-scale yielding. *J. Appl. Mech.*, **55**, 299–316.

- C. F. Shih and R. J. Asaro, 1989, Elastic-plastic analysis of cracks on bimaterial interfaces: Part II. Structure of small-scale yielding fields. *J. Appl. Mech.*, **56**, 763-779.
- C. F. Shih and R. J. Asaro, 1990, Elastic-plastic analysis and asymptotic fields of interface cracks. *Int. J. Fract.*, **42**, 101-116.
- G. C. Sih, P. C. Paris and G. R. Irwin, 1965, On cracks in rectilinearly anisotropic bodies. *Int. J. Fract. Mech.*, **1**, 189-203.
- G. C. Sih and J. R. Rice, 1964, The bending of plates of dissimilar materials with cracks. *J. Appl. Mech.*, **31**, 477-482.
- D. Singh and D. K. Shetty, 1989, Fracture toughness of polycrystalline ceramics in combined mode I and mode II loading. *J. Am. Ceram. Soc.*, **72**, 78-84.
- P. Stähle, J. Gunnars and P. Delfin, 1995, Crack paths in a weak elastic layer covering a beam. *Acta Mech. Solida Sinica*, **8**, 579-583.
- H. Stang and S. P. Shah, 1986, Failure of fiber-reinforced composites by pull-out fracture. *J. Mater. Sci.*, **21**, 953-957.
- A. N. Stroh, 1958, Dislocations and cracks in anisotropic elasticity. *Phil. Mag.*, 625-646.
- Z. Suo, 1989, Singularities interacting with interfaces and cracks. *Int. J. Solids Struct.*, **25**, 1133-1142.
- Z. Suo, 1990a, Singularities, interfaces, and cracks in dissimilar anisotropic media. *Proc. Roy. Soc. London A*, **427**, 331-358.
- Z. Suo, 1990b, Delamination specimens for orthotropic materials. *J. Appl. Mech.*, **57**, 627-634.
- Z. Suo and J. W. Hutchinson, 1989a, On sandwich test specimen for measuring interface crack toughness. *Mater. Sci. Eng. A*, **107**, 135-143.
- Z. Suo and J. W. Hutchinson, 1989b, Steady-state cracking in brittle substrates beneath adherent films. *Int. J. Solids Struct.*, **25**, 1337-1353.
- Z. Suo and J. W. Hutchinson, 1990, Interface crack between two elastic layers. *Int. J. Fract.*, **43**, 1-18.
- Z. Suo, C. F. Shih and A. G. Varias, 1993, A theory for cleavage cracking in the presence of plastic flow. *Acta Metall. Mater.*, **41**, 1551-1557.
- S. Suresh, C. F. Shih, A. Morrone and N. P. O'Dowd, 1990, Mixed-mode fracture toughness of ceramic materials. *J. Am. Ceram. Soc.*, **73**, 1257-1267.
- M. D. Thouless, H. C. Cao and P. A. Mataga, 1989a, Delamination from surface cracks in composite materials. *J. Mater. Sci.*, **24**, 1406-1412.
- M. D. Thouless, O. Sbaizero, L. S. Sigl and A. G. Evans, 1989b, Effect of interface mechanical properties on pullout in a SiC-fiber reinforced lithium aluminum silicate glass-ceramic. *J. Am. Ceram. Soc.*, **72**, 525-532.
- T. C. T. Ting, 1986, Explicit solution and invariance of singularities at an interface crack in anisotropic composites. *Int. J. Solids Struct.*, **22**, 965-983.
- T. C. T. Ting, 1996, "Anisotropic Elasticity: Theory and Applications," Oxford University Press, New York.
- G. C. Trantina, 1972, Combined mode crack extension in adhesive joints. *J. Composite Mater.*, **6**, 371-385.
- M. R. Turner, B. J. Dalgleish, M. Y. He and A. G. Evans, 1995, A fracture resistance measurement method for bimaterial interfaces having large debond energy. *Acta Metall. Mater.*, **43**, 3459-3465.
- V. Tvergaard and J. W. Hutchinson, 1992, The relation between crack growth resistance and fracture process parameters in elastic-plastic solids. *J. Mech. Phys. Solids*, **40**, 1377-1397.
- V. Tvergaard and J. W. Hutchinson, 1993, The influence of plasticity on mixed mode interface toughness. *J. Mech. Phys. Solids*, **41**, 1119-1135.
- J. Wang and B. L. Karihaloo, 1994, Mode II and mode III stress singularities and intensities at a crack terminating on a transversely isotropic-orthotropic interface. *Proc. Roy. Soc. London A*, **444**, 447-460.
- J. Wang and B. L. Karihaloo, 1996, Mode I stress singularity and intensity at a crack tip terminating on a transversely isotropic-orthotropic bimaterial interface. *Int. J. Fract.*, **74**, 325-340.
- J. S. Wang and Z. Suo, 1990, Experimental determination of interfacial toughness curves using Brazil-nut-sandwiches. *Acta Metall.*, **38**, 1279-1290.
- K. R. Wang and T. C. Wang, 1987, Conservation integrals and governing equation for singularity field. *Appl. Math. Mech.*, **8**, 791-797 (in Chinese).
- K. R. Wang, J. L. Xu and H. Gao, 1977, Calculation of stress intensity factors for combined mode bend specimens. In: "Fracture (ICF7)," ed. D. M. R. Taplin, vol. 4, pp. 123-133.
- S. S. Wang and I. Choi, 1983, The interface crack between dissimilar anisotropic composite materials. *J. Appl. Mech.*, **50**, 169-178.
- S. S. Wang, J. F. Mandell and F. J. McGarry, 1978, An analysis of the crack tip stress field in DCB adhesive fracture specimens. *Int. J. Fract.*, **14**, 39-58.
- T. C. Wang, 1986, Singularity fields of stress and strain near crack tip for combined mode crack. In: "Proceedings International Conference Comp. Mech.," Tokyo, vol. 1, V227-V234.
- T. C. Wang, 1990, Elastic-plastic asymptotic fields for cracks on bimaterial interfaces. *Eng. Fract. Mech.*, **37**, 527-538.
- T. C. Wang, 1994, Kinking of an interface crack between two dissimilar anisotropic elastic solids. *Int. J. Solids Struct.*, **31**, 629-641.
- T. C. Wang, C. F. Shih and Z. Suo, 1992, Crack extension and kinking in laminates and bicrystals. *Int. J. Solids Struct.*, **29**, 327-344.
- T. C. Wang and P. Stähle, 1998a, Stress state in front of a crack perpendicular to bimaterial interface. *Eng. Fract. Mech.*, **59**, 471-485.
- T. C. Wang and P. Stähle, 1998b, A crack perpendicular to and terminating at a bimaterial interface. *Acta Mech. Sinica*, **14**, 27-36.
- W. C. Wang and J. T. Chen, 1993, Theoretical and experimental re-examination of a crack perpendicular to and terminating at the bimaterial interface. *J. Strain Anal.*, **28**, 53-61.
- Y. G. Wei and J. W. Hutchinson, 1997a, Nonlinear delamination mechanics for thin films. *J. Mech. Phys. Solids*, **45**, 1137-1159.
- Y. G. Wei and J. W. Hutchinson, 1997b, Steady state crack growth and work of fracture for solids characterized by strain-gradient plasticity. *J. Mech. Phys. Solids*, **45**, 1253-1273.
- Y. G. Wei and J. W. Hutchinson, 1999, Models of interface separation accompanied by plastic dissipation at multiple scales. *Int. J. Fract.*, **95**, 1-17.
- J. K. Wells and P. W. R. Beaumont, 1985, Debonding and pull-out processes in fibrous composites. *J. Mater. Sci.*, **20**, 1275-1284.
- M. L. Williams, 1959, The stress around a fault of crack in dissimilar media. *Bull. Seismol. Soc. Am.*, **49**, 199-204.
- J. R. Willis, 1971, Fracture mechanics of interface crack. *J. Mech. Phys. Solids*, **19**, 353-368.
- K. C. Wu, 1990, Stress intensity factor and energy release rate for interfacial cracks between dissimilar anisotropic materials. *J. Appl. Mech.*, **57**, 882-886.
- L. Xia and T. C. Wang, 1992, Asymptotic fields for interface crack in elastic-plastic material. *Acta Mech. Solida Sinica*, **5**, 245-258.
- L. Xia and T. C. Wang, 1994a, Elastic-plastic stress field of frictionless contact at interfacial crack tip. *Acta Mech. Solida Sinica*, **15**, 19-30 (in Chinese).
- L. Xia and T. C. Wang, 1994b, High-order analysis of near tip fields around an interfacial crack between two

- dissimilar power law hardening materials. *Acta Mech. Sinica*, **10**, 27–39.
- Z. C. Xia, J. W. Hutchinson, A. G. Evans and B. Budiansky, 1994, On large scale sliding in fiber-reinforced composites. *J. Mech. Phys. Solids*, **42**, 1139–1158.
- T. Ye, Z. Suo and A. G. Evans, 1992, Thin film cracking and the roles of substrate and interface. *Int. J. Solids Struct.*, **29**, 2639–2648.
- A. R. Zak and M. L. Williams, 1963, Crack point singularities at a bi-material interface. *J. Appl. Mech.*, **30**, 142–143.
- E. Zywicki, 1988, On elastic–plastic cracks between dissimilar media. Ph.D. thesis, Massachusetts Institute of Technology, Cambridge, MA.
- E. Zywicki and D. M. Parks, 1990, Elastic–plastic analysis of frictionless contact at interfacial crack tips. *Int. J. Fract.*, **42**, 129–143.